https://ntrs.nasa.gov/search.jsp?R=19970037592 2020-06-16T01:47:05+00:00Z

NASA Technical Paper 3702

Micro-Mechanical Voltage Tunable Fabry-Perot Filters Formed in (111) Silicon

James D. Patterson
Langley Research Center, Hampton, Virginia

National Aeronautics and
Space Administration

Langley Research Center
Hampton, Virginia 23681-2199

September 1997

The information in this report was offered as a thesis in partial fulfillment of the requirements for the Degree of Doctor of Philosophy in Electrical Engineering, University of Colorado, Boulder, Colorado.

Available from the following:

NASA Center for AeroSpace Information (CASI)
800 Elkridge Landing Road
Linthicum Heights, MD 21090-2934
(301) 621-0390

National Technical Information Service (NTIS)
5285 Port Royal Road
Springfield, VA 22161-2171
(703) 487-4650

Abstract

The MEMS (Micro-Electro-Mechanical-Systems) technology is quickly evolving as a viable means to combine micro-mechanical and micro-optical elements on the same chip. The methods for MEMS fabrication are based on those already used in the well established semiconductor industry. Dry and wet etching of deposited, grown, or bulk layers is used to form movable structures of micron dimensions. These structures can be fabricated on the traditional semiconductor substrate materials making possible the further integration of MEMS devices with optoelectronics and electronics. Such integration could, significantly improve the performance, increase the functionality, reduce the size, and cost of optical systems.

One MEMS technology that has recently gained attention by the research community is the micro-mechanical Fabry-Perot optical filter. A MEMS based Fabry-Perot consist of a vertically integrated structure composed of two mirrors separated by an air gap. Wavelength tuning is achieved by applying a bias between the two mirrors resulting in an attractive electrostatic force which pulls the mirrors closer. MEMS based Fabry-Perots can provide large tuning ranges, on the order of hundreds of nanometers with a 5V bias. This is an advantage over electro-optic effect Fabry-Perots which are limited to under 10nm of tuning range due to the small refractive index changes possible.

The methods for micro-mechanical Fabry-Perot filter fabrication recently reported in the literature require many (10 to 44 layers) deposited or grown layers to form the DBR (Distributed Bragg Reflector) mirrors and to provide the sacrificial layer for the air gap. Consequently, the fabrication of these Fabry-Perots is complex and costly. In this work, we present a new micro-mechanical Fabry-Perot structure which is simpler to fabricate and is integratable with low cost silicon based photodetectors and transistors. The structure consists of a movable gold coated oxide cantilever for the top mirror and a stationary Au/Ni plated silicon bottom mirror. The fabrication process is single mask level, self aligned, and requires only one grown or deposited layer. Undercutting of the oxide cantilever is carried out by a combination of RIE and anisotropic KOH etching of the (111) silicon substrate. Metallization of the mirrors is provided by thermal evaporation and electroplating.

The optical filtering characteristics of the fabricated devices were studied. A wavelength shift of 120nm with 53V applied bias was demonstrated by one device geometry using a 6.27μm air gap. The finesse of the structure was 2.4. Modulation bandwidths ranging from 91KHz to greater than 920KHz were also observed. Theoretical calculations show that if mirror reflectivity, smoothness, and parallelism are improved, a finesse of 30 is attainable. The predictions also suggest that a reduction of the air gap to 1μm results in an increased wavelength tuning range of 175nm with a CMOS compatible 4.75V.

Acknowledgments

I am indebted to many individuals who have assisted me during the study of the micro-mechanical filters. I would like to thank and acknowledge them for their efforts.

My advisor, Professor Bart Van Zeghbroeck has provided countless hours of discussion and advice that have propelled the research along the way. I am indebted to him for this and also for his strong optimism that kept me going during times of frustration.

I would like to thank the Ph.D. committee members for their input into the research, especially their guidance on the critical issues, that formed the framework of the research.

I am extremely grateful to Professor Bill May for many hours of discussion on the processing issues and his many hours of assistance in the integrated circuit lab. I also thank Skip Wichart for his advice and the many times in which he repaired the reactive ion etcher.

Special thanks is owed to the Optoelectronics Division at the National Institute of Standards and Technology (NIST) at Boulder for the use of their Ti:Sapphire laser system in the spectral analysis of the Fabry-Perot filters. Specific thanks is owed to Kevin Knopp for setting up and trouble shooting the spectral analysis system and to Dave Christensen who offered NIST's services for this study.

Contents

Abstract iii

Acknowledgements iv

List of Tables vii

List of Figures viii

I. Introduction 1

1.1 MEMS: an Overview 1
1.2 MEMS based Fabry-Perots: the State of the Art 1
1.3 Potential Applications of the Cantilever Fabry-Perot 2
1.4 A Novel Silicon Based Micro-Mechanical Fabry-Perot 3
1.5 References 5

II. Electro-Mechanical and Optical Theory 7

2.1 Introduction 7
2.2 Electro-Mechanical Theory 7
2.2.1 Derivation of the Cantilever Bending Equation 7
2.2.2 Derivation of the Cantilever's Frequency Response 10
2.2.3 Numerical Results For the Cantilever Bending and Frequency Response 15
2.3 Optical Theory 20
2.3.1 Introduction 20
2.3.2 The Calculation of the Transmission and Reflectance Spectra Using the Matrix Method 21
2.4 Numerical Predictions For the Optical Filter: Electro-Mechanical and Optical Theory Combined 24
2.5 References 31

III. Fabrication of Micro-Mechanical Fabry Perot Filters 33

3.0 Introduction 33
3.1 Popular Methods of Micro-Mechanical Fabry-Perot Fabrication Using Deposited Materials 33
3.2 Anisotropic Etching of Silicon in Potassium Hydroxide 33
3.3 Fabrication of the Fabry-Perots in (111) Silicon: an Overview 36
3.4 Fabrication of Fabry Perots Filters in (111) Silicon: Details and Results 38
3.4.0 Process Objectives 38
3.4.1 Si Wafer Specifications 38
3.4.2 Thermal Oxidation 39
3.4.3 Masking Materials For Reactive Ion Etching 39
3.4.4 The Photolithographic Mask Design 39
3.4.4.1 Mask Design Introduction 39
3.4.4.2 Why Cantilever Mirrors? 40
3.4.4.3 Mask Design For Electrical Isolation 41

3.4.5 Reactive Ion Etching of the Si Well and Isolation Trench 41
3.4.6 KOH Undercutting of the Silicon Dioxide 43
3.4.6 .1 Lower Than Expected KOH Selectivities 44
3.4.7 Chip Rinsing and Nitric Acid Treatment 50
3.4.8 Metal Electroplating of the Lower Mirror 50
3.4.9 Drying of the Cantilever Structures Following Wet Processing 53
3.4.9.1 Drying Through Room Air Evaporation and the Pinning/Sticking Problem 53
3.4.9.2 Critical Point Drying 56
3.4.10 Top Mirror Metal Evaporation 57
3.4.11 Stress Induced Cantilever Mirror Curvature 59
3.5 References 60

IV. Electro-Mechanical and Electro-Optical Characterization 63

4.1 Introduction 63
4.2 SEM Characterization of the Electro-Mechanical Behavior 63
4.3 Electro-Optical Characterization: Wavelength Resolved 67
4.3.0 Introduction 67
4.3.1 Spectral Analysis of a Modulator Without Ni: Early Spectral Results 68
4.3.2 Spectral Analysis of a Modulator Including the Ni Layer 70
4.4 Electro-Optical Characterization: Time Resolved 80
4.5 References 85

V. Conclusion 87

5.1 Summary of the Study: Major Issues 87
5.2 Micro-Mechanical Fabry-Perot Performance Comparison 88
5.3 References 89
Comprehensive List of References 91

List of Tables

Table

2-1. Material Constants Used in the Bending Theory and Frequency Response Calculations ... 15

2-2. Optical constants Used in the Theoretical Analysis ... 24

3-1. RIE Etch Rates of Silicon, Silicon Dioxide, and Negative Photoresist in CF_4 ... 43

3-2. Measured KOH Etch Rates and Selectivities of Silicon and Silicon Dioxide ... 46

3-3. KOH Etch Rates and Selectivities Reported by Waggener ... 47

5-1. Micro-Mechanical Fabry-Perot Performance Comparison ... 89

List of Figures

Figure

1-1 An array of micro-mechanical Fabry-Perot filters is used as a WDM demultiplexer with wavelength tracking capability 3

1-2. Cross-sectional diagram of the novel Si (111) based micro-mechanical Fabry-Perot filter 4

2-1. Cantilever schematic for the electro-mechanical analysis 7

2-2. Diagram used for the calculation of the moment of inertia for the cantilever beam 9

2-3. Cantilever profiles for 2.5 and 5.0 volt bias. The cantilever length is 100 μm and has a 0 voltage air gap of 1 μm. The oxide thicknesses is 0.85 μm 15

2-4. Cantilever profiles for 15 and 30 volts. The cantilever length is 100 μm and has a 0 voltage air gap of 4 μm 16

2-5. The position of the cantilever tip as the bias is swept in the forward and reverse directions for a h_{co} = 1 μm air gap cantilever. 17

2-6. The position of the cantilever tip as the bias is swept in the forward and reverse directions for a 4 μm air gap cantilever 18

2-7. Forward and reverse sweep of the bias voltage under the $V<V_{th}$ constraint for cantilevers with h_{co} equal to 1, 2, and 4μm. 18

2-8. Theoretical Bode plot showing the cantilever tip displacement response. The theory models the cantilever as a linear-spring point-mass system that is described by Eq. 2-13. The oxide cantilever was 101 μm long by 20 μm wide with a thickness of 0.85 μm. 19

2-9. Bandwidth and cantilever tip deflection as a function of cantilever length 20

2-10. Diagram of the multilayered stack used in the spectral analysis 21

2-11A. Transmission spectra for a 1 μm air gap Fabry-Perot at zero bias. The gold thickness is 20 nm. The finesse of the Fabry-Perot is 8.0. 25

2-11B. Reflection spectra for a 1 μm air gap Fabry-Perot at zero bias. The gold thickness is 20 nm. The finesse of the Fabry-Perot is 8.0. 25

2-12. Transmission spectra for a 1 μm air gap Fabry-Perot at zero bias. The gold t hickness has been increased from 20 nm to 50 nm providing a finesse increase from 8 to 30 27

2-13. Transmittance and finesse as a function of gold thickness. Power throughput and finesse are traded off 27

2-14. The spectral transmittance of the Fabry-Perot as a function of tuning voltage. The 0 volt bias air gap is 1 μm and the gold mirror thickness is 40 nm 28

2-15. Transmission peak wavelength versus tuning voltage for the 1 μm air gap cantilever 28

2-16. Transmission spectrum for a 4 μm air gap Fabry-Perot at zero bias 30

2-17. The spectral transmittance of the Fabry-Perot as a function of tuning voltage. The 0 Volt bias air gap is 4 μm and the gold mirror thickness is 40 nm. 30

2-18. Transmission peak wavelength versus tuning voltage for the 4 μm air gap cantilever. 31

3-1. Pyramidal structure formed in (100) Si by KOH etching. 34

3-2. Rectangular trenches formed in (110) Si by KOH etching 35

3-3. Schematic of (111) Si following vertical drilling using RIE. 35

3-4. Cross-sectional diagram of (111) silicon drilled vertically with RIE and followed with lateral KOH etching 36

3-5. Basic movable mirror fabrication process. 37

3-6. Staircase Si profile which results from 4° misalignment with the (111) direction. 38

3-7. Cross-section of the wafer following oxide growth and masking for reactive ion etching. 39

3-8. The single mask required for the fabrication of the micro-mechanical Fabry-Perot filters. The mask incorporates a wide variety of cantilever shapes each surrounded by a hexagonal electrical isolation trench. 40

3-9. A SEM photograph of an "H" shaped oxide membrane on Si which is sagging due to compressive stress 40

3-10. The shape of the cantilever silicon well and the hexagonal isolation trench provide electrical isolation between the cantilevers and the underlying Si and between individual cantilevers on the die 42

3-11. A cross-sectional diagram of the wafer showing chromium or photoresist covered regions that are protected during the RIE vertical etching 42

3-12. A cross section of the wafer following RIE of the SiO_2 and Si layers. This step exposes (110) facets for subsequent lateral undercutting of the oxide layer during the KOH etch step 43

3-13. Lateral undercutting of the cantilever by rapid wet KOH etching in the (110) direction. 44

3-14. The lateral undercutting has completely removed the Si underneath the cantilever. 44

3-15A-D. Optical micrographs showing the evolution of the KOH undercutting as a function of etch time. The cantilever is 20 μm wide and is parallel to the (110) flat. 45

3-16. A SEM photo of the entire Fabry-Perot structure including the hexagonal isolation trench following 45 minutes of KOH etching. The KOH etching of the hexagonal isolation trench has provided uniformly undercut oxide eaves around the inside perimeter of the trench. 45

3-17. A graphical comparison between our measured (110)/(111) selectivities and to those reported by Waggener . The KOH percentage of the etchant is 45% 48

3-18. A graphical comparison between our measured (110)//SiO_2 selectivities and those reported by Waggener. The KOH percentage of the etchant is 45% 48

3-19. The misalignment of the wafer surface normal with the (111) direction results in a much higher apparent (111) etch rate due to the (110) etch rate projection 49

3-20. A Dektak profile underneath a 20 μm wide cantilever. The profile is measured across the narrow width of the cantilever near the tip. The measured angle between the reference and measurement cursors is 0.13°. 50

3-21A. A SEM photo of a cantilever Fabry-Perot structure showing KOH etch residue on the silicon (white specks).This device was rinsed with water followed by acetone..... 51

3-21B. A SEM photo of a cantilever Fabry-Perot structure showing the absence of the residue when cleaned with nitric acid. 51

3-22. A SEM photo of the cantilever Fabry-Perot structure showing the absence of the residue under the cantilever. This device was not cleaned with nitric acid..... 52

3-23. A cross-sectional diagram of the Fabry-Perot structure following Ni plating. The Ni has plated only the Si and not the SiO_2 preserving the electrical isolation between the top and bottom mirrors. 54

3-24. An optical micrograph of a Ni plated 3.2 μm cavity Fabry-Perot..... 54

3-25. An optical micrograph of a Ni plated 0.6 μm air gap Fabry-Perot. Note the rough Ni plating under the cantilever and oxide eaves. The roughness is a consequence of poor plating solution and gas transport in the narrow gap..... 54

3-26A-C. The pinning process of a cantilever that is dried through room air evaporation... 55

3-27. A SEM photo of an room air dried cantilever that is pinned down to the Si surface due to capillary and Van der Waals forces. 56

3-28. A SEM photo of an air dried Fabry-Perot including the surrounding hexagonal isolation trench. Note that the oxide eaves around the trench have been pulled down into contact with the Si. These contact points will result in the loss of electrical isolation between the top and bottom mirror metallization..... 56

3-29. A SEM photo of a CPD dried cantilever which is erect in contrast to the air dried structures..... 57

3-30. A SEM photo of a CPD dried cantilever Fabry-Perot which is erect. Note also that the oxide eaves used for the electrical isolation are not in contact with silicon layer below in contrast to the air dried devices..... 58

3-31. A cross-sectional diagram of a cantilever Fabry-Perot following the top mirror gold evaporation. Note the electrical discontinuity provided by the underside of the oxide eaves..... 58

3-32. A microphotograph of a completely processed micro-mechanical tunable optical filter based on a movable cantilever mirror. The top side of the cantilever is coated with gold. The silicon underneath the cantilever is plated with nickel..... 59

3-33. SEM photographs illustrating the stress induced upward cantilever curvature. Thicker oxide cantilevers curve less..... 60

4-1. A photo of the cantilever modulator studied under bias in the SEM..... 63

4-2. A cross-sectional schematic of the cantilever modulator studied in the SEM..... 64

4-3. A SEM photo of the cantilever modulator without an applied bias..... 64

4-4. A SEM voltage contrast photo showing electrical isolation between the top and bottom mirrors of the contacted Fabry-Perot. The top mirror of the contacted device is also shown to be electrically isolated from the top mirrors of adjacent structures. 65

4-5. A SEM photo of the cantilever with 0 volts applied bias. 66

4-6. A SEM photo of the cantilever with 45 volts applied bias. The cantilever has been moved into contact with the silicon surface. 66

4-7. The predicted Displacement-Voltage characteristic for the cantilever structure studied in the SEM. 67

4-8. The experimental arrangement used to spectrally characterize the Fabry-Perot filters. 68

4-9. The cantilever structure which was spectrally analyzed with the Ti:Sapphire laser. The length of the cantilever is a stiff 30 μm. The bottom mirror is not coated with nickel and provides only the 35% reflectivity of the bare silicon. 69

4-10. Fabry-Perot spectra taken at 0, 30, and 40 volts. 69

4-11. A cross-sectional diagram of a cantilever modulator with a nickel plated bottom mirror. 70

4-12. The Fabry-Perot spectra taken at 40, 44, and 48 volts applied bias. 71

4-13. A comparison between measured and theoretically predicted spectra for the Fabry-Perot at 40 volts applied bias. The calculated spectrum assumes ideal, flat and parallel, top and bottom mirrors. 72

4-14. Mirror profiles of the Fabry-Perot. The 101 μm long cantilever is curving upwards due to stress damage. The bottom mirror is angled at -0.5° to represent the worst case staircase effect. The bias between the two mirrors is 40 volts. 73

4-15. The measured intensity profile of the focused light beam on the top mirror. The profile is fitted with a $\sigma = 5$ μm gaussian function. The gaussian function is used to weight the spectra in the summation. 74

4-16. Reflectance as a function of wavelength for various spot sizes. Here the spectral summation approximation was used to calculate the total reflectance. The mirror profiles are those from Figure 4-14. 75

4-17. Experimental and theoretical spectra for the 101 μm long cantilever. The non I deal Fabry Perot theoretical spectrum was calculated using the summation approximation. 76

4-18. Experimental and theoretical spectra for the 101 μm long cantilever. The theoretical spectra were calculated using the weighted spectral summation. The dashed curves represent the theoretical spectra for the case of, both stress induced curvature of the top mirror and an angled bottom mirror, and only including curvature of the top mirror. The degradation due to the top mirror curvature is dominant. 77

4-19. The minimum reflectance wavelength for one cavity mode as a function of applied DC voltage. The theoretical predictions using 5.0×10^{10} N/m^2 for the oxide elasticity modulus closely match the experimentally measured values. 78

4-20. On/Off ratio versus voltage for the cantilever Fabry-Perot. 79

4-21. Repeatability of the cantilever Fabry-Perot spectra before and after cycling the cantilever from 0 to 54 volts and back ten times. Both spectra were measured at 40 V applied bias. Significant changes in the spectrum were not observed..... 79

4-22. Spectrum repeatability before and after 8 hours of oscillation at a 10 Khz drive frequency. The applied voltage consisted of a 41 V DC bias in series with a 5 V peak-to-peak sinusoidal signal. 80

4-23. An illustration of the biasing scheme used for the time resolved measurements. ... 81

4-24. Modulation of 830 nm laser light by a cantilever modulator driven at 10 KHz. The DC bias was 21 V..... 82

4-25. Modulation of 830 nm laser light by a cantilever modulator driven at its resonance frequency of 57 KHz. Note the higher order frequency components in the photodetector signal due to the large cantilever deflection..... 82

4-26. Frequency response of a cantilever modulator with length 101 μm..... 83

4-27. Frequency response of a cantilever modulator with of length 45 μm..... 83

4-28. Bandwidth and resonant frequency versus cantilever length. The calculated values are shown by the lines and the experimental values by the diamonds. The elasticity modulus used in the theoretical curves was 5.0 X 10^{10} N/m^2..... 84

4-29. Bandwidth and resonant frequency versus cantilever length. The calculated values are shown by the lines and the experimental values by the diamonds. The elasticity modulus used in the theoretical curves was 7.3 X 10^{10} N/m^2..... 85

I. Introduction

1.1 Micro-Electro-Mechanical-Systems (MEMS): an Overview

The MEMS technology is quickly evolving as a viable means to combine micro-mechanical, micro-optical, opto-electronic, and electronic devices on the same chip. The methods for MEMS fabrication are based on those already used in the well established semiconductor industry. Dry and wet etching of deposited, grown, or bulk layers is used to form moveable micron sized structures. These micro-mechanical structures can be formed on traditional semiconductor substrate materials including silicon and gallium arsenide. This makes possible the integration of micro-mechanical systems with transistors, optical transmitters, and photodetectors. The monolithic realization of these electro-optical systems will provide many advantages including higher performance, lower cost, and reduced size.

Historically, micro-mechanics had its beginnings during the early years of the integrated circuit industry. In 1965 H. C. Nathanson et al. of Westinghouse Research Laboratories invented the silicon based resonant gate transistor [1, 2]. The transistor used a cantilever based gate electrode to control the channel transconductance. The strong mechanical resonance of the cantilever provided a high-Q bandpass electrical filter. Nathanson's work generated a brief flurry of interest in micro-mechanics. However, the interest waned, due to the ease in which the filtering behavior could be implemented electronically. Slowly, micro-mechanics has evolved with emphasis on applications that could not be implemented with the same performance and simplicity using electronics. For many years following, the fabrication of ink jet nozzles and print heads represented the main thrust in micro-mechanics [3–5].

Today, the MEMS technology has widespread applications in many areas. These areas include micro-optics, mechanical actuation, and sensing. Tiny optical benches on a chip are now possible. Texas Instruments has developed and is currently marketing arrays of digital micro-mirror devices for use in overhead projectors and printers [6]. In the area of optical communications MEMS based Fabry-Perot optical filters are being used to tune to and track WDM (Wavelength Division Multiplexing) signals [7–14]. Acceleration, pressure, and temperature sensors based on micro-mechanics are being developed and are available off-the-shelf [15–17]. These and growing numbers of applications are being developed to take advantage of the integrateability of optics, electronics, and micro-mechanics on a single substrate.

1.2 MEMS Based Fabry-Perot Filters: The State of the Art

One MEMS device that has recently (in the past few years) gained increased attention is the tunable micro-mechanical Fabry-Perot filter. These micro-mechanical Fabry-Perot filters consist of two mirrors separated by an air gap. The structure is formed vertically. The mirrors either consist of multilayer DBR (Distributed Bragg Reflector) stacks or a highly reflective metallic layers such as gold. The air gap is formed by the etching of a sacrificial layer. The top mirror is freely suspended above the bottom mirror. A voltage applied between electrical contacts on the two mirrors results in an attractive electrostatic force which pulls the top mirror down. Consequently, the air gap and transmission wavelength of the Fabry-Perot are reduced.

Traditionally, semiconductor Fabry-Perots have provided tuning based on a cavity refractive index change through the Stark and the electro-optic effects. The tuning range of these devices have been limited to less than 10 nm due to the small index changes possible [8, 18, 19]. On the other hand, micro-mechanical Fabry-Perots with tunable air gaps provide much wider tuning ranges than their Stark or electro-optic effect counterparts. Micro-mechanical Fabry-Perots have demonstrated a tuning range as high as 70 nm with a maximum 5 volts applied bias.

Both GaAs and Si based micro-mechanical Fabry-Perots have been investigated and have shown promising performance characteristics. Researchers at Stanford University and the University of California at Berkley have been working with GaAs based micro-mechanical Fabry Perots. The thrust of their work has dealt with controlling the output wavelength of VCSEL s (Vertical Cavity Surface Emitting Lasers) with a tunable coupled cavity micro-mechanical Fabry-Perot [7, 9, 10, 20]. M.S. Wu et al. have fabricated and

have tested a GaAs based micro-mechanical Fabry-Perots with the largest tuning range [20]. The Fabry-Perot demonstrated 70 nm of wavelength tuning (wavelength range: 900 to 970 nm) with a maximum of 4.9 volts bias. The linewidth of the transmission spectra was less than 10 nm. Their design incorporates two molecular beam epitaxy grown AlAs/GaAs Distributed Bragg Reflector (DBR) mirrors separated by an air gap. The top and bottom DBR mirrors use 12.5 and 9 quarter wavelength pairs respectively. The top DBR mirror geometry is a cantilever and moves by a bending motion.

A group at the National Nano Fabrication facility at Cornell is currently fabricating silicon based micro-mechanical Fabry-Perots. A. T. T. D. Tran et al. have fabricated a silicon based Fabry-Perot which uses two three and a half period CVD (Chemical Vapor Deposition) deposited Si/SiO_2 DBR mirrors for the cavity [11–13]. Tran achieved 40 to 60 nm (wavelength range: 1490 to 1540 nm) of tuning with 65 volts maximum bias applied to the structure. A 5 nm linewidth was typical for this device. The top suspended mirror for this structure was held on four sides, and consequently moved by more difficult stretching instead of bending like the GaAs cantilevers.

As mentioned previously, the air gap micro-mechanical Fabry-Perot filters provide a larger tuning range than their Stark effect counterparts. However, there are disadvantages and problems associated with the micro-mechanical Fabry-Perots. Although they provide a large tuning range there is a tradeoff in bandwidth. Practical Fabry-Perots have demonstrated bandwidths of less than 1Mhz [1, 2, 21]. Yields of the devices have been less than desirable. The suspended mirrors are fragile and require careful handling following air gap formation. Due to their fragility, integration with electronics requires that the Fabry-Perot air gap formation be the last step. Stress due to differences in the thermal coefficients of expansion have caused the Fabry-Perot mirrors to curve resulting in a less than stable optical resonator [13]. Lifetimes of the movable mirrors are sometimes limited to fatigue [21]. If wet etching is used to remove the sacrificial layer, capillary and intersolid forces during the rinse/dry step could result in plastic deformation of the structure and the potential pinning of the two mirrors together [22].

1.3 Potential Applications of the Cantilever Micro-Mechanical Fabry-Perot

There are many applications in which the modulator can be used. Here we present a few potential possibilities although there may be many others.

The wide wavelength tuning range of by micro-mechanical Fabry-Perot filters along with their potential chip integrateability with photodetectors and electronics makes them attractive for use as miniature scanning spectrometers. The vertical integration of the filter with a photodetector requires a minimal amount of chip real estate thus allowing for large arrays of the spectrometers. One application poised to take advantage of the wavelength selective nature of the micro-mechanical Fabry-Perots is optical fiber communications. A growing trend in fiber optic communications is the use of multiple wavelength channels on the same fiber to provide increased data bandwidth [23]. This type of multiplexing is commonly called Wavelength Division Multiplexing (WDM). At the receiver end of these systems, the WDM optical channels are demultiplexed and detected with a photodetector. For dense (5 channels or more) WDM optical systems, the demultiplexing is usually carried out using a diffraction grating based system. A problem inherent with this type of system is that the grating system is designed to accommodate fixed wavelength channels. In reality, the wavelengths of the semiconductor lasers drift during operation due to thermal effects. Additionally, it is very difficult and expensive to specify the laser center wavelength with tight enough tolerances. A solution to the laser drift and specification problem is an adaptable receiver.

This solution can be realized with an array of Fabry-Perot filter photo-detector pairs as shown in Figure 1-1. The structure is basically a drop demultiplexer realized with an array of Fabry-Perot filters. Each filter in succession, is voltage tuned to drop and measure one WDM channel while reflecting the remaining channels. Sequentially, each channel is picked off and measured by the properly tuned Fabry-Perots. Thermal drift of the individual channel wavelengths is accommodated by feedback control methods between the photodetector and the movable mirror. This technique has been demonstrated successfully by M. S. Wu et al. [24].

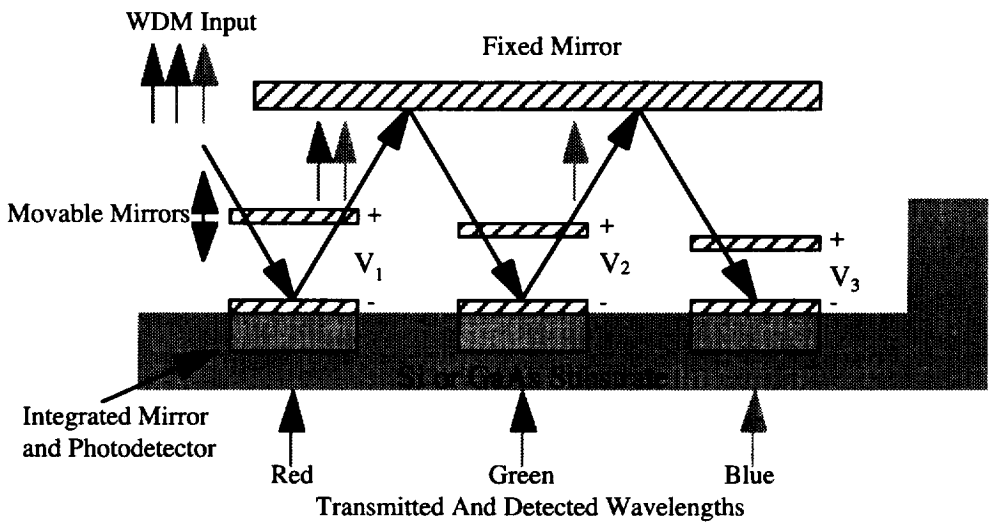

Figure 1-1. An array of micro-mechanical Fabry-Perot filters is used as a WDM demultiplexer with wavelength tracking capability.

Another possible application for the tunable filters is a flat panel display using the Fabry-Perot as a color producing pixel element. Black and white displays have been demonstrated using thick metal-coated movable cantilever mirrors by IBM researchers in 1977 [25]. The imaging system used a quasi-collimated light source to illuminate arrays of the cantilever mirrors. The display image was formed by directing the light from each cantilever mirror in or out of the numerical aperture of the imaging lens. This imaging system was probably the precursor to Texas Instruments' Digital Micro-Mirror Device (DMD) display[6].

Optically interrogatable acceleration and temperature sensing are also possibilities for the micro-mechanical Fabry-Perot filter. Cantilever bending due to acceleration forces can be translated into the spectral transmission shift of a broadband source or the power modulation of monochromatic laser light. Temperature sensing is possible by the fabrication of the movable mirror with two materials with large differences in thermal coefficient of expansion. This large difference can be used to produce the bimetallic bending effect. The thermal stress induced bending of the movable mirror results in an optical cavity length change. The temperature dependent cavity length is used to relate temperature to the spectral transmission properties of the Fabry-Perot.

1.4 A Novel Silicon Based Micro-Mechanical Fabry-Perot

The fabrication of the micro-mechanical Fabry-Perots as reported in the literature rely on multilayered deposited films for the mirrors and selective isotropic removal of a deposited sacrificial layer to form the air gap. Consequently, the fabrication of these micro-mechanical Fabry-Perots is time consuming, requires expensive and complicated film growth equipment (especially MBE), and is potentially costly.

We present a new fabrication technique to form micro-mechanical modulators that can be used to realize Fabry-Perots on a silicon substrate. This technique is simpler and potentially less expensive than all processes that have been reported to our knowledge. Furthermore, integration with inexpensive, well established, Si-based, transistors and photodetectors is made possible. The fabrication process requires only one mask level and uses a single oxide layer to provide the top mirror supporting structure and the electrical isolation. A cross-sectional schematic of the structure is shown in Figure 1-2.

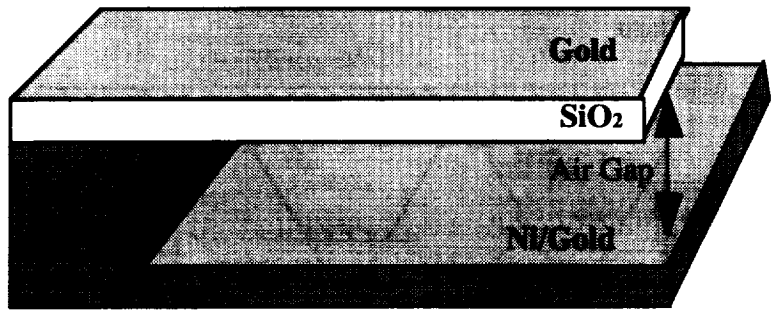

Figure 1-2. Cross-sectional diagram of the novel (111) silicon based micro-mechanical Fabry-Perot filter.

A (111) oriented silicon substrate is used. The movable top mirror is a cantilever made of high quality thermally grown SiO_2. A cantilever structure was chosen due to the much lower voltages required to bend the structure in comparison to the stretching of a membrane fixed on two or more ends. The formation of the air gap under the cantilever is accomplished by a combination of vertical RIE (Reactive Ion Etching) and lateral anisotropic selective KOH wet etching of the (111) silicon. The substrate itself provides the sacrificial layer. The metallization of the top mirror is carried out by gold evaporation while the bottom mirror is electroplated with nickel followed by gold.

The structure can function as both a filter and a photodetector in the 700–900 nm wavelength range by simply implanting or diffusing a p-n junction photodetector into the substrate under the bottom mirror. The filter can also operate in unattenuated transmission through the substrate at wavelengths longer than the 1100 nm cutoff wavelength of the silicon.

In comparison with the micro-mechanical Fabry-Perot filters currently being developed from the literature, this structure has the advantage of being simpler in construction and fabrication complexity. However, the utilization of simple metallic mirrors results in a performance tradeoff not suffered by Fabry-Perots using DBR mirrors. Fabry-Perots using metallic mirrors cannot provide both high finesse and high transmittance simultaneously due to optical absorption in the metal. That is, the effective mirror reflectivity is increased with a thicker metal layer which yields a higher finesse. However, the optical throughput is reduced. In light of this tradeoff, we present the simple structure as an inexpensive alternative to the DBR based Fabry-Perots for applications where the tradeoff can be tolerated.

We begin in Chapter 2 by presenting a theoretical description of the cantilever bending. The bending of the cantilever will be related to the physical characteristics of the structure and the applied voltage. A hysteretic behavior is predicted. However, it is shown to be avoidable if the applied voltages are below a threshold value. The optical filtering behavior of the structure is related to the device geometry and voltage. Numerical results are presented and predict reasonable device performance characteristics and reveal performance tradeoff issues.

In Chapter 3, the modulator fabrication process is described. A new method for cantilever undercutting using (111) Si wafers is presented. Mask design methods are presented that provide efficient undercutting of the oxide cantilever and the necessary electrical isolation between the mirrors. Details of the mirror metallization are presented. Top mirror metal evaporation and bottom mirror electroplating are discussed. Structural and processing problems will be revealed that result in the deviation of the mirror surfaces from perfect smoothness and flatness.

In Chapter 4, the experimental results for the micro-mechanical Fabry-Perots are presented. Results from a SEM study of the motion of the cantilever under bias and the spectral tuning characteristics of the filter are also presented. The spectra were measured as a function of applied bias. The spectral characterization includes tuning voltage versus transmission wavelength, linewidths, and on/off ratios. The frequency response characteristics of the modulator are also presented. The experimental results are compared to theoretical predictions.

Finally in Chapter 5 we summarize the results and suggest modulator design improvements that could

result in better filter performance.

References

1. Nathanson, H. C. and R. A. Wickstrom, A resonant gate silicon surface transistor with high-Q bandpass properties. App. Phys. Ltrs., **7**, p. 84, 1965.

2. Nathanson, H. C., et al., A resonant gate transistor, *IEEE Trans. on Elect. Dev.*, **ED-14**, p. 117, 1967.

3. Bassous, E., H. H. Taub, and L. Kuhn, Ink jet printing nozzle arrays etched in silicon, App. Phys. Ltrs., **31**, p. 135, 1977.

4. Wolber, W. G. and K. D. Wise, Sensor development in the microcomputer age, *IEEE Trans. Elect. Dev.*, **ED-26**, p. 1864, 1979.

5. Middelhoek, S., J. B. Angell, and D. J. W. Noorlag, *Microprocessors get integrated sensors*, IEEE Spectrum,. **17**(2), p. 42, 1980.

6. Hornbeck, L J., *Digital Light Processing and MEMS: An Overview* in *IEEE/LEOS 1996 Summer Topical Meetings: Optical MEMS And Their Applications*, Keystone, CO, pp. 7–8, 1996.

7. Chang-Hasnain, C. J., E. C. Vail, and M. S. Wu, *Widely -tunable micro-mechanical vertical cavity lasers and detectors* in *IEEE/LEOS 1996 Summer Topical Meetings: Optical MEMS and Their Applications*. 1996. Keystone, CO, pp. 43–44.

8. Choa, F.S., et al., InGaAs/InGaAsP integrated tunable detector grown by chemical beam epitaxy, *App. Phys. Ltrs.*, **63**(13), pp. 1836–1838, 1993.

9. Harris Jr., J. S., M. C. Larson, and A. R. Massengale, *Coupled -cavity laser diode with micromachined external mirrors* in *IEEE/LEOS 1996 Summer Topical Meetings: Optical MEMS and Their Applications*, Keystone, CO, pp. 31–32, 1996.

10. Larson, M .C. and J. S. Harris Jr., *Broadly-tunable, narrow linewidth resonant cavity light emitter* in *53rd Annual Device Research Conference*, Charlottesville, VA, pp. 130–131, 1995.

11. Lo, Y. H., et al., *Integrated micro-optical interferometer arrays* in *IEEE/LEOS 1996 Summer Topical Meetings: Optical MEMS and Their Applications*, Keystone, CO, pp. 25–26, 1996.

12. Tran, A. T. T. D., et al., *Electro-mechanically tunable micro Fabry-Perot filter array* in *53rd Annual Device Research Conference*, Charlottesville, VA, pp. 128–129, 1995.

13. Tran, A. T. T. D., et al., *Surface Micromachined Fabry-Perot Tunable Filter*. Photonics Technology Letters, **8**(3), pp. 393–395, 1996.

14. Uenishi, Y., *Coupled-cavity laser diode with micromachined external mirrors* in *IEEE/LEOS 1996 Summer Topical Meetings: Optical MEMS and Their Applications*, Keystone CO, pp. 33–34, 1996.

15. Fricke, J. and E. Obermeier, *Surface Micromachined Accelerometer Based On A Torsional Moving Structure* in *The 8th International Conference on Solid-State Sensors and Actuators*, Stockholm, Sweden, pp. 542–545, 1995.

16. Goldman, K. and M. Mehregany, *A Novel Micromechanical Temperature Memory Sensor* in *The 8th International Conference on Solid-State Sensors and Actuators*, Stockholm, Sweden, pp. 132–135, 1995.

17. Neikirk, Y. K. A. D. P., Monolithically integrated optically interrogated pressure microsensor, *Acoustic Soc. America*, p. 2353, 1992.

18. Wipiejewski, T., et al., Tunable extremely low threshold vertical cavity laser diodes, *IEEE Photonics Ltrs.*, **5**(8), pp. 889–892, 1993.

19. Martinet, E., et al., Electrical tunability of infrared detectors using compositionally asymmetric GaAs/AlGaAs multiquantum wells, *App. Phys. Ltrs.*,. **60**(7), pp. 895–897, 1992.

20. Wu, M. S., et al. *Widely tunable micromachined gallium arsenide fabry-perot filters* in *IEEE/LEOS*, Keystone CO, 1994.

21. Petersen, K. E., *Silicon as a mechanical material*, Proceedings of the IEEE, **70**(5), pp. 420–457, 1982.

22. Mastrangelo, C. H. and C. H. Hsu, *Mechanical Stability and Adhesion of Microstructures: Part I: Basic Theory*. Journal of Micro-mechanical Systems, **2**(1), pp. 33–43, 1993.

23. Brackett, C. A., *Dense wavelength division multiplexing networks: Principles and applications*, IEEE Journal of Selected Areas in Communications, **8**(6), pp. 948–964, 1990.

24. Wu, M. S., et al., Widely and continuously tunable micromachined resonant cavity detector with wavelength tracking, *IEEE Photonics Tech. Ltrs.*, **8**(1), pp. 98–100, 1996.

25. Petersen, K. E., Micromechanical light modulator array fabricated on silicon, *App. Phys. Ltrs.*, **31**(8), pp. 521–523, 1977.

II. Electro-Mechanical and Optical Theory

2.1 Introduction

In this chapter, the theory describing the behavior of the voltage tunable Fabry-Perot filters is developed and presented. The analysis is performed in two steps. First, the electro-mechanical behavior of the cantilever structure is analyzed. In this section, the voltage induced bending of the cantilever is calculated. The bending theory is used to relate the applied voltage to the size of the air gap under the cantilever mirror. The second part of the analysis is the calculation of the optical spectra transmitted and reflected by the Fabry-Perot. Given the Fabry-Perot geometry and functional dependence of the air gap on voltage, the optical filtering characteristics are calculated. In section 2.4 numerical results are presented for several cases. The numerical results provide an understanding of how the tuning behavior is affected by the applied voltage and geometry of the structure, and what the tradeoff issues are. In Chapter 4, the theory presented in this chapter will be compared to the experimental results.

2.2 Electro-Mechanical Theory

2.2.1 Derivation of the Cantilever Bending Equation

The bending of the cantilever as a function of voltage is described in this section. Figure 2-1 shows a schematic of the cantilever structure described in the analysis with relevant symbol definitions. The cantilever structure is assumed to be of constant cross-section. However, the theory is amenable to more complicated geometries. It is also assumed that ideally the cantilever is straight and parallel to the lower mirror with zero bias applied to the structure.

The structure consists of a gold coated cantilever suspended above a gold coated silicon substrate. The cantilever forms the top mirror for the Fabry-Perot while the gold coated Si below provides the bottom mirror. The length of the cantilever is L. It has a width W, and oxide thickness h_{ox}. The height of the cantilever above the bottom mirror with zero bias V is h_{co}. y is defined as the height of the cantilever above the bottom mirror. With an applied bias y is a function of the lateral position x.

As mentioned in Chapter 1 the basis for the cantilever bending is a capacitive electrostatic force. We can treat the cantilever structure as a capacitor since the SiO_2 electrically insulates the top mirror metal from the Si based mirror below. When a voltage is applied between the cantilever metal and the metal on

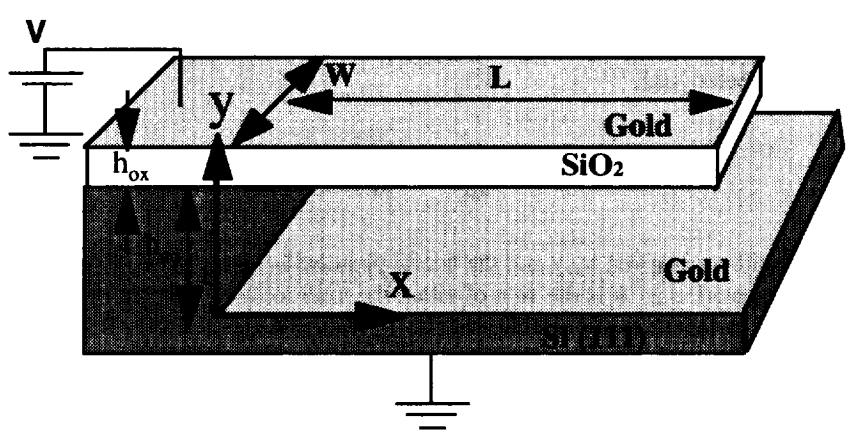

Figure 2-1. Cantilever schematic for the electro-mechanical analysis.

the silicon, opposite charges build up on the capacitor plates producing an attractive electrostatic force that pulls the cantilever toward the silicon.

The force between the cantilever and the Si due to the voltage V can be derived from the equation of stored energy in a capacitor C.

$$U = \frac{1}{2}CV^2 \tag{2-1}$$

The force F(y), can be obtained by differentiating the stored energy U with respect to the capacitor spacing y. The differentiation is performed while holding the capacitor voltage constant. That is, the voltage is provided by an ideal source. Differentiating gives

$$F(y) = \frac{dU}{dy} = \frac{1}{2}V^2\frac{dC}{dy} \tag{2-2}$$

Here the capacitance is the series combination of the cantilever oxide capacitor and the air gap capacitor between the bottom of the cantilever and the metal coated Si below.

$$\frac{1}{C} = \frac{1}{C_{ox}} + \frac{1}{C_{air-gap}}, \quad C = \frac{C_{ox}C_{air-gap}}{C_{ox} + C_{air-gap}}, C_{ox} = \frac{\varepsilon_o\varepsilon_{rox}WL}{h_{ox}}, \quad C_{air-gap} = \frac{\varepsilon_o WL}{y} \tag{2-3}$$

$\varepsilon_o \rightarrow$ *free space permittivity*

$\varepsilon_{rox} \rightarrow$ *SiO_2 relative permittivity*

Differentiating the series capacitance combination and substituting into the force equation gives

$$F(y) = \frac{dU}{dy} = -\frac{1}{2}V^2\frac{\varepsilon_o WL}{\left[y + \frac{h_{ox}}{\varepsilon_{rox}}\right]^2} \tag{2-4}$$

The force is shown to be proportional to the square of the ratio of the voltage to the air gap spacing for small h_{ox}/ε_{rox}.

The bending of a cantilever under the influence of an arbitrary loading function is given by the cantilever differential equation [1, 2]. This equation provides the steady state or static profile of the cantilever under a distributed load.

$$\frac{d^2y}{dx^2} = \frac{M(x)}{EI} \tag{2-5}$$

The height of the cantilever is given by y and the lateral position is given by x as in Figure 2-1. M(x) is the total moment at a position x. It is the sum of either the total loading moment or torque to the left of x or too the right of x. E is the elasticity modulus of the cantilever material and is frequently called Young's modulus. In this case E is the elasticity modulus of the oxide. The elasticity of the composite beam is minimally affected by the addition of the thin gold layer. I is the cross-sectional area moment of inertia of the beam (a cross-sectional area defined by h_{ox} and the width W) and describes the beams stiffness to torsional bending. Here the moment is taken about the central z axis of the beams cross-section as shown in Figure 2-2.

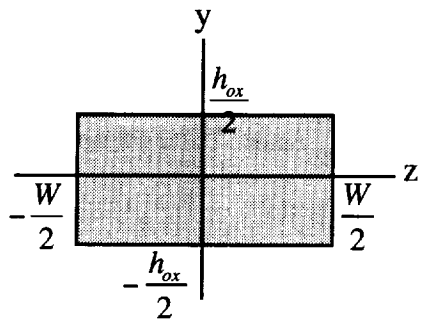

Cantilever Beam
Cross-Section

Figure 2-2. Diagram used for the calculation of the moment of inertia of the cantilever beam.

For the constant cross-section cantilever shown in Figure 2-1, I is given by

$$I = \int_{y=-\frac{h_{ox}}{2}}^{y=\frac{h_{ox}}{2}} y^2 dy \int_{z=-\frac{W}{2}}^{\frac{W}{2}} dz = \frac{Wh_{ox}^3}{12} \tag{2-6}$$

M(x) can be related to the electrostatic force

$$M(x) = \int_{x'=x}^{L} \frac{F(y(x))}{L}(x'-x)dx' = -\varepsilon_o W \frac{V^2}{2} \int_{x'=x}^{L} \frac{(x'-x)}{\left[y(x') + \frac{h_{ox}}{\varepsilon_{rox}}\right]^2} dx' \tag{2-7}$$

The resultant cantilever differential equation is given by

$$\frac{d^2y}{dx^2} = -\frac{6\varepsilon_o}{Eh_{ox}^3} V^2 \int_{x'=x}^{L} \frac{(x'-x)}{\left[y(x') + \frac{h_{ox}}{\varepsilon_{rox}}\right]} \tag{2-8}$$

One immediately observes that the beam bending under the influence of the electrostatic force does not depend on the width W of the structure, since it has dropped out of the expression. This is a consequence of both the stiffness of the beam and the electrostatic force depending linearly on W. It will also be shown that the width does not affect the frequency response either. The classification of the equation is a second order nonlinear differential equation. It cannot be solved exactly for an analytic solution. Instead, it must be solved using numerical methods.

The numerical solution solves the differential equation by using trapezoidal integration and iteration to provide convergence of the y input values to y output values. That is, first assume that y(x) is approximated by h_{co}, the zero voltage air gap. Next, the moment is integrated providing y''(x). Integrate y''(x) twice to provide y(x). The values for y(x) are plugged into the moment generating equation again. The iteration is performed until the y(x) solution does not change greater than 1 part in a billion. The moment integral provides a pulling down of the guessed input values toward the real solution.

Convergence occurs, since the first guess for the y values h_{co} is larger than the real solution .

An analytical solution would provide some needed insight to the cantilever's bending sensitivity to voltage as a function of the structures geometry. If one assumes in the differential equation, that the height y(x) does not vary significantly from the initial air gap h_{co} (with 0 Volts), y(x) in the denominator of the integral can be replaced by the constant h_{co} without great loss of accuracy. The replacement provides an analytical solution which is valid for small V/h_{co} ratios. The small voltage or quadratic approximation is

$$y(x) = h_{co} - \frac{6\varepsilon_o}{Eh_{ox}^3} \frac{V^2}{\left[h_{co} + \frac{h_{ox}}{\varepsilon_{rox}}\right]^2} \left[\frac{L^2x^2}{4} - \frac{Lx^3}{6} + \frac{x^4}{24}\right] \tag{2-9}$$

The maximum deflection of the cantilever beam occurs at its tip. The position of the tip is given by

$$y(L) = h_{co} - \frac{3}{4}\frac{\varepsilon_o}{Eh_{ox}^3} \frac{V^2}{\left[h_{co} + \frac{h_{ox}}{\varepsilon_{rox}}\right]^2} L^4 \tag{2-10}$$

As shown, the maximum displacement of the beam is proportional to the fourth power of the length. The dependence of the bending to h_{ox} is inverse to the 5th power for small initial cavity height h_{co}. Also, for large h_{co}/h_{ox}, the displacement goes as the square of the ratio of the voltage to the initial cavity height.

2.2.2 Derivation of the Cantilever's Frequency Response

Another crucial performance metric for the micro-mechanical Fabry-Perot is its deflection response as a function of the frequency of the applied voltage. From this characteristic we also gain knowledge of the structures modulation bandwidth which can be used for comparison. Here we present a theoretical method for calculating the dependence of the response characteristic and bandwidth on the device geometry. In calculating the response characteristic, a combination of rigorous and first order theory is used. A completely rigorous analysis would require extensive numerical calculations for solutions of transcendental functions. It will be shown in Chapter 4 that the approximate theory predicts a response function that is very consistent with the experimental data. First the natural resonant frequencies of a freely vibrating cantilever are calculated. The model rigorously describes the distributed mass and elasticity of the cantilever. Next a response function to a sinusoidal driving force is formulated based on a linear-spring point-mass system. The response function also includes a damping term due to air resistance. The response function includes only the affects of the 1st natural frequency of the cantilever. The natural frequency in the first order response function is then replaced by the fundamental or 1st natural frequency calculated using the rigorous theory. This function provides a prediction for the response characteristic of the cantilever and its −3 dB bandwidth. Justification of this model can be obtained from the experimental results. Like the frequency response calculated with the linear-spring point-mass model, the measured response for the cantilevers is low pass. Furthermore, the measured response only shows a significant contribution from the 1st natural frequency. The strength of the higher order natural frequencies are relatively small probably due to the viscous air damping of the cantilever.

In general, to calculate exactly the analytic solution to the motion of a freely vibrating cantilever one uses the partial differential equation of motion for the lateral vibration of a beam [3]

$$\frac{\partial^2}{\partial x^2}\left(EI\frac{\partial^2 y}{\partial x^2}\right) = -\rho_{eff}.Wh_{ox}\frac{\partial^2 y}{\partial t^2} \tag{2-11}$$

$$\rho_{eff.} \rightarrow \textit{effective density of the beam}$$
$$\rho_{Au} \rightarrow \textit{density of gold layer}$$
$$h_{Au} \rightarrow \textit{thicknes of gold layer}$$

$$\rho_{eff.} = \frac{\rho_{SiO_2} h_{ox} + \rho_{Au} h_{Au}}{h_{ox}} \tag{2-12}$$

Here all variable definitions are the same as previously stated except for the addition of the effective density. The effective density includes contributions to the mass of the cantilever from both the thin gold layer (10 to 50 nm) and the thicker oxide layer (850 nm). In the calculation of the bending of the cantilever, the contribution of the gold layer to the stiffness was negligible. This is a consequence of the gold layer being much thinner than the oxide layer and the elasticity constant of gold 7.8×10^{10} N/m^2 being comparable to that of SiO_2 7.3×10^{10} N/m^2 [4]. However, when calculating the mass of the structure the gold must be included for an accurate result. Gold's density is a factor of 7.7 higher than that of oxide, 19.3 g/cm^3 versus 2.5 g/cm^3 respectively [4, 5]. Consequently the gold layer's contribution to the mass is significant. The solution to the motion equation is separable and is of the form

$$y(x,t) = X(x) Cos(\omega_n t + \theta) \tag{2-13}$$

At this point a new constant is defined

$$\kappa^4 = \frac{\omega_n^2 \rho_{eff.} W h_{ox}}{EI} \tag{2-14}$$

Here ω_n is one of the natural frequencies of oscillation for the cantilever beam. Substituting Eqs. 2-13 and 2-14 into the vibration equation and dividing by $Cos(\omega_n t + \theta)$ gives

$$\frac{d^4 X(x)}{dx^4} = \kappa^4 X(x) \tag{2-15}$$

The solution to equation 2-15 is of the form

$$X = A_1 Sin(\kappa x) + A_2 Cos(\kappa x) + A_3 Sinh(\kappa x) + A_4 Cosh(\kappa x) \tag{2-16}$$

The constants A_1, A_2, A_3, and A_4 are found by the supporting conditions on the ends of the cantilever beam. In finding the solutions to Eq. 2-16 it is more convenient to redefine the constants and write it in the form

$$\begin{aligned} X = {} & A[Cos(\kappa x) + Cosh(\kappa x)] + B[Cos(\kappa x) - Cosh(\kappa x)] \\ & + C[Sin(\kappa x) + Sinh(\kappa x)] + D[Sin(\kappa x) - Sinh(\kappa x)] \end{aligned} \tag{2-17}$$

This form will reduce the number of constants in the final solution. The conditions on the ends of the cantilever are as follows.

The deflection is proportional to X and is zero at the built-in end.

The slope is proportional to X' and is zero at the built-in end.

The moment is proportional to X" and is zero at the free end.

The shear is proportional to X''' and is zero at the free end.

The required derivatives are

$$X' = \kappa A\left[-Sin(\kappa x) + Sinh(\kappa x)\right] + \kappa B\left[-Sin(\kappa x) - Sinh(\kappa x)\right]$$
$$+\kappa C\left[Cos(\kappa x) + Cosh(\kappa x)\right] + \kappa D\left[Cos(\kappa x) - Cosh(\kappa x)\right] \tag{2-18}$$

$$X'' = \kappa^2 A\left[-Cos(\kappa x) + Cosh(\kappa x)\right] + \kappa^2 B\left[-Cos(\kappa x) - Cosh(\kappa x)\right]$$
$$+\kappa^2 C\left[-Sin(\kappa x) + Sinh(\kappa x)\right] + \kappa^2 D\left[-Sin(\kappa x) - Sinh(\kappa x)\right] \tag{2-19}$$

$$X''' = \kappa^3 A\left[Sin(\kappa x) + Sinh(\kappa x)\right] + \kappa^3 B\left[Sin(\kappa x) - Sinh(\kappa x)\right]$$
$$+\kappa^3 C\left[-Cos(\kappa x) + Cosh(\kappa x)\right] + \kappa^3 D\left[-Cos(\kappa x) - Cosh(\kappa x)\right] \tag{2-20}$$

Applying the cantilever end conditions to the equations results in

$$0 = A \tag{2-21}$$

$$0 = C \tag{2-22}$$

$$0 = B\left[Cos(\kappa L) + Cosh(\kappa L)\right] + D\left[Sin(\kappa L) + Sinh(\kappa L)\right] \tag{2-23}$$

$$0 = B\left[Sin(\kappa L) - Sinh(\kappa L)\right] - D\left[Cos(\kappa L) + Cosh(\kappa L)\right] \tag{2-24}$$

Here A and C are zero due to the conditions on the built-in end of the cantilever. There are still two remaining constants which have not been determined B, D, and the spatial frequency κ is unknown. Once the spatial frequency of a given mode has been determined, one of the unknown constants can be found in terms of the other. There is always one undetermined constant, which can be evaluated only if the amplitude of the vibration is known. We will not be concerned with this constant since we are calculating the normalized response of the cantilever. Using Eqs. 2-23 and 2-24, expressions relating the spatial frequency to the ratio of D to B can be derived.

$$\frac{D}{B} = -\frac{Cos(\kappa L) + Cosh(\kappa L)}{Sin(\kappa L) + Sinh(\kappa L)} = \frac{Sin(\kappa L) - Sinh(\kappa L)}{Cos(\kappa L) + Cosh(\kappa L)} \tag{2-25}$$

Rearranging Eq. 2-25 results in

$$-1 = Cos(\kappa_n L)Cosh(\kappa_n L) \tag{2-26}$$

Eq. 2-26 provides numerical solutions for the spatial frequency given a cantilever length L. Solutions to the product of spatial frequency and the length must be obtained using numerical methods. The first few solutions are

$$\kappa_1 L = 1.875$$
$$\kappa_2 L = 4.694$$
$$\kappa_3 L = 7.855$$
$$\kappa_4 L = 10.996 \tag{2-27}$$

Of most significance in calculating the response characteristic of spring-mass system is the fundamental natural frequency ω_1. The response of spring-mass system is basically low pass. The fundamental frequency is the first and most dominant pole in the response characteristic. Substituting $\kappa_1 L$ in Eq 2-27 into Eq. 2-14 gives an expression for the fundamental natural frequency.

$$\omega_1 = 2\pi f_1 = 1.015\sqrt{\frac{E}{\rho_{eff.}}}\frac{h_{ox}}{L^2} \tag{2-28}$$

Equation 2-11 is the differential equation for a freely vibrating cantilever beam oscillating only in its resonant frequencies. To obtain the response of the beam to a continuous external force the external force must be included in Eq 2-12 and the particular solution solved for in addition to the homogeneous equation. The solutions to the particular solution are found numerically and are quite cumbersome to calculate. For an exact solution to the forced oscillator a finite element mechanics program such as MSC/NASTRAN should be used (MSC/NASTRAN is a registered trademark of MacNeil Schwendler Corporation) [6]. However, the rigorously calculated 1st natural frequency can be used to adequately model the forced response of the cantilever when used in combination with the linear-spring point-mass forced oscillator model. As stated previously from the knowledge of the experimental results the affect of the higher order resonances on the response are relatively insignificant in comparison to the 1st natural frequency. Consider the simple harmonic oscillator differential equation.

$$m\frac{d^2y}{dt^2} + \gamma\frac{dy}{dt} + Ky = F_{applied}$$
$$y \rightarrow displacement$$
$$t \rightarrow time$$
$$m \rightarrow point\ mass$$
$$\gamma \rightarrow damping\ coefficient$$
$$K \rightarrow linear\ spring\ constant$$
$$F_{applied} \rightarrow applied\ force \tag{2-29}$$

This equation assumes a point-mass, a linear spring, and damping. In the case of the cantilever structures, the damping is caused by viscous air damping. Next, assume a sinusoidal applied force and sinusoidal displacement of the same frequency (this requires the spring to be linear)

$$F_{applied} = \tilde{F}e^{j\omega t}, y = \tilde{Y}e^{j\omega t} \tag{2-30}$$

Here the complex F and Y represent the complex amplitude of the applied force and displacement respectively. ω is the angular frequency. Plugging Eq. 2-30 into Eq. 2-29 and calculating the displacement response yields:

$$\left|\tilde{Y}\right| = \frac{\left|\tilde{F}\right|}{\left(\omega^4 + \omega^2\left(\frac{\gamma^2}{m^2} - \frac{2K}{m}\right) + \frac{K^2}{m^2}\right)^{\frac{1}{2}}} \tag{2-31}$$

Next recognize that the natural frequency of a linear-spring point-mass system is given by

$$\omega_1 = 2\pi f_1 = \frac{1}{2\pi}\sqrt{\frac{K}{m}} \tag{2-32}$$

The natural frequency has been subscripted to be the fundamental or first natural frequency. A linear spring has only one natural frequency. We could obtain a resonance frequency based on the linear-spring point-mass model by taking the derivative of Eq. 2.10 with respect to the force. However, this would result in loss of accuracy since the cantilever is a distributed system. Instead we use the more accurate fundamental natural frequency calculated by the rigorous theory. Rewriting Eq. 2-31 and normalizing to the DC response yields

$$\left|\tilde{Y}\right| = \frac{\omega_1^2}{\left(\omega^4 + \omega^2\left(\frac{\gamma^2}{m^2} - 2\omega_1^2\right) + \omega_1^4\right)^{\frac{1}{2}}} = \frac{f_1^2}{\left(f^4 + f^2\left(\frac{\gamma^2}{(2\pi m)^2} - 2f_1^2\right) + f_1^4\right)^{\frac{1}{2}}} \tag{2-33}$$

To numerically calculate the response all that remains to determine is the damping factor. The damping results from the viscosity of the air displaced by the motion of the cantilever. Theoretical calculation of the damping factor is generally very difficult. Consequently in this analysis, the damping factor will be determined from the experimental data. At this point another observation is key. In the undamped case we calculated the natural frequency, the frequency of maximum displacement amplitude for the cantilever. In the case of a damped oscillator the frequency of maximum displacement or resonance frequency is reduced in comparison to the undamped case. The shifted resonance is found by minimizing the denominator of the response function of Eq. 2-33. The shifted resonance is

$$\omega_R = \sqrt{\omega_N^2 - \frac{\gamma^2}{2m^2}} \tag{2-34}$$

For our structures (from experimental measurements) the shift is very small due to small value of the factor containing the damping term relative to the square of the natural frequency. The frequency shift for our structures is about 4%. Another useful quantity is the -3 dB frequency. Setting Equation 2-33 equal to one-half gives

$$f_{-3dB}^2 = -\frac{1}{2}\left(\frac{\gamma^2}{(2\pi m)^2} - 2f_1^2\right) + \frac{1}{2}\sqrt{\left(\frac{\gamma^2}{(2\pi m)^2} - 2f_1^2\right)^2 + 12f_1^4} \tag{2-35}$$

An approximate and simple expression for the −3 dB frequency can be found provided again that the term containing the damping factor in Eq. 2-35 is much less that containing the fundamental natural frequency.

$$f_{-3dB} \approx \sqrt{3}f_1, provided\ \frac{\gamma^2}{(2\pi m)^2} << 2f_1^2 \tag{2-36}$$

2.2.3 Numerical Results For the Cantilever Bending and Frequency Response

In this section, theoretical numerical results for the cantilever structure shown in Figure 2-1 are presented. The material constants used in the electro-mechanical calculations are listed in Table 2-1.

Table 2-1. Material Constants Used in the Bending Theory and Frequency Response Calculations.

Parameter	Symbol	Value	References
SiO_2 Elasticity Modulus (Fused Silica/Optical Fiber)	E	7.3×10^{10} N/m^2	[7]
SiO_2 Density (Fused Silica/Optical Fiber)	ρ_{SiO2}	2.5 g/cm^3	[7]
SiO_2 Relative Permittivity	ε_{SiO2}	3.9	[5]
Au Density	ρ_{Au}	19.3 g/cm^3	[4]
Au Elasticity Modulus		2.5 g/cm^3	[4]

Figure 2-3 shows the cantilever air gap, y as a function of lateral position x for a cantilever with initial air gap h_{co} = 1 μm.. The length of the cantilever is 100 μm. Profiles are shown for both 2.5 and 5 volt bias. A bias of 2.5 V provides 68 nm of bending at the tip as indicated by both the numerical and low voltage solutions. The angle of the cantilever tip is 0.04°. An application of 5 V provides 472 nm of bending at the tip with an angle of 0.27°. The low voltage solution no longer applies and grossly underestimates the tip bending by a factor of 2. Note that the long length of the cantilever ensures that the pitch angle is small for a given displacement. A small angle is necessary to provide for a stable and high finesse optical resonator. Figure 2-4 shows the profile for the same cantilever except the initial air gap has been increased to 4.0 μm.

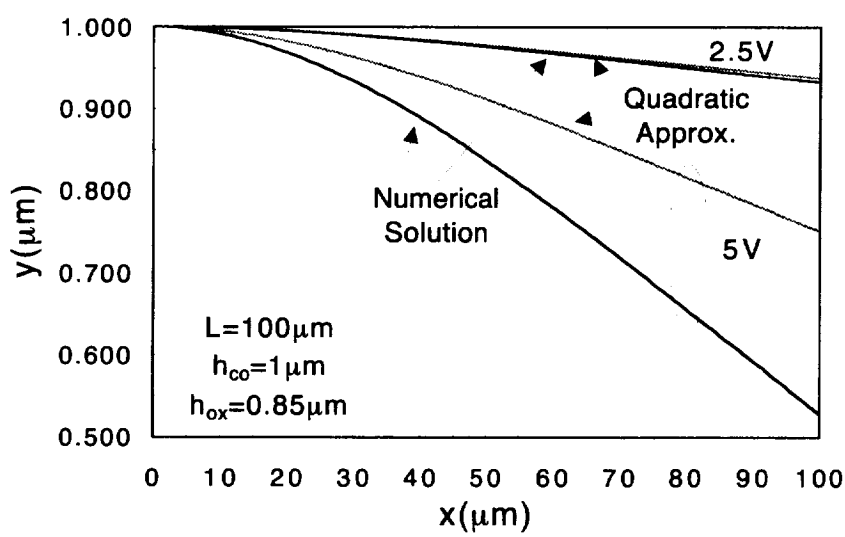

Figure 2-3. Cantilever profiles for 2.5 and 5.0 volt bias. The cantilever length is 100 μm and has a 0 voltage air gap of 1 μm. The oxide thicknesses is 0.85 μm.

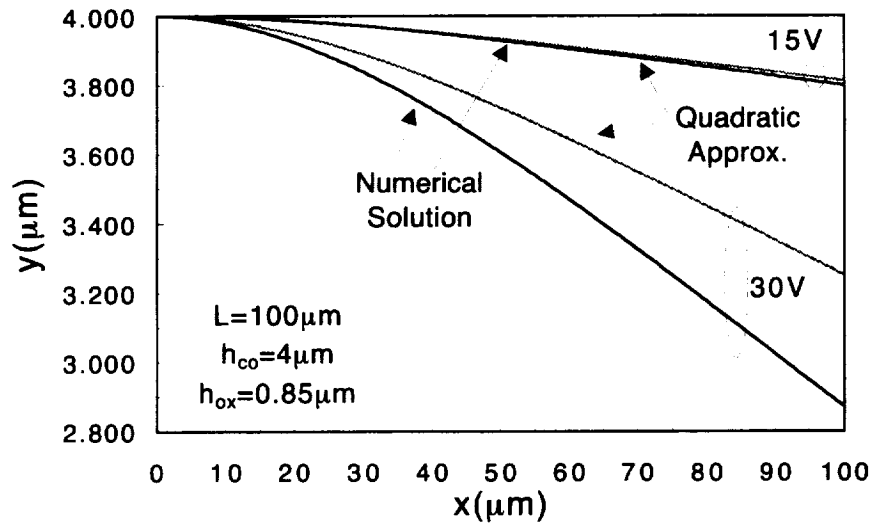

Figure 2-4. Cantilever profiles for 15 and 30 volts. The cantilever length is 100 μm and has a 0 voltage air gap of 4 μm.

An application of 15 V is required to bend the cantilever 200 nm and 30 V bends it 1130 nm. The pitch angles are 0.11° and 0.64° respectively. The 4 μm cantilever has a much smaller bending sensitivity to voltage than the 1 μm cantilever. A 2.5 V bias applied to the 1 μm cavity provides 68 nm of bending at the tip. Whereas the same 2.5 V bias provides only 4.3 nm of bending for the 4 μm cavity. Recall, from the quadratic approximation, that the bending goes as

$$Bending \propto \frac{1}{h_{co}^2} \tag{2-37}$$

This implies that a 1 μm air gap cantilever will bend 16 times more than a 4 μm cantilever for the same voltage.

$$\frac{y_{hco=1\mu m}}{y_{hco=4\mu m}} = \frac{4^2}{1^2} = 16 \tag{2-38}$$

This suggest that the initial air gap should be minimized to provide the highest air gap change for a given voltage (more spectral shift). The gain in voltage sensitivity does not come at the expense of decreased bandwidth since the bandwidth does not depend on the air gap. This is contrary to a cantilever length increase which results in larger sensitivity but at the expense of a lower bandwidth. Additionally, as will be discussed in the optical theory section, smaller cavity lengths result in a larger free spectral range.

Figure 2-5 shows the air gap at the tip of the cantilever as a function of applied voltage for a h_{co} = 1 μm cantilever. The graph shows the results for both forward and backward sweeps of the slowly varying DC voltage. As the voltage is swept from 0 to 5 volts, the air gap decreases from 1 μm to .53 μm. A small increase beyond 5 volts results in a "snapping" down of the cantilever into contact with the bottom Si mirror. That is, there are no stable positions for the cantilever between 0 and 0.53 μm. This behavior has been observed by others [7–10]. The unstable behavior is the result of a rapid build up of electrostatic force at the cantilever tip as it is moved closer to the lower capacitor plate or mirror.

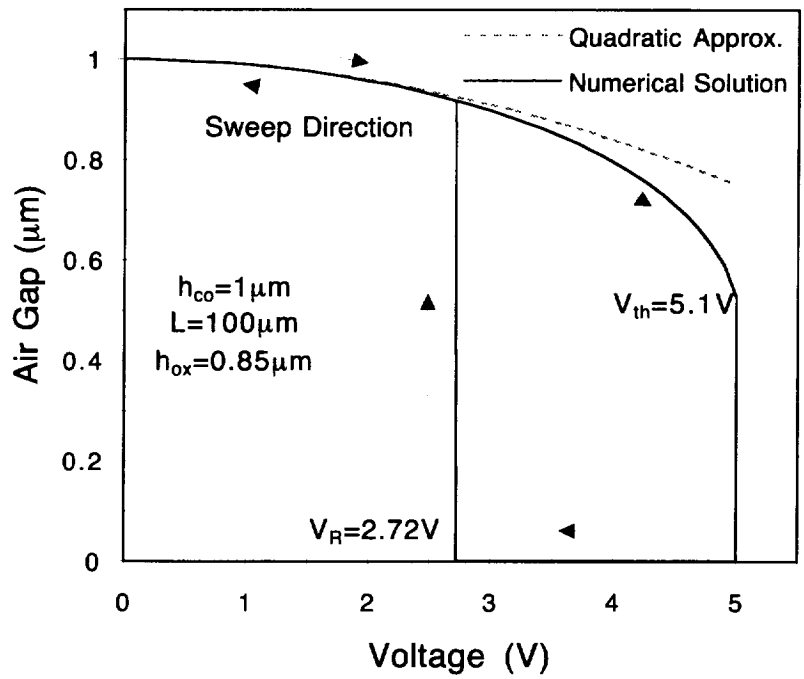

Figure 2-5. The position of the cantilever tip as the bias is swept in the forward and reverse directions for a h_{co} = 1μm air gap cantilever.

The voltage for which this occurs is defined as V_{th} An approximation for V_{th} as a function of the geometry of the cantilever structure can be derived by assuming the cantilever bending quadratic as a function of lateral position and voltage. The expression is [10]

$$V_{th} = \sqrt{\frac{3Eh_{ox}^3 h_{co}^3}{10\varepsilon_o L^4}} \tag{2-39}$$

This equation predicts V_{th} to be 3.9 V which is lower than that predicted by the numerical solution. The approximation is better for large h_{co}/h_{ox} ratios. The snap down occurs approximately when the end of the cantilever has been bent down 1/3 of the initial air gap.

Following snap down, the voltage is swept in the reverse direction. The reverse sweep indicates a hysteretic behavior. The cantilever tip does not immediately rise as the voltage is decreased below V_{th}. Instead a reduction of the voltage to V_R = 2.71 V is required to release the cantilever (V_R = release voltage). Below 2.72 V the forward and reverse voltage sweeps are identical.

Figure 2-6 shows the same characteristic for the 4 μm air gap cantilever. The same hysteretic behavior is observed. The threshold voltage is a much higher 32 V which is equivalent to that predicted by the threshold voltage equation. The release voltage is 5.77 V.

Hysteresis is generally an unwanted characteristic. Figure 2-7 shows the deflection of the cantilever tip as a function of voltage for initial air gaps of 1, 2, and 4 μm. The voltage was swept in both forward and reverse directions but not allowed to go beyond V_{th}. Hysteresis was not observed under this constraint $V < V_{th}$: the curves retraced exactly. This graph also shows clearly the increased voltage sensitivity (larger slope) of the smaller air gap cantilever structures over the larger air gap cantilevers.

A plot of the frequency response characteristic that was calculated using Eq. 2-33 is shown in Figure 2-8. Here the normalized displacement response Y is plotted against drive voltage frequency. The constants chosen for Eq 2-13 to generate the graph were representative of one of the fabricated cantilever structures. The oxide cantilever was 101 μm long by 20 μm wide with a thickness of 0.85 μm.

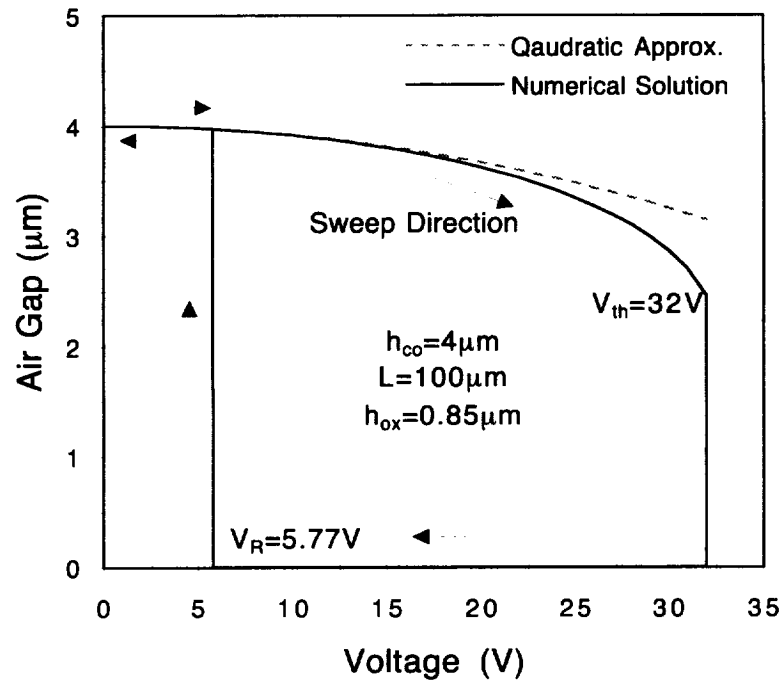

Figure 2-6. The position of the cantilever tip as the bias is swept in the forward and reverse directions for a 4 μm air gap cantilever.

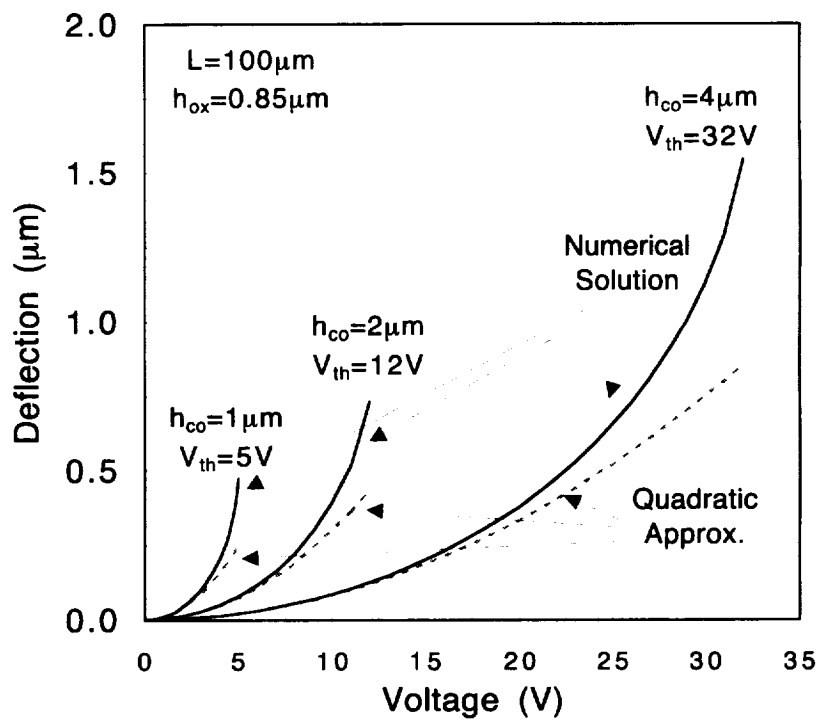

Figure 2-7. Forward and reverse sweep of the bias voltage under the $V < V_{th}$ constraint for cantilevers with h_{co} equal to 1, 2, and 4 μm.

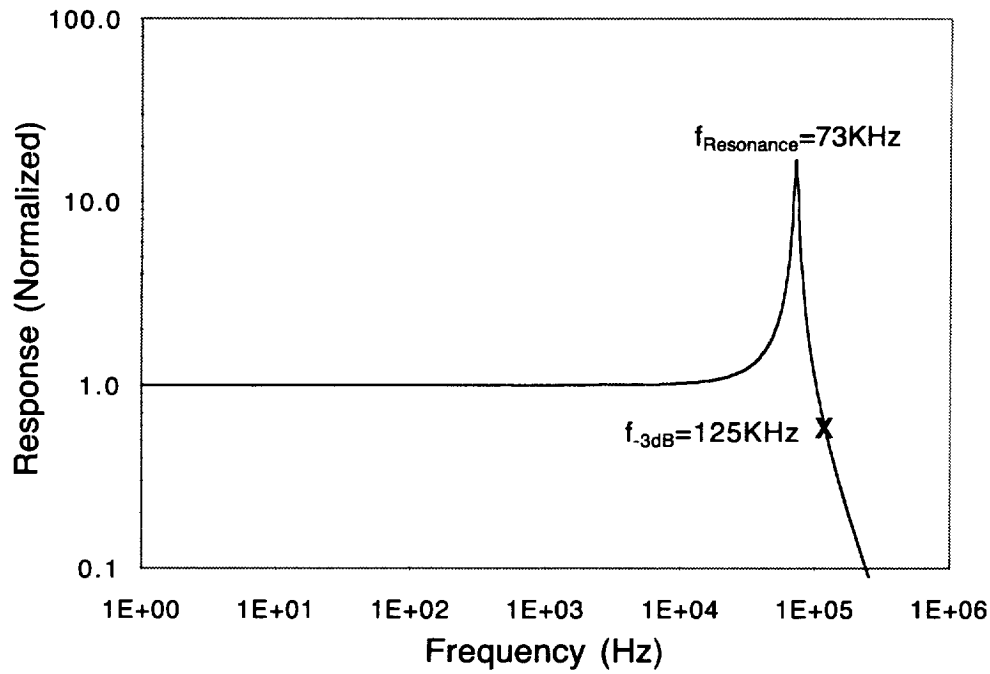

Figure 2-8. Theoretical Bode plot showing the tip displacement response for a cantilever modulator. The theory models the cantilever as a linear-spring point-mass system that is described by Eq. 2-13. The oxide cantilever was 101 μm long by 20 μm wide with a thickness of 0.85 μm.

The response is flat from DC until the frequency approaches the resonant frequency where the response quickly rises and falls to zero. The behavior will be shown to be consistent with the experimental measurements presented in Chapter 4. A damping factor of 1.35×10^{-7} Kg-Hz was used since it was consistent with the experimental results for this structure. Here the −3 dB frequency is 125 KHz whereas the resonant frequency is 72.675 KHz. The resonant frequency is actually slightly lower than the natural frequency which is 72.737 KHz due to the shift caused by the damping factor. Note that the approximate relation of Eq. 2-36 between the −3dB frequency and the resonant frequency applies due to the low damping.

$$f_{-3dB} \approx \sqrt{3} f_1 = \sqrt{3}(73KHz) = 126KHz \approx 125KHz \tag{2-40}$$

In applications where the cantilever may be used as an indirect optical modulator or for fast wavelength tracking and tuning, high speeds may be required. The −3 dB bandwidth and cantilever tip deflection were calculated for cantilever lengths ranging from 1 to 150 μm. The bandwidth calculations were made using Eq 2-33. The small reduction of the bandwidth due to the damping factor was ignored in the calculations. The tip deflection is linearly related to the optical tuning range and is discussed in section 2.3. The results are shown in Figure 2-9. The tip deflections were calculated at 2.5 V bias. A comparison between the two curves shows a tradeoff between bandwidth and deflection. A 100 μm long cantilever provides a bandwidth of 125 KHz and a deflection of 62 nm. Whereas, a 50 μm long cantilever provides a much higher 473 KHz bandwidth and only 4 nm of deflection. However, both a high bandwidth and a reasonable deflection could be obtained if higher voltages are used.

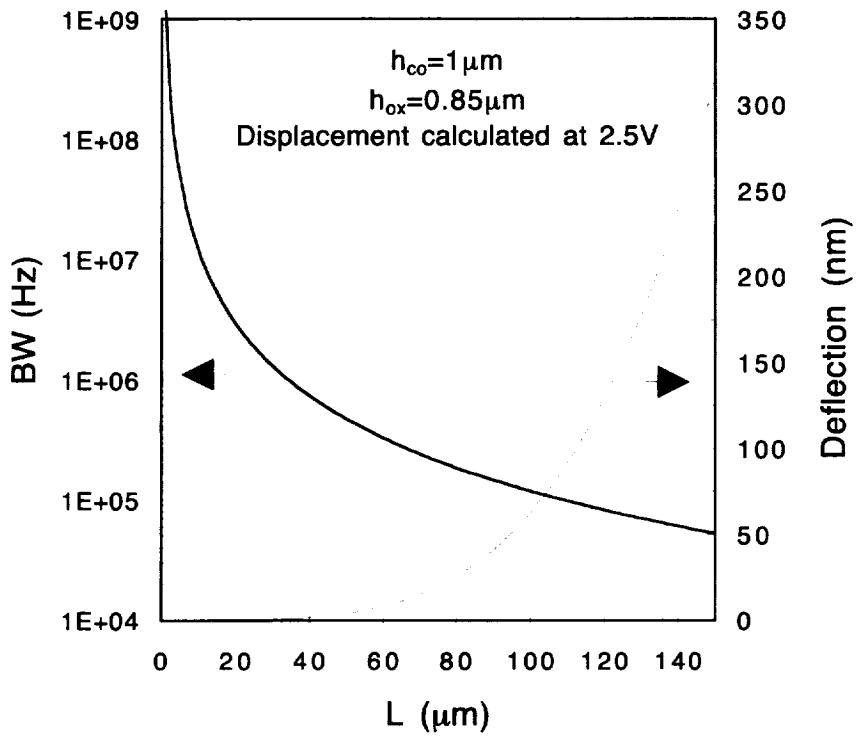

Figure 2-9. Bandwidth and cantilever tip deflection as a function of cantilever length.

2.3 Optical Theory

2.3.1 Introduction

In the previous section, the cavity length or air gap of the Fabry-Perot was related to the voltage, geometry, and material constants of the cantilever structure. The next step of the analysis is the calculation of the transmittance and reflectance of the Fabry-Perot structure for a given air gap, i.e., relating the spectral characteristics of the optical filter to the tuning voltage.

In modeling the cantilever Fabry-Perot spectra, it is assumed that the structure is composed of an ideal stack of homogeneous, smooth, and parallel layers, although this isn't necessarily the case. In the experimental results presented in Chapter 4 a significantly varying air gap is observed. The variation is due to stress induced curvature of the top mirror and the angular misalignment of the (111) silicon based bottom mirror. The model presented here for an ideal structure can be modified to account for the variable air gap. The modification is presented in Chapter 4 and predicts consistent spectra in comparison to the experimentally measured spectra.

The theoretical approach to the spectral calculations is a general, but versatile technique. The generality provides an analytical model easily amenable to changes in the Fabry-Perot structure. The theory is firstly based upon the standard boundary value approach. The tangential components of the electromagnetic wave electric field **E** and magnetic field strength **H** are made continuous across each boundary of the multilayered structure (or equivalently the normal components of **D** and **B**). The equations of continuity are then related using matrices [11, 12]. Consequently, each layer is uniquely defined by what is commonly called the characteristic matrix. The product of the characteristic matrices for all the layers allows one to relate the incident fields to those reflected and transmitted. The addition of a new layers is easily accommodated by the insertion of the new layer's characteristic matrix into the matrix product.

The spectral analysis of the multilayered structure is correct for both dielectric and absorptive materials such as gold or nickel. This is accomplished by assuming in general, that the materials index of refraction is complex. However, the solution is correct only for the case of normal incidence. In the case of non normal incidence, the wave in the absorbing material is nonhomogeneous. That is, the optical wave has a propagation vector magnitude and absorption that are dependent on propagation angle [13]. Since the study in its entirety is at normal incidence, the analysis is confined to this region.

2.3.2 The Calculation of the Transmission and Reflectance Spectra Using the Matrix Method

In this section, the incident, transmitted, and reflected fields are related for a general multilayer film stack. The stack represents the cantilever Fabry-Perot. A cross-sectional diagram of the stack with relevant symbology is shown in Figure 2-10.

The multilayered stack consists of N layers identified with indices: 0 for the incidence medium which is usually air, 1 through N for the stack, and l for the last layer. The complex indices of these layers is denoted by n. The thickness of each layer is designated by h.

The tangential components of the electric and magnetic field strengths are equated at each interface starting on the left with the 0/1 interface and moving to the right and concluding with the N/l interface. Note that the direction of propagation for each wave is denoted by **K** with direction given by the curl of **E** into **H**. Equating tangential components of the electric fields at the interface

$$E_{0r} + E_{0i} = E_{1r} + E_{1i} \tag{2-41}$$

and magnetic fields:

$$H_{0r} - H_{0i} = H_{1r} - H_{1i} \tag{2-42}$$

Multilayered Structure With N Layers

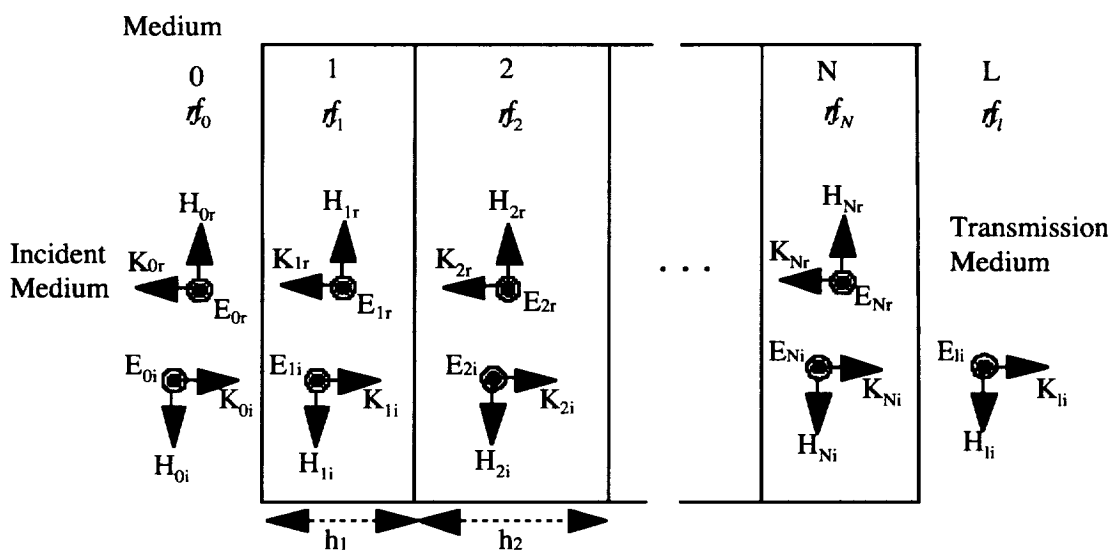

Figure 2-10. Diagram of the multilayered stack used in the spectral analysis.

The relation between **E** and **H** for a plane wave is given by

$$H = \frac{\tilde{n}_m}{\eta_o} E \tag{2-43}$$

$$\tilde{n}_m \rightarrow mth\,layer\,complex\,index$$
$$\eta_o \rightarrow free\,space\,wave\,impedence$$

Substituting into the **H** field continuity expression

$$\rightarrow E_{0r}\tilde{n}_0 - E_{0i}\tilde{n}_0 = E_{1r}\tilde{n}_1 - E_{1i}\tilde{n}_1 \tag{2-44}$$

These two equations describing the 0/1 interface can be rewritten in matrix form as

$$R_0 A_0 = L_1 A_1 \tag{2-45}$$

$$R_0 = \begin{pmatrix} 1 & 1 \\ \tilde{n}_0 & -\tilde{n}_0 \end{pmatrix}, A_0 = \begin{pmatrix} E_{0r} \\ E_{0i} \end{pmatrix}, L_1 = \begin{pmatrix} 1 & 1 \\ \tilde{n}_1 & -\tilde{n}_1 \end{pmatrix}, A_1 = \begin{pmatrix} E_{1r} \\ E_{1i} \end{pmatrix} \tag{2-46}$$

For the next boundary, 1/2 , the continuity equations become trickier since the relative phase shifts for the waves must be included.

$$E_{1r}e^{-j\beta_1} + E_{1i}e^{j\beta_1} = E_{2r} + E_{2i} \tag{2-47}$$

$$E_{1r}\tilde{n}_1 e^{-j\beta_1} - E_{1i}\tilde{n}_1 e^{j\beta_1} = E_{2r}\tilde{n}_2 - E_{2i}\tilde{n}_2 \tag{2-48}$$

The phase shift β is given by:

$$\beta_m = \frac{2\Pi}{\lambda} h_m \tilde{n}_m$$
$$\lambda \rightarrow free\,space\,wavelength$$
$$h_m \rightarrow mth\,layer\,thickness \tag{2-49}$$

Note that the forward moving wave in medium 1 is advanced in phase by β in propagating from the 0/1 to the 1/2 interface. Similarly, the backward traveling wave in medium 1 is retarded in phase by β in going from interface 0/1 to 1/2. The matrix relation for the 1/2 interface is given by

$$R_1 A_1 = L_2 A_2 \tag{2-50}$$

$$R_1 = \begin{pmatrix} e^{-j\beta_1} & e^{j\beta_1} \\ \tilde{n}_0 e^{-j\beta_1} & -\tilde{n}_0 e^{j\beta_1} \end{pmatrix}, A_1 = \begin{pmatrix} E_{1r} \\ E_{1i} \end{pmatrix}, L_2 = \begin{pmatrix} 1 & 1 \\ \tilde{n}_2 & -\tilde{n}_2 \end{pmatrix}, A_2 = \begin{pmatrix} E_{2r} \\ E_{2i} \end{pmatrix} \tag{2-51}$$

Similar matrix relations can be generated for each layer in the stack. For the last layer of the stack denoted by l.

$$R_N A_N = L_l A_l \tag{2-52}$$

$$R_N = \begin{pmatrix} e^{-j\beta_N} & e^{j\beta_N} \\ \tilde{n}_N e^{-j\beta_N} & -\tilde{n}_N e^{j\beta_N} \end{pmatrix}, A_N = \begin{pmatrix} E_{Nr} \\ E_{Ni} \end{pmatrix}, L_l = \begin{pmatrix} 1 & 1 \\ \tilde{n}_l & -\tilde{n}_l \end{pmatrix}, A_l = \begin{pmatrix} E_{lr} \\ E_{li} \end{pmatrix} \tag{2-53}$$

For the complete stack we can write using the inverse matrix operation

$$R_0 A_0 = \left[L_1 R_1^{-1} L_2 R_2^{-1} \bullet \bullet \bullet L_N R_N^{-1} \right] L_l R_l \tag{2-54}$$

Note that the matrix product in the brackets is a product of characteristic matrices for each layer. The product can be rewritten as

$$R_0 A_0 = \left[M_1 M_2 \bullet \bullet \bullet M_N \right] L_l A_l \tag{2-55}$$

$$M_m = L_m R_m^{-1} \tag{2-56}$$

Here M_m is the characteristic matrix of each layer. The matrix product of the layers shown in brackets is multiplied and represented by M_T the characteristic matrix of the total stack.

$$M_T = \begin{pmatrix} m_{11} & m_{12} \\ m_{21} & m_{22} \end{pmatrix} \tag{2-57}$$

$$R_0 A_0 = M_T L_l A_l \tag{2-58}$$

After the elements of the matrix have been calculated with a computer program, they can be used to calculate the field transmittance and reflectance using the easily derived equations below [11].

$$r = \frac{E_{or}}{E_{oi}} = \frac{\tilde{n}_0 \left(m_{11} - m_{12}\tilde{n}_l \right) - \left(m_{22}\tilde{n}_l - m_{21} \right)}{\tilde{n}_0 \left(m_{11} - m_{12}\tilde{n}_l \right) + \left(m_{22}\tilde{n}_l - m_{21} \right)} \tag{2-59}$$

$$t = \frac{E_{li}}{E_{oi}} = \frac{2\tilde{n}_0}{\tilde{n}_0 \left(m_{11} - m_{12}\tilde{n}_l \right) + \left(m_{22}\tilde{n}_l - m_{21} \right)} \tag{2-60}$$

The power reflectance and transmittance are given by

$$R = |r|^2 \tag{2-61}$$

$$T = \frac{n_l}{n_0} |t|^2 \tag{2-62}$$

The factor n_1/n_O in the power transmittance expression is a consequence of wave impedance differences between the incident and the transmitted medium.

2.4 Numerical Predictions For The Tunable Optical Filter: Electro-mechanical and Optical Theory Combined

Combining the electro-mechanical theory of section 2.2 with the optical theory presented in section 2.3 provides the means to predict the tuning characteristics of the micro-mechanical Fabry-Perot filter. That is, the voltage applied to the cantilever can be related to the transmitted and reflected spectra. In this section, numerical results generated by the theory are presented. The numerical results provide an understanding of how the tuning behavior is affected by the geometry of the structure and what the tradeoff issues are.

The material parameters used in the bending theory calculations were shown in Table 2-1 of section 2.2.2. Table 2-2 below lists the refractive indices used in the spectral calculations. The refractive indices of both gold and nickel contain a complex part which is representative of absorption. To model refractive index dispersion effects for the nickel and gold, a straight line fit was used between the specified values of refractive index. For the dielectric material silicon dioxide and the semiconductor silicon the Sellmeier dispersion formula was used [14]. The dispersion of metals (the gold and nickel) cannot be represented by the Sellmeier equation due to the loss of accuracy of the model near absorption bands. The Sellmeier formula is given by

$$n^2(\lambda) - 1 = \sum_{i=1} \frac{A_i \lambda^2}{\lambda^2 - \lambda_i^2} \tag{2-63}$$

The first three values of A_i and λ_I were used in the Sellmeier expansion and are listed in Table 2-2 for silicon dioxide and silicon.

Table 2-2. Optical Constants Used in the Theoretical Analysis.

Parameter	Symbol	Value	References
Gold Refractive Index	n_{Au}	0.13 + 3.48I (700 nm) 0.15 + 4.65I (800 nm) 0.17 + 5.34I (900nm) 0.18 + 6.04I (1000 nm)	[4]
Nickel Refractive Index		2.48 + 4.38I (800 nm) 2.85 + 5.10I (1000 nm)	[4]
SiO_2 Refractive Index	n_{SiO2}	Sellmeter Parameters: λ_1 = 0.0684043 λ_2 = 0.1162414 λ_1 = 9.896161 A_1 = 0.6961663 A_2 = 0.4079426 A_3 = 0.8974794	[4]
Si Refractive Index		Sellmeter Parameters: λ_1 = 0.301516485 λ_2 = 1.13475115 λ_3 = 1104.0 A_1 = 10.6684293 A_2 = 0.0030437484 A_3 = 1.54133408	[4]

Figures 2-11A and 2-11B show the predicted spectra for a 1 μm air gap Fabry-Perot in transmission and reflection.

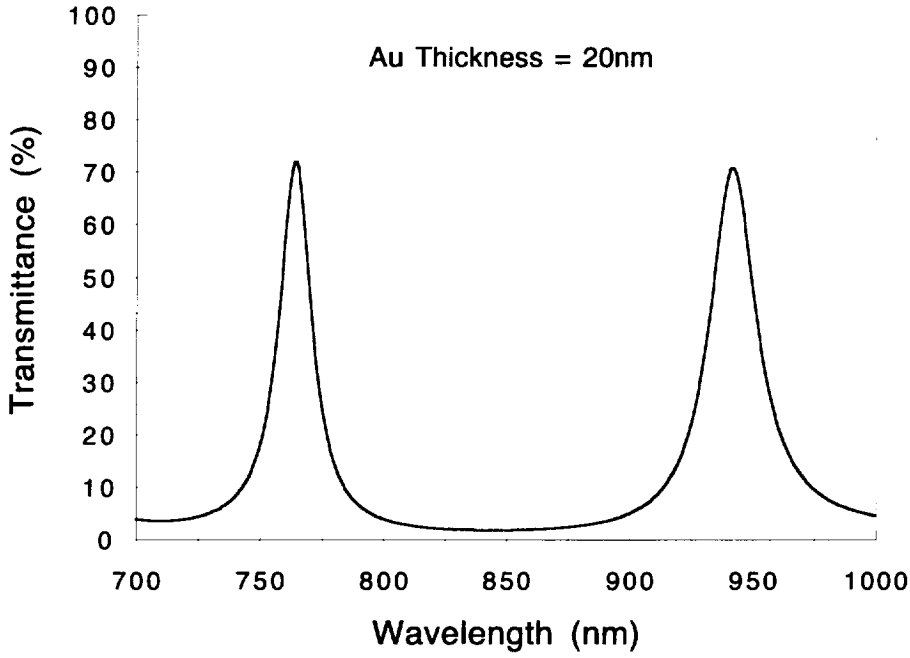

Figure 2-11A. Transmission spectra for a 1 μm air gap Fabry-Perot at zero bias. The gold thickness is 20 nm. The finesse of the Fabry-Perot is 8.0.

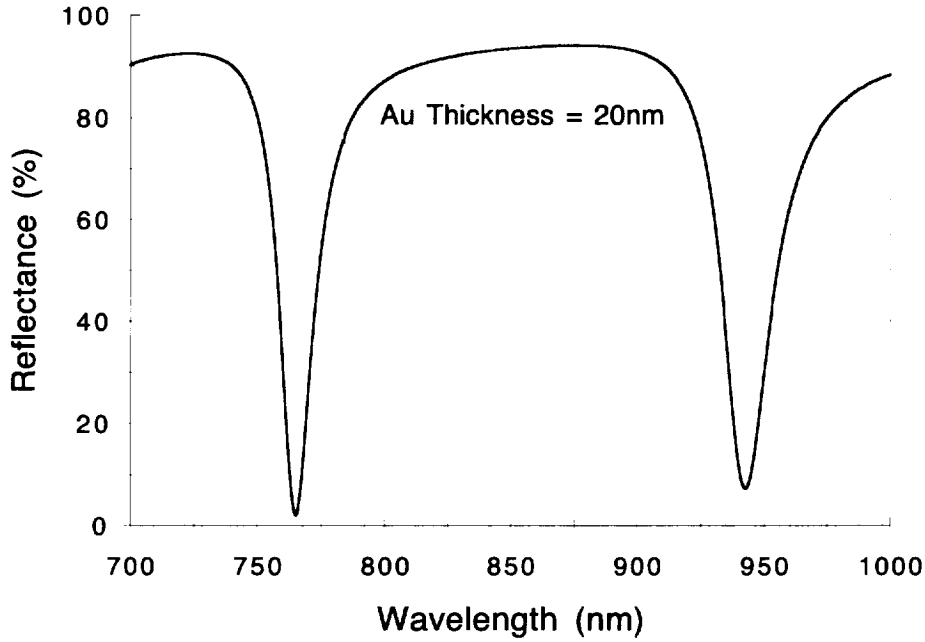

Figure 2-11B. Reflection spectra for a 1 μm air gap Fabry-Perot at zero bias. The gold thickness is 20 nm. The finesse of the Fabry-Perot is 8.0.

The spectra were calculated at zero bias. The cantilever oxide thickness was 0.85 μm and it is for all spectral data presented. The wavelength range of interest is 700-1000 nm which is the high responsivity region of a Si photodetector. In the introduction the potential for integrating a Si photodetector under the bottom mirror was mentioned. Referring to Figure 2-10A, the mode spacing of this structure is 181 nm in this wavelength range with transmission peaks at 765 nm and 946 nm. The peak transmission is 72% and 71% for the 765 nm and 946 nm peaks respectively. The transmission is down from the ideal 100% due to absorption in the gold mirrors. The Full Width at Half Maximum (FWHM) or linewidth of the transmission peaks is 24 nm. The calculated finesse at 850 nm is 8.0 which is approximately the number of Wavelength Division Multiplexing (WDM) channels that the filter could potentially select. Finesse is defined as

$$Finesse = \frac{FSR(\upsilon)}{FWHM(\upsilon)} \tag{2-64}$$

FSR is the free spectral range or mode spacing in frequency and FWHM is the full width at half maximum of the transmission peak in frequency. Figure 2-10B shows the reflectance spectra for the structure. The reflectance curve is basically the compliment of the transmission spectra less the absorption in the gold. The FWHMs of the reflection minima are approximately equal to those of the transmission peaks and was calculated to be 22 nm for the 946 nm peak.

The finesse of the Fabry-Perot can be improved by increasing the reflectance of the two gold mirror layers. This is done by increasing their thicknesses. The increase in reflectivity can be explained by considering the relative phase difference between the internal reflection at the oxide/gold interface and the reflection from the gold/air interface (the top mirror as an example). To first order, the total reflectance of the gold layer is the phasor sum from the two interfaces. The phase difference between these two reflections is approximately 180° indicating destructive interference between the waves and consequently a lower reflectance. By increasing the thickness of the layer the destructive interference between the waves is reduced since the wave traveling through the gold is absorbed more. Consequently, the reflectance goes up as thickness is increased and eventually will equal the reflectance of the gold/oxide interface.

Figure 2-12 shows the transmission spectrum for the same Fabry-Perot as in Figures 2-11A and B except that the gold layer thickness has been increased from 20 nm to 40 nm. As shown, the linewidth has been reduced to 6 nm . The calculated finesse has been improved to 30 at 850 nm. However, there has been a tradeoff between finesse and the transmittance, more power has been absorbed. The peak transmission has been reduced to 38% and 35% at the 765 nm and 946 nm peaks respectively.

Figure 2-13 shows a graph of transmittance and finesse as a function of gold thickness for the 1 μm air gap Fabry-Perot. A bias of 4 V has been applied to shift the transmission mode to 850 nm. The inverse relationship between finesse and transmittance is indicated.

The tuning characteristics of the 1 μm air gap cantilever are shown in Figure 2-14. The gold layer thickness is 40 nm providing a reasonable 5.5 to 6.5 nm linewidth. Transmission spectra are shown for the air gap ranging from 1 μm at zero bias to 0.75 μm at 4.3 V bias . Here the peaks blue shift with voltage as expected due to the cavity length reduction (the shift is indicated by the arrows). The voltage required to obtain the spectrum is labeled above the transmission peak.

Figure 2-15 shows a plot of the transmission peak wavelength versus voltage. 175 nm (almost the entire free spectral range) of wavelength shift is provided with 4.75 V of applied bias. The characteristic is quadratic in voltage. This agrees with the theory since the air gap at the tip of the cantilever is proportional to the square of the voltage (in the low voltage approximation) and the transmission wavelength is linearly proportional to the air gap. In the simple theory, the cavity OPL (Optical Path Length) is equal to an integer multiple of half wavelengths for the resonant transmission wavelength.

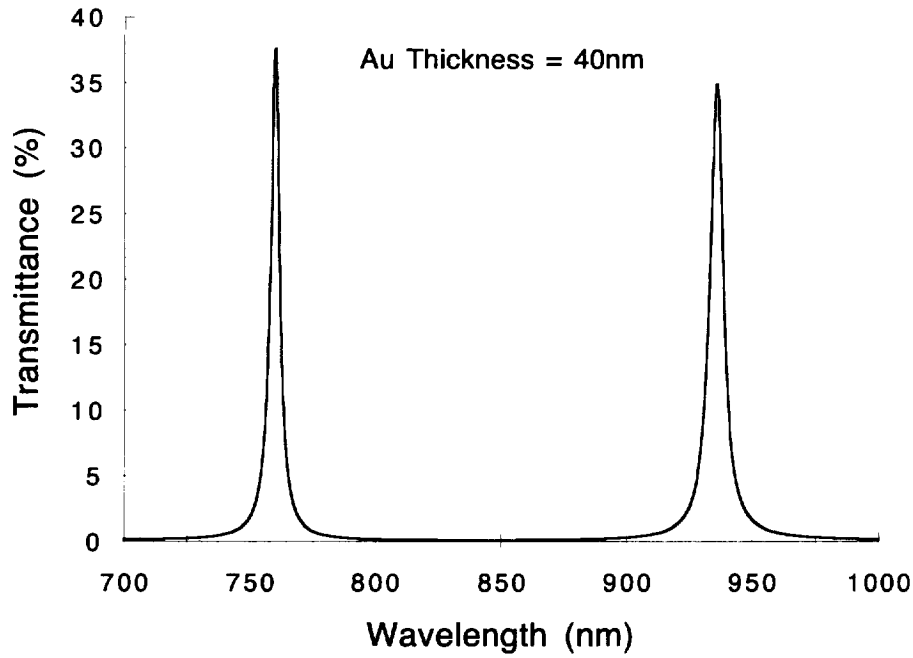

Figure 2-12. Transmission spectra for a 1 μm air gap Fabry-Perot at zero bias. The gold thickness has been increased from 20 nm to 50 nm providing a finesse increase from 8 to 30.

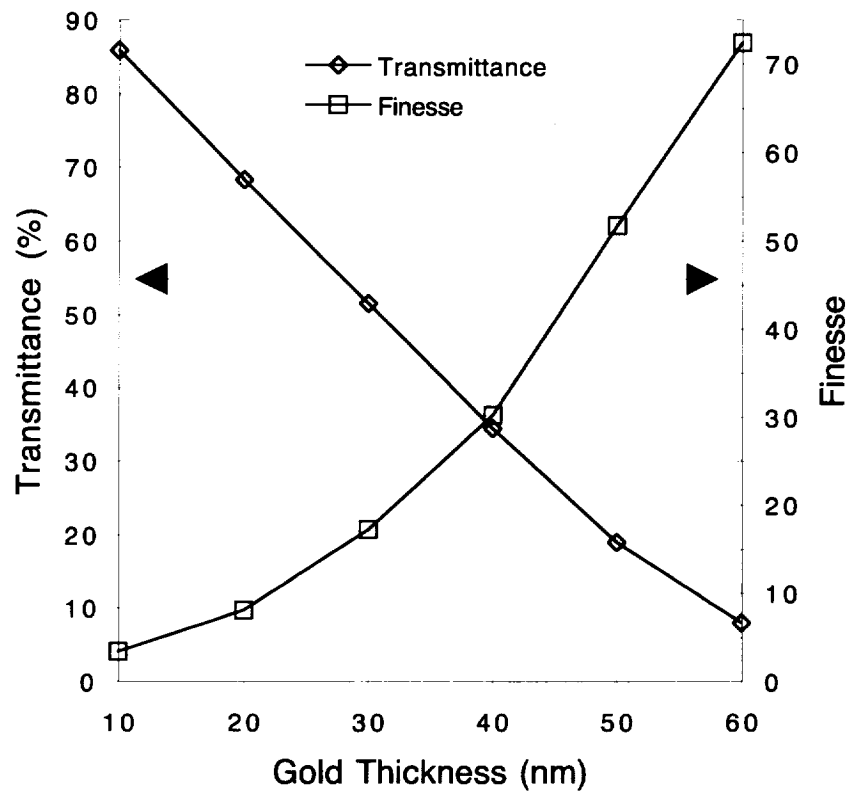

Figure 2-13. Transmittance and finesse as a function of gold thickness. Power throughput and finesse are traded off.

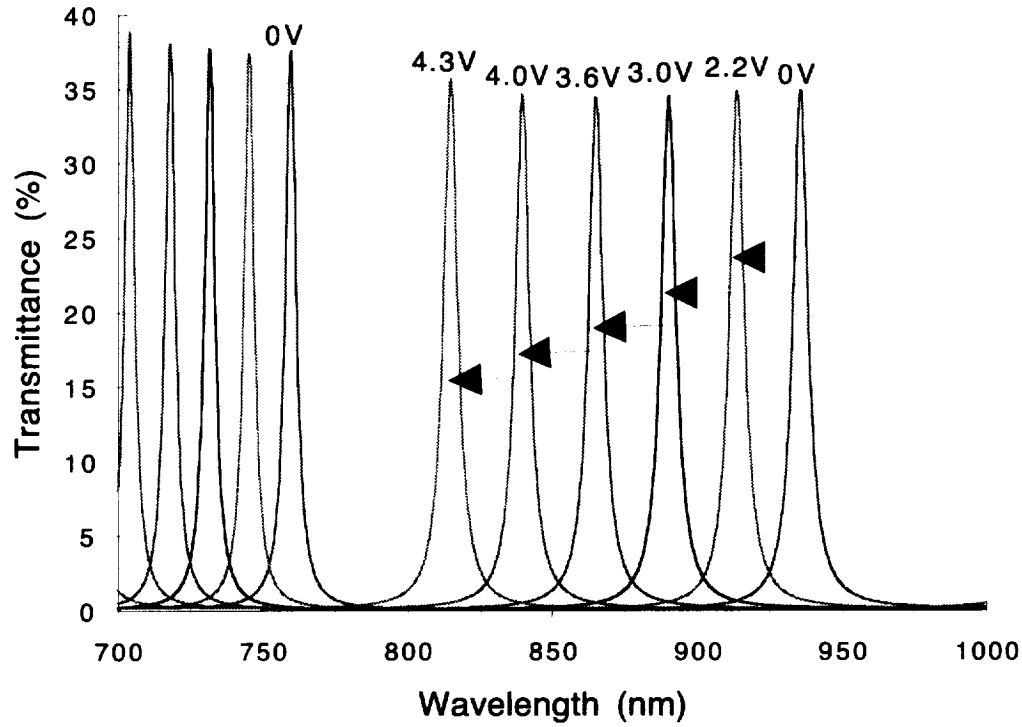

Figure 2-14. The spectral transmittance of the Fabry-Perot as a function of tuning voltage. The 0 volt bias air gap is 1 μm and the gold mirror thickness is 40 nm.

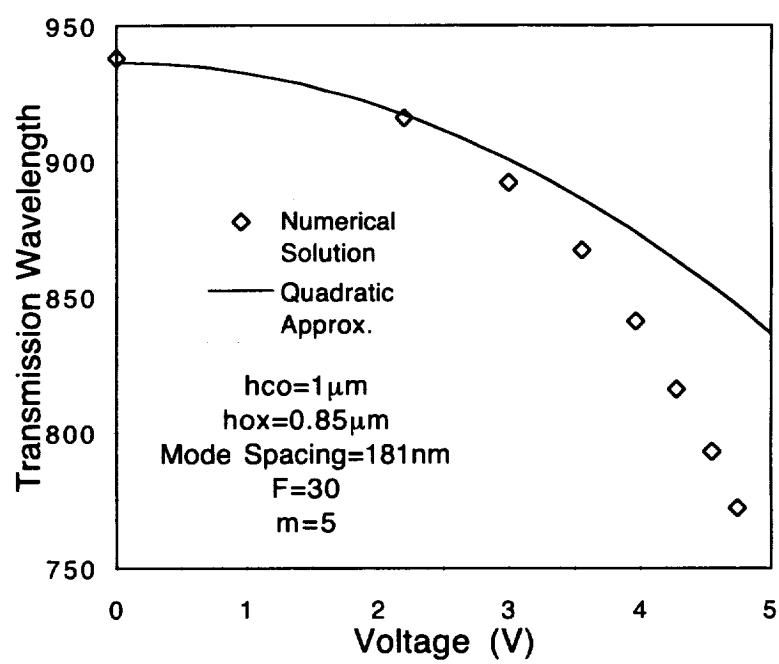

Figure 2-15. Transmission peak wavelength versus tuning voltage for the 1 μm air gap cantilever.

$$
\begin{aligned}
&OPL = m\frac{\lambda}{2} = n_{SiO_2}h_{ox} + h_c \\
&m \rightarrow positive\ integer \\
&n_{SiO_2} \rightarrow oxide\ refractive\ index \\
&h_{ox} \rightarrow oxide\ thickness \\
&h_c \rightarrow air\ gap
\end{aligned}
\tag{2-65}
$$

Using this relation in conjunction with the quadratic approximation in section 2.2.1 results in

$$
\lambda(V) = \frac{2}{m}\left\{ n_{SiO_2}h_{ox} + h_{co} - \frac{3}{4}\frac{\varepsilon_o}{Eh_{ox}^3}\frac{V^2}{\left[h_{co} + \frac{h_{ox}}{\varepsilon_{rox}}\right]^2}L^4 \right\}
\tag{2-66}
$$

This approximation was plotted along with the numerical solution. The approximation predicts the characteristic closely up to 3 V. Beyond 3 V the analytic approximation underestimates the wavelength shift. The reduced accuracy beyond 3 V is due to the inaccuracy of the quadratic approximation of the cantilever bending at high values of the voltage to air gap ratio.

Figures 2-16 shows the transmission spectra for a 4 μm air gap cantilever with zero bias. The mode spacing is a much smaller 73 nm in comparison to the 181 nm of the 1 μm air gap Fabry-Perot. This is predicted by the simple theory

$$
\text{frequency mode spacing:}\quad \Delta f = \frac{c}{2OPL}
\tag{2-67}
$$

$$
\text{Wavelength Mode Spacing:}\quad \Delta\lambda = \frac{\bar{\lambda}^2\Delta f}{c} \approx \frac{\bar{\lambda}^2}{2OPL}
\tag{2-68}
$$

However, consistent with a constant finesse (the finesse depends only on the mirror reflectances), the linewidth of the 4 μm cavity is smaller by the factor 73/181. In agreement the linewidth is 2.3 nm at the 887 nm peak.

The smaller linewidth of the 4 μm structure could be more advantageous over the shorter 1 μm Fabry-Perot in applications where the spectral lines of the source are closely spaced and a large free spectral range is not required.

Figure 2-17 shows the spectra for the 4 μm cavity for voltages ranging from 0 to 16.6 V. The transmission spectra linewidths range from 1.8 to 2.3 nm.

Figure 2-18 shows the transmission peak wavelength as a function of tuning voltage. The same quadratic behavior is observed as with the 1 μm air gap cavity. However, the wavelength shift sensitivity to voltage in much reduced. A wavelength shift of 71 nm is obtained with 20.5 V whereas the 1 μm cavity provided 166 nm of tuning with only 4.7 V. The quadratic approximation more accurately predicts the tuning behavior of the 4 μm air gap cantilever due its small voltage to air gap ratio in comparison to the 1 μm structure .

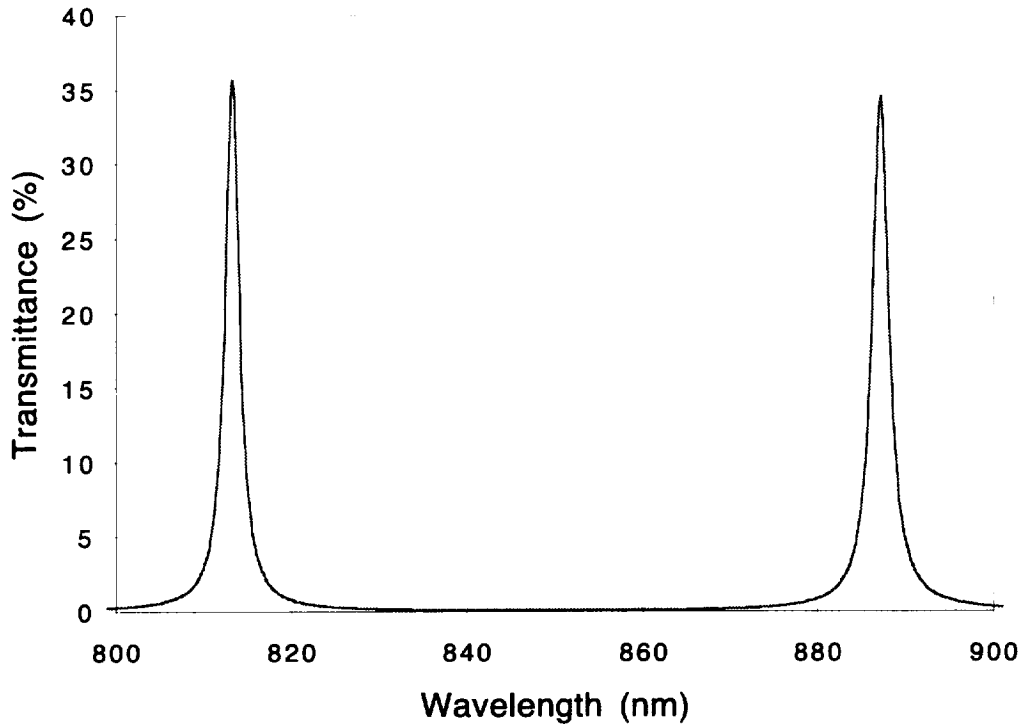

Figure 2-16. Transmission spectrum for a 4 μm air gap Fabry-Perot at zero bias.

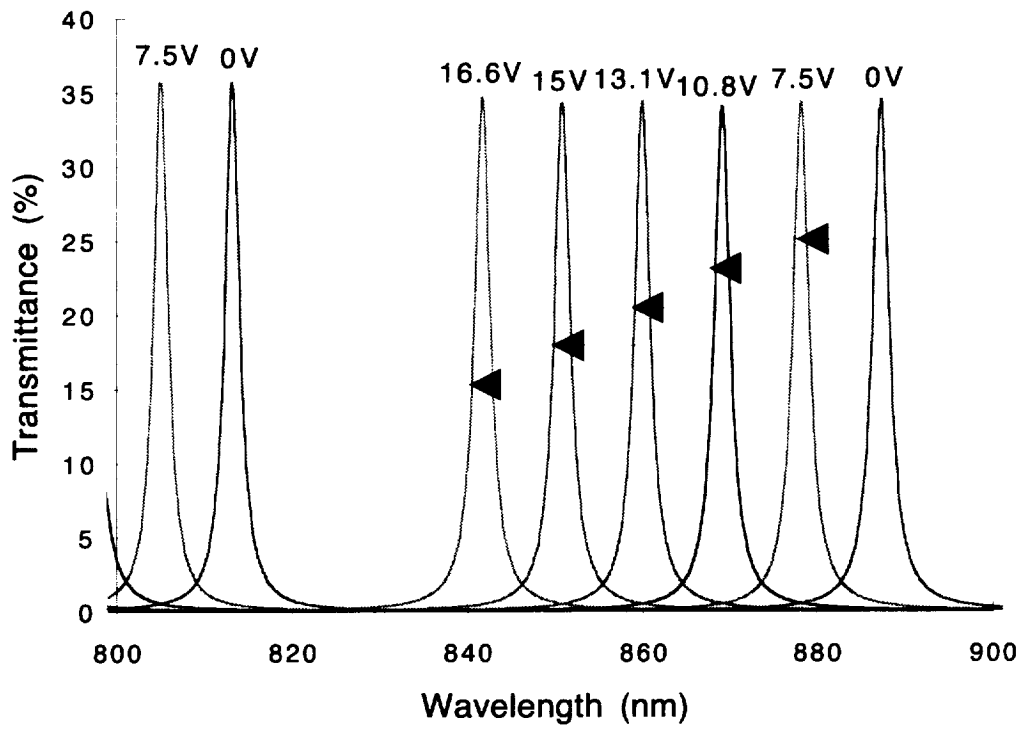

Figure 2-17. The spectral transmittance of the Fabry-Perot as a function of tuning voltage. The 0 Volt bias air gap is 4 μm and the gold mirror thickness is 40 nm.

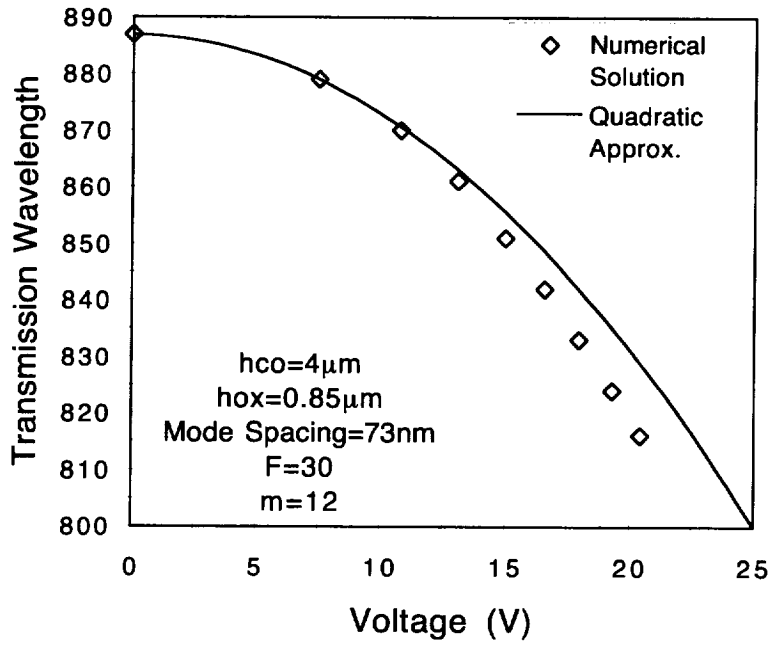

Figure 2-18. Transmission peak wavelength versus tuning voltage for the 4 μm air gap cantilever.

2.5 References

1. Archer, R. R., et al., *An Introduction to the Mechanics of Solids*, 2nd ed., T. J. Lardner, editor, McGraw-Hill, New York, pp. 511–555, 1982.

2. Zeghbroeck, B. J. V., *Micro-Mechanics*, in *Principles of Electronic Devices*, University of Colorado: Boulder, pp. A1.1–A1.4, 1995.

3. Stokey, W. F., *Vibrations of Systems Having Distributed Mass and Elasticity*, in *Shock and Vibration Handbook*, C. M. Harris, Editor., McGraw-Hill, New York, pp. 7-1 to 7-15, 1988.

4. Waynant, R. and M. Ediger, *Electro-Optics Handbook*, 1st ed., McGraw-Hill, New York, pp. 11.56–11.75, 1994.

5. Sze, S. M., *Physics of Semiconductor Devices*, John Wiley & Sons, New York, 1969.

6. Finite Element Structural Modeling Software, Version 67, *MSC/NASTRAN*, MacNeil Schwendler Corporation, Los Angeles, CA, 1993.

7. Petersen, K. E., *Silicon as a Mechanical Material*, Proceedings of the IEEE, **70**(5), p. 420, 1982.

8. Nathanson, H. C. and R. A. Wickstrom, A Resonant-Gate Silicon Surface Transistor With High-Q Bandpass Properties. *App. Phys. Ltrs.*, **7**, p. 84, 1965.

9. Nathanson, H. C., et al., The Resonant Gate Transistor, *IEEE Trans. Elect. Dev.*, **ED-14**: p. 117, 1967.

10. Petersen, K. E., *Dynamic Micromechanics on Silicon: Techniques and Devices*. IEEE Trans. Electron Devices, **ED-25**, p. 1241, 1978.

11. Born, M. and E. Wolf, *Wave Propagation In A Stratified Medium. Theory of Dielectric Films*, in *Principles of Optics*, Pergamon Press, New York, pp. 51–70, 1980.

12. Fowles, G. R., *Theory of Multilayer Films*, in *Introduction to Modern Optics*, Holt, Rinehart and Winston, Inc., New York, pp. 95–100, 1968.

13. Fowles, G. R., *Reflection and Refraction at the Boundary of an Absorbing Medium*, in *Introduction to Modern Optics*, Holt, Rinehart, and Winston Inc., New York, pp. 165–168, 1968.

14. Jenkins, F. A. and H. E. White, *Dispersion*, in *Fundamentals of Optics*, McGraw-Hill, New York, pp. 464–487, 1957.

III. Fabrication of the Micro-Mechanical Fabry-Perot Filters

3.0 Introduction.

In this chapter we present an overview of the standard methods used to fabricate micro-mechanical Fabry-Perots. This is followed by a section discussing silicon micro-machining using anisotropic wet KOH etching and Reactive Ion Etching (RIE). A combination of vertical RIE and wet KOH etching is shown to provide lateral etching in (111) silicon which can be used to undercut a silicon dioxide or silicon nitride masking material. In section 3.3 we introduce a new fabrication process to form air gap micro-mechanical Fabry-Perots that is based on this etching technique. Fabry-Perots formed with this technique are the focus of the study. Finally in section 3.4 we describe the entire fabrication process in detail. The process presented is self-aligned and uses only one mask level to provide the mirrors and the electrical isolation. Fabrication results, problems, and potential solutions are also presented.

3.1 Popular Methods of Micro-Mechanical Fabry-Perot Fabrication Using Deposited Materials

The fabrication methods for micro-mechanical Fabry-Perots recently reported in the literature rely on deposited materials for the mirrors and the air gap formation. In general, these methods require the formation of a sandwich of mirror material surrounding a sacrificial layer that can be removed selectively producing an air gap Fabry-Perot. This is accomplished by depositing the bottom mirror material on the substrate, followed by a sacrificial layer, and then the top mirror. These layers are typically deposited by Chemical Vapor Deposition (CVD) or Molecular Beam Epitaxy (MBE) processes. Via holes for a wet chemical or plasma etchant are provided through the top mirror region to facilitate the removal of the sacrificial layer. Removal of the sacrificial layer can be accomplished by both wet chemical and plasma etchants provided that the etchant has a high selectivity to the sacrificial layer over the mirror materials.

Polyimide and photoresist have been used successfully as a sacrificial layer when using Si and SiO_2 DBR mirrors [1]. The polyimide or photoresist are easily removed with an oxygen plasma without attacking Si or SiO_2. Acetone can be used to remove the positive photoresist also. Researchers fabricating GaAs based Fabry-Perots have used intrinsic GaAs as a sacrificial layer with AlGaAs mirrors. Selective removal of the GaAs sacrificial layer has been accomplished with a dry etch using a $SiCl_4$ and SF_6 plasma [2].

3.2 Anisotropic Etching of Silicon in KOH

Another method of sacrificial layer removal is to take advantage of the anisotropic etching behavior of a crystalline material in a wet chemical. This process is simpler, since the sacrificial layer need not be deposited. Instead the substrate material provides the sacrificial layer. In this section we present an overview of anisotropic etching of Si in KOH and an associated method by which thin film membranes can be undercut. The method is amenable to the fabrication of micro-mechanical Fabry-Perot structures.

The anisotropic etching behavior of crystalline silicon in wet chemical etchants has been known for many years [3–6]. This anisotropy makes possible many unique etched geometries. Integrated circuit designs have implemented anisotropic etching to form trench electrical isolation around transistors. In the area of micro-machining, pyramid shaped ink jet nozzles have been formed using the anisotropic etching behavior. The anisotropic etching behavior is a consequence of a high etch rate dependency on direction in the silicon crystal. This dependence has been attributed to differences in atomic and dangling bond densities for different planes in the crystalline lattice [3]. In the silicon lattice, the principle feature of the anisotropic etching behavior is the much slower etch rate of the (111) planes in comparison to the much faster etching (110) and (100) planes. The (111) planes have the highest density of atoms per square centimeter and the lowest density of dangling bonds that can be easily attacked by the etchant molecules.

A common anisotropic silicon etchant is KOH. Its silicon etching behavior has been well studied

[3, 7]. Its etching behavior is not highly sensitive to the Si dopant type (p or n type) or dopant density provided that the density is not greater than $10^{20}/cm^3$. KOH provides comparative etch rates and selectivities given by :

$$\text{Comparative Etch Rates in KOH: } (110) > (100) >> (111) >>> SiO_2 >> Si_3N_4 \tag{3-1}$$

$$\text{Selectivities: } \frac{(110)}{(111)} = 160 \quad \frac{(110)}{SiO_2} = 500 \quad \frac{(110)}{Si_3N_4} = \infty \tag{3-2}$$

The selectivities where taken from the literature [7] and are shown for a solution of 45% KOH in water by weight at a temperature of 70°C. KOH etches (110) planes most rapidly while the (111) planes comparably form an etch stop. The etch rates and selectivities of two optically transparent dielectric materials, SiO_2 and Si_3N_4 have also been included. These are the popular and effective KOH masking materials. They provide an additional etch geometry control mechanism and can also be used for their good mechanical properties. Here Si_3N_4 provides the best etch stop for KOH. However, SiO_2 can be used for shorter etch time applications.

There are three standard silicon wafer orientations (surface normal) which yield unique anisotropic etching geometries. These are the most popular (100) orientation, the (110), and the least popular (111) orientation. Pyramidal shaped structures can be formed in (100) Si by opening square holes in the masking material to the KOH etching. Figure 3-1 shows a cross-sectional view of the pyramid structure in a (100) substrate. Here the Si etches quickly in the vertical [100] direction until the slow etching (111) facets are exposed resulting the 54.7° angles as shown in the Figure. Some undercutting of the mask material has occurred due to the angle of the (111) facets and the small width of the window. The other two walls of the four sided pyramid are found by a rotation of the Figure by 90°. This technique has been used to form ink jet nozzles and trench isolation.

Rectangular trenches can be formed in (110) Si substrates as shown in Figure 3-2. Here the Si etches vertically in the fastest etching [110] direction. Lateral etching or undercutting is prevented by the (111) sidewalls. The depth of these trenches are not constrained by (111) facets permitting them to be deep and narrow.

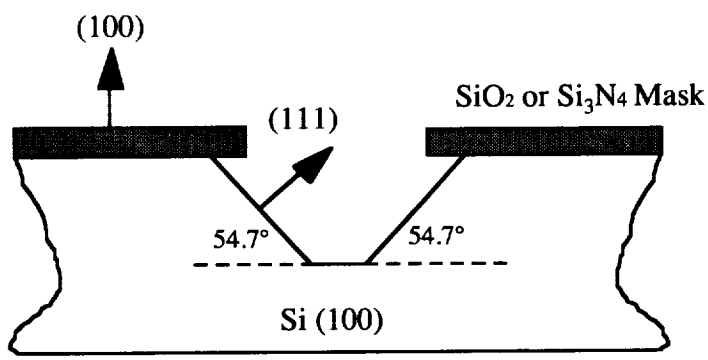

Figure 3-1. Pyramidal structure formed in (100) Si by KOH etching.

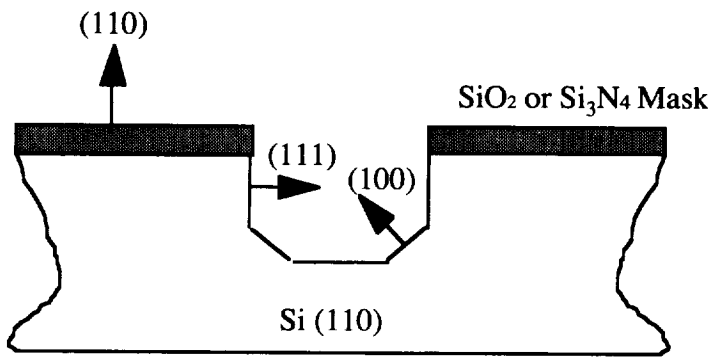

Figure 3-2. Rectangular trenches formed in (110) Si by KOH etching.

Now imagine rotating the (110) wafer by 90 degrees resulting in a (111) surface normal and a (110) facet facing laterally. The anisotropic etching of the (111) Si is not possible by KOH etching alone, since the only facet exposed through the mask would be the slowly etching (111) plane. However, RIE (Reactive Ion Etching) is not as sensitive to the crystal direction and can be used to drill vertically through the (111) surface exposing the faster etching (110) planes. A schematic of the (111) oriented Si is shown in Figure 3-3 following vertical drilling with two windows opened in the mask.

Following the RIE, the wafer can be etched in KOH. The etching is shown in Figure 3-4. The exposed (110) facets are rapidly etched resulting in the undercutting of the mask material. If the etching is continued, the mask material between the two windows will be completely undercut. The depth of the well remains relatively constant due to its slowly etching (111) surface. This assumes that the etch rate in the [111] direction is small and that the etch time is low. However, prolonged etch times will result in increased depth. The Figure shows the (110) wall proceeding with the etch perpendicular to the (111) surface. For prolonged etch times the wall profile will evolve and eventually meet and stop on another (111) surface. This will only be true for the outside walls. Here it is assumed that the central masked region is narrow enough to prohibit this. The inside wall angles are 109.5° for the left wall and 70.5° for the right wall.

The lateral undercutting of the mask material is exactly what is needed to provide a freely suspended structure which can be used to realize a micro-mechanical Fabry-Perot. This technique has several important advantages for Fabry-Perot formation. The depth of the well can be controlled by the RIE etch alone. Since the cavity length of the Fabry-Perot dictates its resonant wavelengths, single step depth control is advantageous. Additionally, the lateral undercutting along the [110] direction provides a flat surface underneath and parallel to the suspended mask material which can be used as the bottom mirror of the Fabry-Perot.

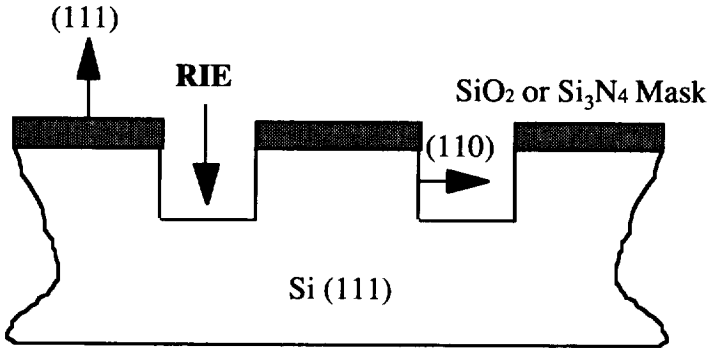

Figure 3-3. Schematic of (111) Si following vertical drilling using RIE.

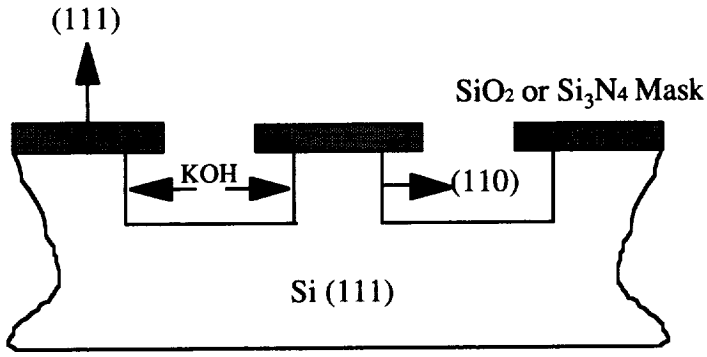

Figure 3-4. Cross-sectional diagram of (111) silicon drilled vertically with RIE and followed with lateral KOH etching.

Although (100) Si can be used to provide mask undercutting it suffers from several disadvantages [8]. The amount of undercutting is strongly dependent on window size constraining the geometry of the freely suspended structure. Additionally, the presence of a silicon ridge formed by (111) facets under the suspended structure results in nonplanar etched surface.

3.3 Fabrication of the Fabry-Perots in (111) Silicon: an Overview

In the previous section we presented a method by which thin film membranes could be formed in (111) Si using a combination of RIE and KOH etching. The method provides depth control by RIE etching alone. The resulting membranes are inherently parallel to the surface of the undercut Si providing for a structure amenable for use as a micro-mechanical Fabry-Perot filter. In this study we use this process to form micro-mechanical Fabry-Perot structures.

Two optically transparent dielectric materials, SiO_2 and Si_3N_4 were mentioned as suitable mask materials for KOH etching. There are tradeoffs to be considered between Si_3N_4 and SiO_2. Si_3N_4 is a better mask material for KOH. From a mechanical point of view it has an elasticity modulus (3.85×10^{12} dyne/cm^2) 5 times that of SiO_2 (0.73×10^{12} dyne/cm^2). This implies that much thinner silicon nitride layers can achieve the same stiffness as silicon dioxide layers. A disadvantage of Si_3N_4 is its high index of refraction (2.05) in comparison to SiO_2 (1.46). The higher index will result in a lower finesse due to the deleterious larger reflection at the dielectric-air interface at the underside of the cantilever: 11% reflectivity for silicon nitride versus 4% for silicon dioxide. Maximizing the majority of the reflection to occur at the metal-dielectric interface provides best reflectivities. SiO_2 layers can be thermally grown whereas Si_3N_4 layers must be deposited. High temperature growth provides superior films in comparison to those which are deposited. Deposited films are generally, not as dense, of uniform thickness, and not as void free as thermally grown films. The thermal growth of SiO_2 is the simplest and one of the most standard thin film process. On the other hand, the high growth temperatures required for thermal oxidation (900–1100°C) and the large differences in thermal coefficient of expansion between SiO_2 (0.55×10^{-6}/°C) and Si (2.33×10^{-6}/°C) could potentially result in stress problems. The stress can manifest itself as curvature and even catastrophic breakage of the membranes following undercutting. Si_3N_4 is deposited generally at a temperature of 700°C (300°C with plasma assisted deposition) and has a coefficient of expansion ($2.85 \times {}^{-6}$/°C) much closer to that of Si and consequently would suffer less stress problems than SiO_2 [9]. In this study, we use thermally grown SiO_2 for the membrane and mask material due to its growth simplicity and lower refractive index. Although Si_3N_4 may be potentially a better material primarily due to its lower stress. Stress problems with the thermally grown SiO_2 will be presented in section 3-11.

Figure 3-5 shows a top view of the basic process for cantilever mirror formation. We start with a (111) oriented Si wafer. We then thermally grow an oxide layer. The thermal oxidation provides the mechanical

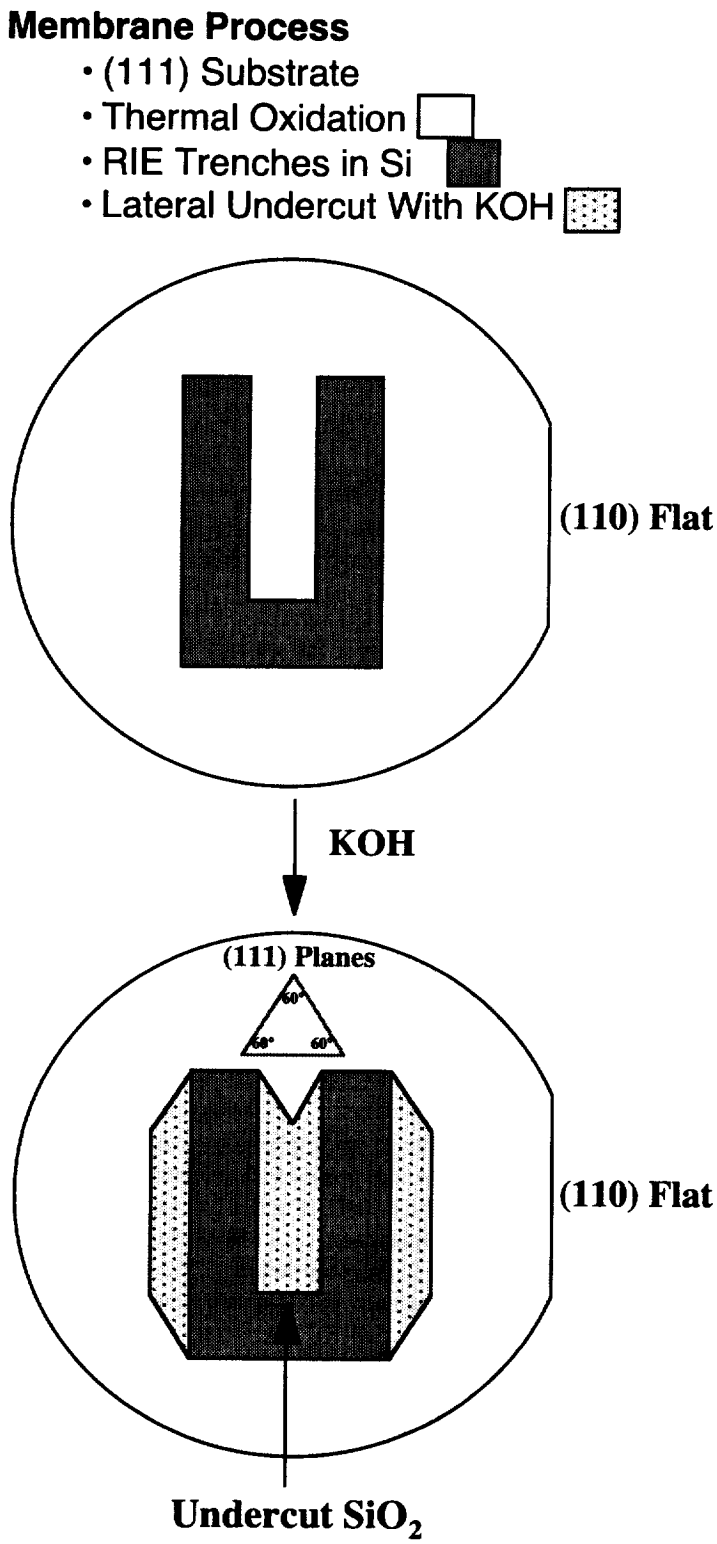

Figure 3-5. Basic movable mirror fabrication process.

material for the suspended movable mirrors (a cantilever structure). The oxidation is followed by the masking of a region defining the mirror which blocks the reactive ion etching. The (111) wafer is then placed in an RIE etcher where the exposed SiO_2 layer and Si are etched. The RIE etched region is shown in Figure 3-5 as the dark gray areas. The vertical etching exposes (110) facets which are parallel to the flat and perpendicular to the surface. Next the wafer is placed in liquid KOH. The KOH etches the silicon rapidly in the (110) direction undercutting the SiO_2 and providing a freely suspended cantilever. The dotted gray areas in the figure are those in which the oxide has been undercut.

Note that the long length of the cantilever is oriented parallel to the wafer flat or equivalently the (110) facet. This orientation is necessary to provide the fastest undercutting. On the other hand, a 90° rotation of the cantilever pattern would have resulted in no undercutting at all since the largest exposed facet would be another (111) plane besides the surface. The triangular inset shows the intersection of all 3 remaining (111) etch stop planes with the (111) surface. The intersections are 60° apart and are the source of the 60° facets in the corners of the etch silicon well and the remaining triangular wall of Si under the connecting section of the cantilever.

Finally, to produce a Fabry-Perot filter from the suspended cantilever structure, we metallize the cantilever and the silicon underneath. The metallization provides the high reflectivity mirrors. The top mirror metallization is carried out with simple evaporation while the bottom mirror or Si substrate is electroplated.

3.4 Fabrication of Fabry-Perot Filters in (111) Si: Details and Results

3.4.0 Process Objectives

The fabrication goal requires a fabrication process which has as few steps as possible which are easy to control and produces high yields. Good Fabry-Perot finesse requires a process that produces a high degree of mirror reflectivity, smoothness, flatness, and parallelism. To provide electrostatic force tunability, the Fabry-Perot mirrors must be sufficiently electrically isolated from one another. In light of these objectives, we present a single mask layer, self-aligned fabrication process for a tunable micro-mechanical Fabry-Perot filter.

3.4.1 Si Wafer Specifications

An important precursor to processing was to obtain (111) Si wafers with a surface normal as close as possible to the (111) direction. Standard off-the-shelf (111) wafers are typically 4° tilted from (111) to prevent channeling effects during normal incidence ion implantation. Any deviation from (111) orientation will result in Si surfaces with a rough staircase like profile following the KOH etch. This is a consequence of the flat RIE etched surface etching in KOH until it meets a collection of offset but parallel (111) surfaces. The surface profile of a 4° tilted, KOH etched, (111) Si wafer is shown in Figure 3-6. The pitch of the staircase is 5 to 10 μm with a 0.5 to 2 μm step height. The staircase profile of the silicon will result in a bottom mirror with a diffuse reflectance consequently lowering the finesse of the completed Fabry-Perot structure.

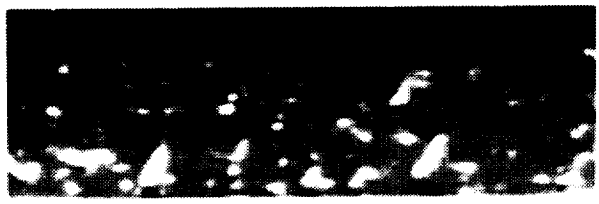

Figure 3-6. Staircase Si profile which results from 4° misalignment with the (111) direction.

To avoid the staircase effect, Si (111) wafers were ordered from Semiconductor Processing Co. of Boston MA, with tolerances of +/– 0.5° on the misalignment with the (111) direction. Tighter tolerances were not permitted due to their manufacturing capability. The wafers were also specified as 10 Ω-cm , p or n type, and were double side polished. The KOH etching is insensitive to dopant type and density allowing for integration flexibility.

3.4.2 Thermal Oxidation

A wet thermal oxidation at 1000°C was used to provide the KOH etching mask and supporting structure for the cantilever mirrors. The 1000°C temperature was chosen as the lowest reasonable temperature to grow a maximum of 9000 Å of oxide in one eight hour day. Low growth temperatures were desired in order to minimize the thermal stress between the oxide and the silicon. The higher thermal expansion coefficient of the Si results in compressive stress in the oxide and consequently can cause buckling of the oxide after undercutting [10]. The furnace temperature was monitored to ensure that a steady temperature had been reached before insertion of the wafers. The Si wafers were taken directly from the wafer box in their cleanest state and placed in the furnace. The wafers were inserted slowly with only N_2 purge gas flowing to prevent any thermal stress gradients forming due to oxide layers growing at different temperatures. Various oxide thicknesses (5000 to 9000Å) were grown to provide cantilever mirrors with a wide variety of mechanical properties for the study.

3.4.3 Masking Materials For the RIE Step

Following thermal oxidation, masking material for the vertical RIE step was put on the wafer as shown in Figure 3-7.

The gas used for the RIE was Poly etch which contains 90% CF_4 with 10% NO_2. Two mask materials were used, either spun on negative photoresist or evaporated chrome. A photoresist mask yields a smoother RIE etched Si surface in comparison to a Cr mask. The Cr mask suffers from edge profile cracking and flaking during the etching. The Cr flakes can redeposit in the etched region resulting in unwanted surface roughness. Photoresist, on the other hand, does not flake off. However negative photoresist has a comparably high etch rate in CF_4 in comparison to Cr and will eventually be etched away. Consequently, photoresist was used in the cases where shallow or short cavity Fabry-Perots were desired (<0.6 μm) and Cr in the case of deep wells >(0.6 μm).

3.4.4 The Photolithographic Mask Design

3.4.4.1 Mask Design Introduction. As mentioned earlier only one mask is required for the fabrication of the micro-mechanical Fabry-Perot filters. The mask used for the fabrication is shown in Figure 3-8.

It contains 57 uniquely shaped cantilever mirrors with various lengths and widths and with either one or two supporting legs. Each cantilever is surrounded by a hexagonal shaped trench that provides electrical isolation between Fabry-Perot structures. The mirror regions (where the light is focused) of the cantilevers were made either 50 μm or 20 μm wide in order to accommodate the spot sizes of multimode or single mode fiber.

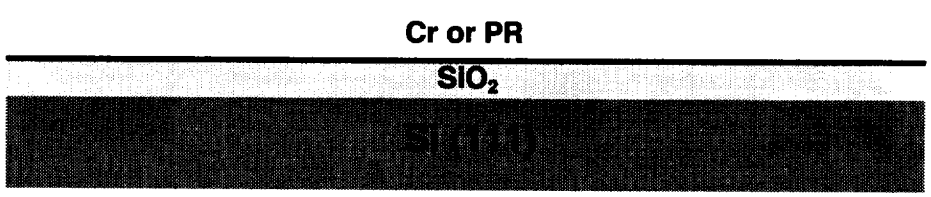

Figure 3-7. Cross-section of the wafer following oxide growth and masking for reactive ion etching.

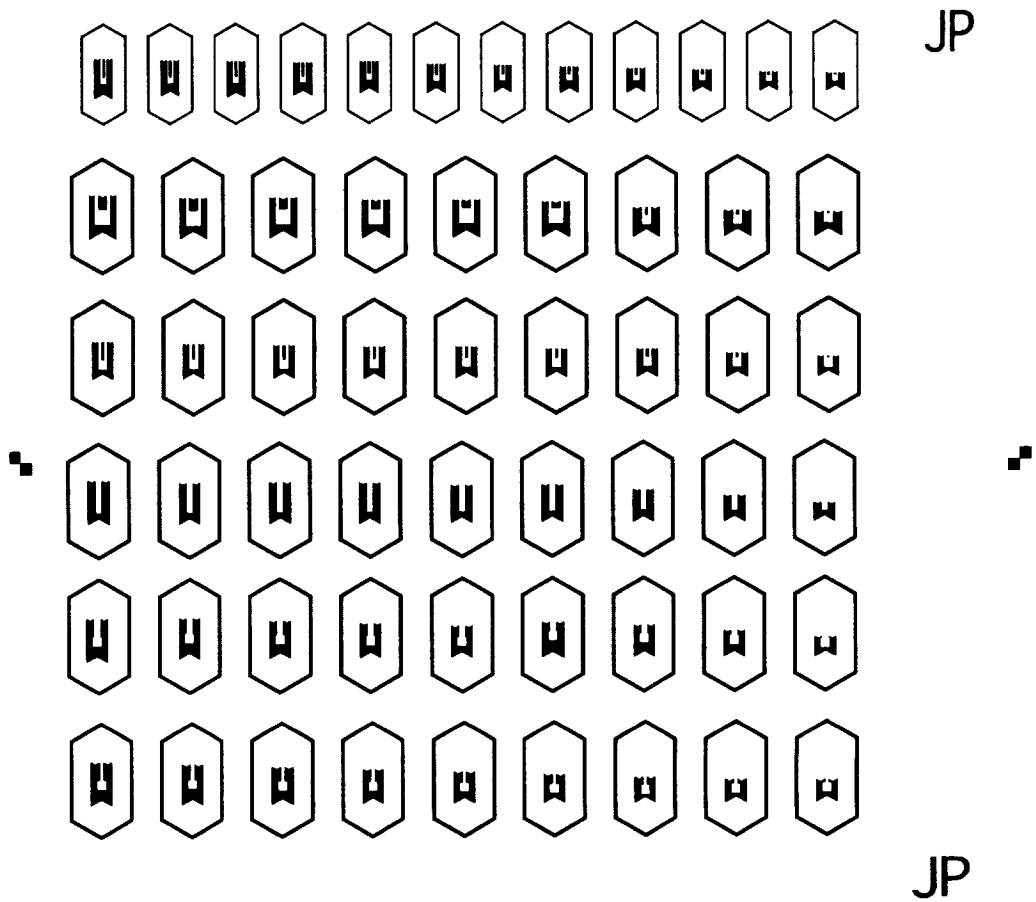

Figure 3-8. The single mask required for the fabrication of the micro-mechanical Fabry-Perot filters. The mask incorporates a wide variety of cantilever shapes each surrounded by a hexagonal electrical isolation trench.

3.4.4.2 Why Cantilever Mirrors? The choice of the cantilever structure for the top mirror instead of a structure held on two or more sides was a consequence of two issues. It is much easier to bend a cantilever than to stretch a structure held on two or more sides. Early experiments showed no movement with 50 V applied to a 5000 Å thick "H" shaped mirror that was held on two sides. As discussed in the theoretical section, the required voltages to shift the cantilever filter by 100 nm wavelength can be less than 5 V, making it compatible with standard transistor voltages. The second issue arises from, the mismatch between the thermal expansion coefficients of Si and SiO_2, and the high growth temperature of the thermal oxide. The SEM (Scanning Electron Microscope) photo of an "H" shaped membrane that is held on each side by two legs is shown in Figure 3-9.

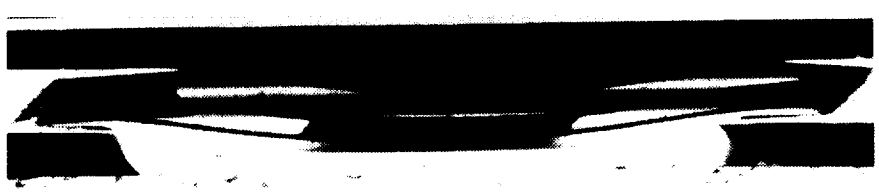

Figure 3-9. A SEM photograph of an "H" shaped oxide membrane on Si which is sagging due to compressive stress.

This cantilever is 150 μm long and exhibits a sag of 5.5 μm in a 7 μm deep Si well. The sag is a consequence of the much higher coefficient of thermal expansion of Si in comparison to SiO_2 and the high growth temperature of the SiO_2. The oxide was grown at 1000°C temperature, with $\alpha_{Si} = 2.6 \times 10^{-6}/°C$ and $\alpha_{SiO2} = 5 \times 10^{-7}/°C$. As the membrane structures cool to room temperature following removal from the furnace, the Si substrate contracts five times more than the SiO_2 placing it under compression. Following the removal of the Si underneath the membrane it relaxes through expansion and sags. The sag produces a central mirror area which is not optimally flat. Instead it is concave up which results in an unstable optical resonator. One solution to this problem is to use deposited low temperature oxide, silicon nitride, or silicon oxynitride for the membrane material. These films can be deposited on silicon with much lower stress.

Cantilevers, on the other hand, do not suffer from the sagging problem even with large thermal coefficient of expansion differences. Instead, as the silicon underneath the oxide cantilever is removed, it is allowed to freely expand at the free end without buckling. As a consequence of the bending ease and reduced thermal oxide buckling, the study focused on the cantilever mirror structure.

3.4.4.3 Mask Design For Electrical Isolation. The top mirrors or cantilevers must be electrically isolated from the bottom mirror to provide voltage tunability. A capacitive charging of the mirrors provides the electrostatic bending force on the cantilever. Furthermore, each of the Fabry-Perot cantilever mirrors on the die must be electrically isolated from one another to provide for independent voltage tuning.

One mask is used to provide for both the undercutting of the cantilevers and the electrical isolation. We provide the electrical isolation by using the same undercutting technique as used for the removal of the silicon underneath the cantilever. The method relies on undercut oxide eaves as a means to create an electrical discontinuity between, the top and bottom mirror of each device and between top mirrors in the array. The electrical discontinuity occurs at the underside of the electrically insulating oxide eave. The underside of the eave is left uncoated during the top and bottom mirror metallization.

As discussed earlier there are three other slowly etching (111) planes besides the surface normal. Their intersections with the surface normal create an equilateral triangle with one side perpendicular to the wafer flat. To provide undercut oxide eaves by KOH etching, we avoid exposing the additional (111) facets during the RIE etch step.

Electrical isolation between the cantilever or top mirror and the silicon region below can be achieved by etching a well with the RIE which has two outside walls parallel to the flat on the two opposite sides of the cantilever as shown in Figure 3-10. The Si facet for these sides are the fast etching (110) planes which easily provide an oxide eave after KOH etching. On the sides perpendicular to the line of the flat we must use a more complex wall shape to ensure the presence of an undercut eave following the KOH step. This wall if made simply perpendicular to the flat would be opening on a slowly etching (111) facet so that very little undercutting would occur. However, if the wall is shaped with an opening oriented midway between two (111) facets, undercutting will result. This was done with a 30°–30°–120° triangle wall shape as shown in Figure 3-10.

To electrically isolate the top mirrors of different Fabry-Perot devices from each other, the same method is used. A hexagonal shaped isolation trench is etched around the entire structure with sides oriented for optimal undercutting of oxide eaves. The trench has two sides parallel to the fast undercutting (110) flat with the same 30°–30°–120° triangle capping them as shown in Figure 3-10.

3.4.5 Reactive Ion Etching of the Si Well and Isolation Trench

Following the application of the photoresist or chromium masking layer, the layer is photolithographically patterned resulting in the cross section shown in Figure 3-11. The gas used for the RIE was Poly etch which contains CF_4 diluted with 10% NO_2 .

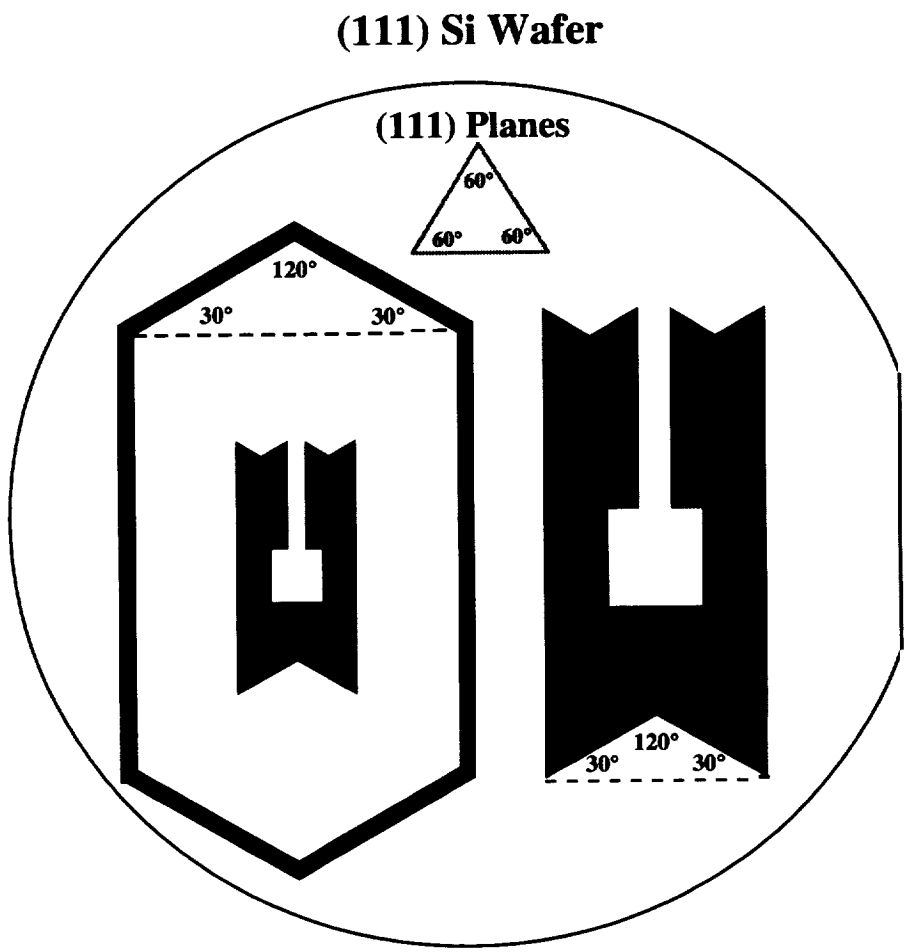

Figure 3-10. The shape of the cantilever silicon well and the hexagonal isolation trench provide electrical isolation between the cantilevers and the underlying Si and between individual cantilevers on the die.

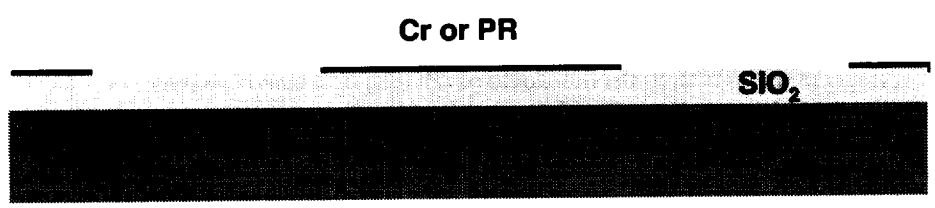

Figure 3-11. A cross-sectional diagram of the wafer showing chromium or photoresist covered regions that are protected during the RIE vertical etching.

The optimum parameters for the RIE were determined to be 50 watts power, 10 sccm Poly Etch, and 30 mTorr pressure. Experiments showed that surface roughness increases with plate power and therefore the lowest possible power of 50 watts was used. The plasma will not ignite below 50 watts. The lower than typical pressure of 30 mTorr was used to provide the highest anisotropy (high mean free path) of the etching to avoid oxide lateral etching. Using the above RIE parameters, the lateral etching was measured to be 30% of the vertical depth. The RIE etch rates of Si, SiO_2, and negative photoresist are shown in Table 3-1.

Table 3-1.RIE Etch Rates of Silicon, Silicon Dioxide, and Negative Photoresist in CF_4.

Material	RIE Etch Rate (Å/minute) 50 Watts, 10 sccm Poly Etch, 30 mTorr
Silicon (111)	376
Silicon Dioxide	120
Shipley 747 Negative Resist	220

Both the SiO_2 and Si were vertically etched with the CF_4 reactive ion etch when chrome was used as the masking layer. It is preferable to etch the SiO_2 layer chemically since RIE etch roughness is an increasing function of etch depth. Attempts were made to etch through the oxide layer first with buffered oxide etch (BOE) containing 10% hydrofluoric acid. However, the adhesion of the chrome to the oxide was marginal enough to permit undercutting and removal of the surrounding oxide layers. The SiO_2 could be BOE etched effectively without undercutting when negative photoresist was used as the RIE masking material. The negative photoresist provided better adhesion. Figure 3-12 illustrates the chip cross-section following the RIE drilling.

3.4.6 KOH Undercutting of the Silicon Dioxide

The step following RIE is chrome or photoresist mask removal using phosphoric acid and an oxygen plasma etcher respectively. The mask materials must be removed before the KOH etching since they will be eventually lifted off without dissolution. The contamination results in a roughened KOH etched silicon surface.

For the KOH undercutting Transene PSE200 Si etchant was generally used. The solution contains potassium hydroxide (KOH) 45% by weight in deionized water with the addition of a proprietary surfactant. The surfactant reduces the surface tension and thereby ensures uniform wetting of the silicon in the well and underneath the cantilever. Etching using a KOH solution without the surfactant results in a much rougher silicon surface.

One cm square chips were cleaved and placed into a Teflon basket suspended in a glass beaker containing the KOH solution. The chips were placed flat, cantilever structures facing upward. This orientation facilitated escape of gas byproducts from the etch reaction. Trapping of these bubbles in the cantilever structure blocks the KOH etchant resulting in increased etched silicon surface roughness. Also, a magnetic stir bar was placed in the beaker to sweep the bubbles out quickly. In general, the temperature of the Transene solution was maintained at 70°C +/- 1°C. This temperature gave high (110)/(111) and (110)/SiO_2 selectivities and a reasonable 35 minute total etch time to undercut the 20 μm wide cantilevers. A total of 45 minutes was required to undercut 50 μm wide cantilevers. Figures 3-13 and 3-14 illustrate the cross-sections of the Fabry-Perot structure during the KOH undercutting.

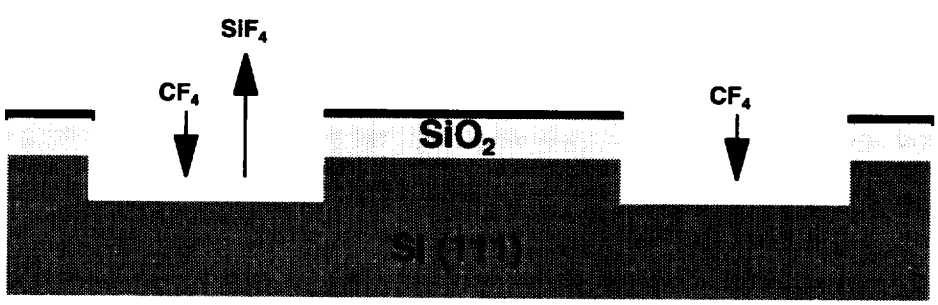

Figure 3-12. A cross section of the wafer following RIE of SiO_2 and Si layers. This step exposes (110) facets for subsequent lateral undercutting of the oxide layer during the KOH etch step.

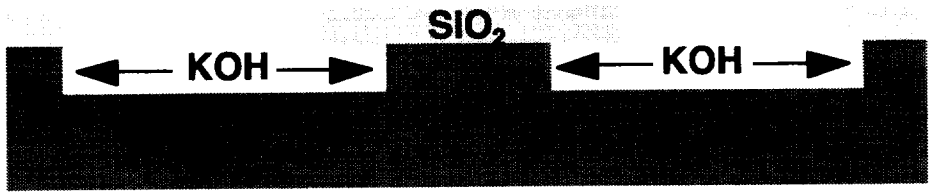

Figure 3-13. Lateral undercutting of the cantilever by rapid wet KOH etching in the (110) direction.

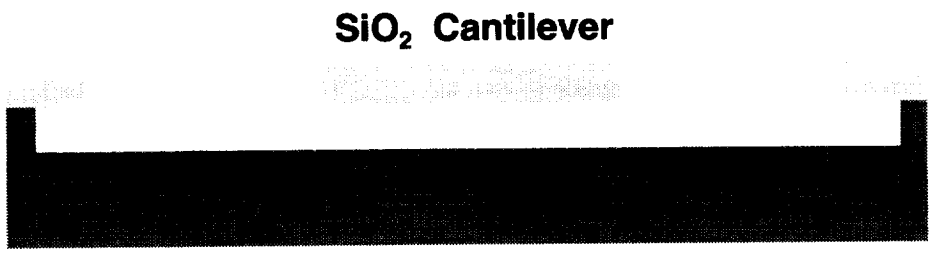

Figure 3-14. The lateral undercutting has completely removed the Si underneath the cantilever.

Optical micrographs showing top views of the Si undercutting evolution are shown in Figures 3-15A-D.

Figure 3-15A shows the profile of an unetched oxide cantilever structure. In Figure 3-15B about 3.5 μm of Si has been etched away from each side of the cantilever and the majority of the perimeter of the well. Figure 3-15C shows about 7 μm of Si removed. Note the formation of two circular pits in the Si well. The origin of the pits could be bubble trapping during etching or a point defect in the silicon. In Figure
3-15D the cantilever is completely undercut except for a few small islands of Si in the center of the cantilever. These islands are made obvious from the presence of circular interference fringes. Continued etching removes the islands. Note also the remaining triangular chunk of Si remaining under the connecting point of the cantilever. The sides of the triangle are (111) etch stop facets. Another crucial observation is the small undercutting in the corners of the Si well. These corners are parallel to (111) facets. The reduced undercutting could potentially result in loss of electrical isolation between the cantilever and the silicon below. Increased magnification reveals that 0.5 to 1 μm of undercutting is present in the corners. The undercutting is the result of a non zero etch rate in the (111) direction and the 30% undercutting provided by the less than anisotropic RIE etch.

Figure 3-16 is a SEM photo of the complete device including the hexagonal isolation trench. The structure has been etched in KOH for 45 minutes. The photo shows that the KOH etching of the hexagonal isolation trench has resulted in a uniformly undercut oxide eave around the inside perimeter. This oxide eave provides electrical isolation between top mirrors of individual devices.

Note also that the extended 45 minute etch has completely removed the triangular section of silicon under the connecting region of the cantilever providing a planar supporting wall of silicon. The planar wall may be more advantageous than the triangular supporting wall since the stress forces during bending are more uniformly distributed. Points of concentrated stress may cause increased fatigue and premature failure of the cantilever.

3.4.6.1 Lower Than Expected KOH Selectivities. A high finesse thin film Fabry -Perot requires smooth parallel surfaces for the mirrors. The crystal orientation dependent etch rates, selectivities, and oxide etch rate of the potassium hydroxide solution can greatly affect the parallelism and smoothness. Etchant temperature, KOH percentage, and crystal alignment are the parameters which affect the etch rates and selectivities.

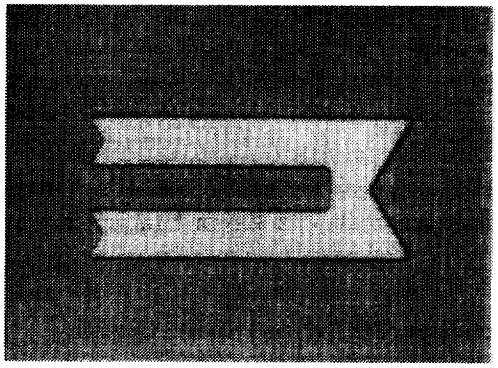

Figure 3-15A. Unetched

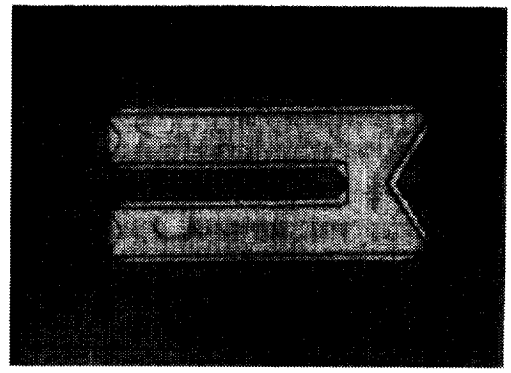

Figure 3-15B. 10 minute etch

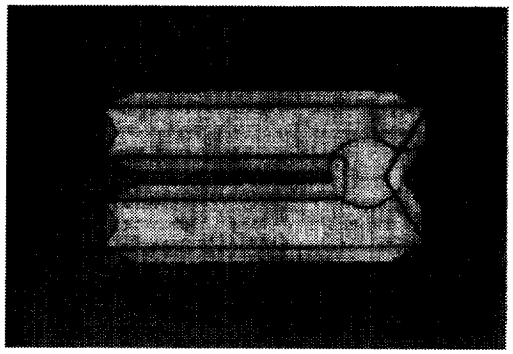

Figure 3-15C. 20 minute etch

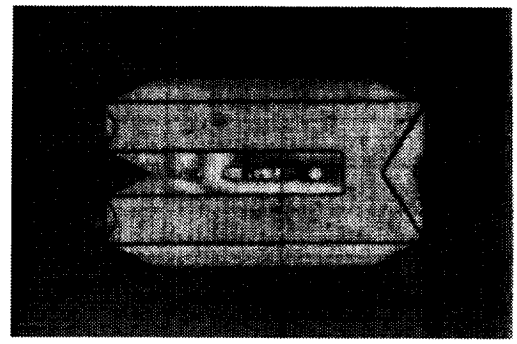

Figure 3-15D. 30 minute etch

Figures 3-15A-D. Optical micrographs showing the evolution of the KOH undercutting as a function of etch time. The cantilever is 20 μm wide and is parallel to the (110) flat.

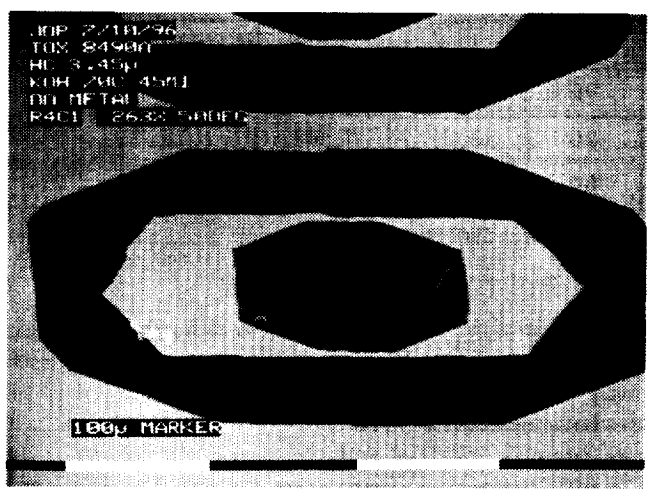

Figure 3-16. A SEM photo of the entire Fabry-Perot structure including the hexagonal isolation trench following 45 minutes of KOH etching. The KOH etching of the hexagonal isolation trench has provided uniformly undercut oxide eaves around the inside perimeter of the trench.

A high (110)/(111) selectivity is desirable for several reasons. A high selectivity permits the undercutting of larger width membranes without deepening the underlying silicon surface thereby yielding cavity length

control to the RIE step alone. Additionally, a small (111) etch rate avoids the convex shaping of the silicon surface underneath the cantilever. The convex shape is a consequence of the longer exposure time of the exterior regions of the Si under the cantilever to the etchant. The convex shape results in a less stable and lower finesse Fabry-Perot. A high (110)/SiO_2 selectivity is also desirable to avoid the convex shape and the loss of mechanical material for the cantilever.

An experimental matrix was carried out to determine the etch rates and selectivities as a function of KOH percentage and temperature. The measured etch rates and selectivities are shown it Table 3-2.

Table 3-2. Measured KOH Etch Rates and Selectivities of Silicon and Silicon Dioxide.

%KOH	Temp.	R(110)	R(111)	R(SiO_2)	R(110)/ R(111)	R(110)/ R SiO_2
% by Weight	°C	µm/hr	µm/hr	Å/hr		
36	50	21.1	0.728	343	29	616
36	55	30.0	0.315	523	95	574
36	60	30.3	0.784	364	39	832
36	80	90.9	1.219	2418	75	376
41	50	13.0	0.260	140	50	929
41	60	24.2	0.571	518	42	468
41	70	54.5	1.573	1026	35	532
41	80	72.7	1.312	1412	55	515
41	90	145	8.759	3420	17	425
45*	50	7.44	0.256	270	29	276
45*	60	9.14	0.115	198	79	462
45*	70	34.8	0.571	1300	61	268
45*	90	71.9	1.252	4334	57	166
50	70	20.8	0.368	1078	57	193
50	80	45.5	0.624	2808	73	162

*Transene PSE200 Solution With Surfactant

The selectivities are given as ratios of the etch rate of (110) to etch rates in the (111) direction and the SiO_2 etch rate. High selectivity ratios are best. From the table, the relation between temperature and (110)/ SiO_2 selectivity is generally monotonic yielding best selectivity at the lowest temperature. Lower KOH concentration also provides better selectivity. The behavior of the (110)/(111) selectivity as a function of temperature is much more complex yielding multiple peaks and valleys. However, the behavior is relatively flat in the 60 to 90°C temperature range using the PSE200 solution. Using the PSE200, the best selectivities occur at 60°C. However, 70°C provides a more reasonable undercutting (110) etch rate (35 μm/hr versus 9 μm/hr) with lower but comparable selectivities.

At 70° C, the typical time to undercut a 20 μm wide cantilever is 35 minutes using PSE200. The less than ideal selectivities result in the etching of 750 Å of oxide and the deepening of the silicon well by 3300 Å. The etching of the SiO_2 and (111) Si is detrimental to Fabry-Perot optical performance since the

silicon surface and cantilever material are being etched and reshaped into nonplanar surfaces. The nonplanar surfaces were observed with an interference microscope.

The measured selectivities were much lower than those reported by others in the literature. Table 3-3 shows the selectivities reported by Waggener et al. [7].

Table 3-3. KOH Etch Rates and Selectivities Reported by Waggener.

%KOH	Temp.	R(110)	R(111)	R(SiO_2)	R(110)/ R(111)	R(110)/ RSiO_2
% by Weight	°C	μm/hr	μm/hr	Å/hr		
9	23	0.49	0.13	5.3	4	920
9	40	4.6	0.49	37	9	1200
9	50	19	0.85	99	22	1900
9	80	100	3.1	1100	32	910
18	23	3.3	0.10	7.5	33	4400
18	40	13	0.32	47	41	2800
18	50	21	0.53	120	40	1800
18	80	130	1.2	1500	110	870
22.5	23	3	0.087	8.6	34	3500
22.5	40	13	0.23	60	57	2200
22.5	50	23	0.42	180	55	1300
22.5	60	41	0.51		80	
22.5	70	69				
22.5	80	130	1.2	1600	110	810
22.5	100	360	3.3		110	
27	23	2.8	0.070	9.7	40	2900
27	40	10	0.24	48	42	2100
27	50	24	0.29	180	83	1300
27	80	130	0.93	1900	140	680
36	23	2.3	0.031	9.9	74	2300
36	40	9.0	0.094	51	96	1800
36	50	22	0.15	130	150	1700
36	80	120	0.69	2100	170	570
45	23	1.2	0.0073	11	160	1100
45	40	4.4	0.026	55	170	800
45	50	10	0.062	180	160	560
45	80	87	0.48	1900	180	460
54	40	1.7	0.0086	24	200	710
54	50	4.2	0.024	81	180	520
54	80	34	0.41	1900	83	180

The values for the etch rates in the (110) directions were comparable to ours. However our etch rates for the (111) directions were much faster by a factor of 2.5. A comparison between Waggener's and our (110)/(111) selectivity is shown in Figure 3-17. Also our SiO_2 etch rates are higher by a factor of 1.5 at 70°C. A graphical comparison of the (110)/SiO_2 selectivity is shown in Figure 3-18.

One source for our much larger (111) etch rates in comparison to Waggener's is the misalignment of our (111) Si wafers with the (111) direction. The apparent (111) etch rate is extremely sensitive to the wafer surface normal misalignment. This behavior has been reported by others in the literature[6].

Referring to Figure 3-19, we have a wafer with its surface normal slightly misaligned (the angle in the Figure is exaggerated). The apparent etch rate in the (111) direction is given by R'(111) and its value is given by the projection of the true rates in the (111) and (110) directions onto the surface normal.

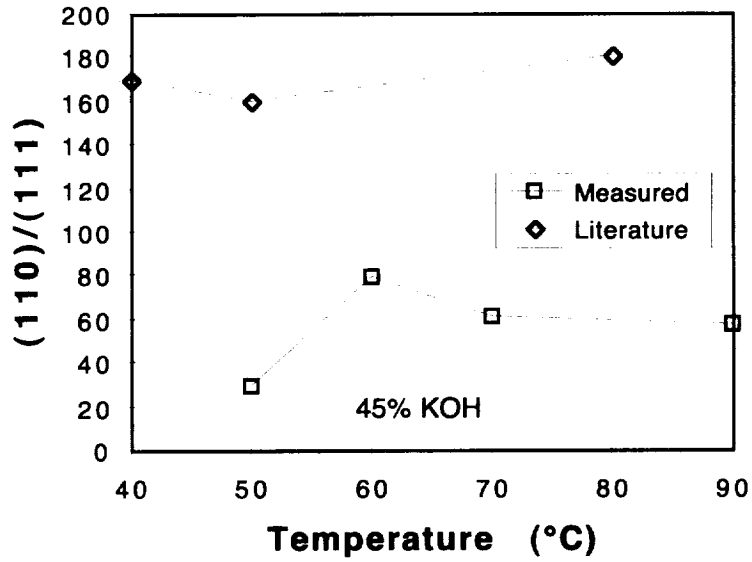

Figure 3-17. A graphical comparison between our measured (110)/(111) selectivities and those reported by Waggener . The KOH percentage of the etchant is 45%.

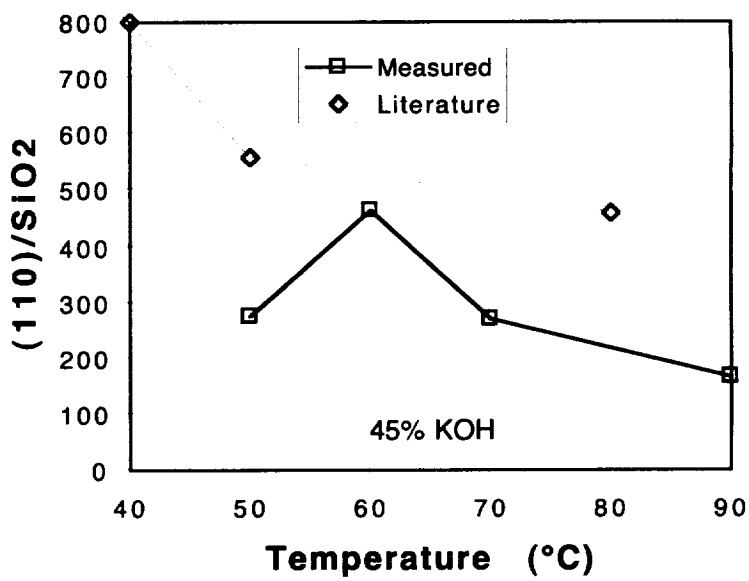

Figure 3-18. A graphical comparison between our measured (110)/SiO_2 selectivities and those reported by Waggener. The KOH percentage of the etchant is 45%.

R(111) in terms of the projections is given by:

$$R'(111) = R(111)Cos(\theta) + R(110)Sin(\theta) \tag{3-3}$$

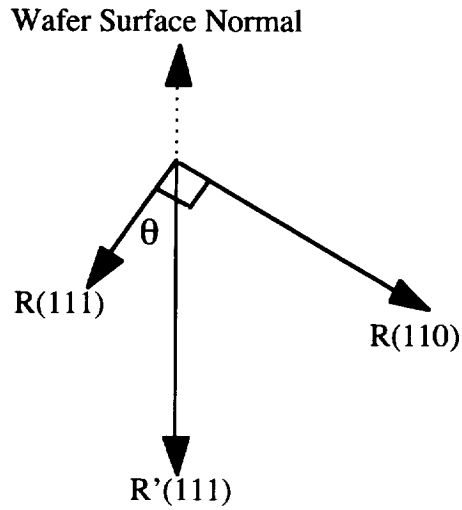

Figure 3-19. The misalignment of the wafer surface normal with the (111) direction results in a much higher apparent (111) etch rate due to the (110) etch rate projection.

The second term on the right side of the equation can be comparable to the 1st term even though Sin(θ) is small, since R(110) can be hundreds of times greater than R(111). The above expression can be rearranged into a more revealing form while assuming a small misalignment:

$$\frac{R(110)}{R'(111)} = \frac{\dfrac{R(110)}{R(111)}}{1 + \dfrac{R(110)}{R(111)} Sin(\theta)} \tag{3-4}$$

For a (110)/(111) selectivity of 160 reported by Waggener for 45% KOH at 60 to 70°C an angular misalignment of 0.5° (the tolerance on our wafers) results in a reduction of the selectivity by a factor of 0.4. to a much lower 66. This selectivity is consistent with our measured values of 61 and 79 at 60 and 70°C respectively.

Our smaller (110)/SiO_2 selectivities in comparison to Waggener's results cannot be a consequence of misalignment, since SiO_2 is amorphous and the (110) rates are comparable. The higher SiO_2 etch rates may be due to the surfactant in the PSE200 or possibly a lower oxide density.

A slight misalignment of the surface normal with the (111) affects not only the selectivity but also produces the same staircase profile exhibited by the 4° tilted wafers but not as severe. Figure 3-20 shows the profile of the Si under a 20 μm wide cantilever. The depth of the silicon under the cantilever varies 388 Å across the 20 μm width. The tilt angle of the wafer was calculated to be 0.13°. Dektak traces on other devices showed angular deviations as high as the 0.5° tolerance. These surfaces evolve during the etching process and produce a wide surface profile variability.

Other observed sources of profile deviation from planarity were pits and terraces. These are believed to be due to Si crystalline defects such as point defects, slip planes, and impurity contamination. The depth of these etch defects were very large for some devices resulting in variations as high as 0.5 μm.

3.4.7 Chip Rinsing and Nitric Acid Treatment

Following the KOH undercutting, the next step is the careful removal of the chips from the teflon basket. The cantilever membranes are fragile at this point since they are freely suspended. The chips are

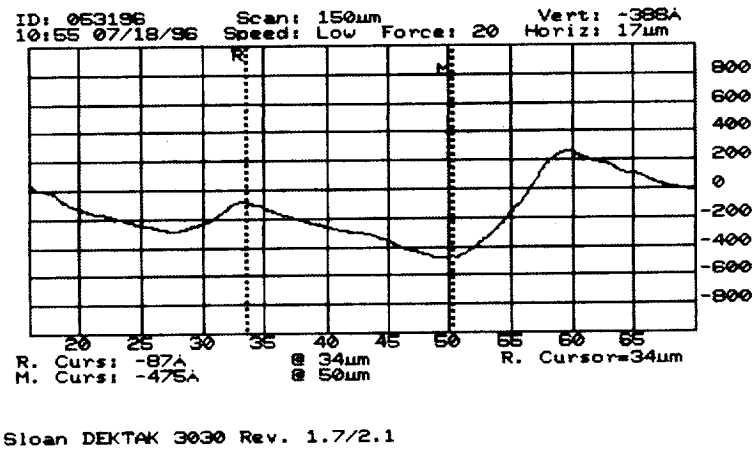

Figure 3-20. A Dektak profile underneath a 20 μm wide cantilever. The profile is measured across the narrow width of the cantilever near the tip. The measured angle between the reference and measurement cursors is 0.13°.

carefully moved to a deionized water rinse tank where the KOH solution is rinsed off. Transport to the tank must be done quickly without drying of the cantilever structures. Air drying will result in the permanent pinning of the cantilevers to the lower silicon surface due to capillary and intersolid forces [11]. Following the final wet chemical step, the metal electroplating of the bottom mirror, the chips are dried using the critical point drying method. CPD drying does not result in cantilever pinning. The method is described in section 3.2.8. Following a careful 5 minute rinse, the chips are then transported to a beaker of 10% nitric acid solution in deionized water for a one minute soak at room temperature. The nitric acid solution is used to remove a water and alcohol insoluble residue on the surface of the Si, which is a byproduct of the KOH etching. The residue has been observed by other researchers [11]. Figures 3-21A and 3-21B show SEM photos of a cantilever membrane with and without the nitric acid treatment.

Note that in both photos, the "air dried" cantilevers are pinned to the Si surface. Removal of the cantilever revealed the absence of the residue under the cantilever even without the nitric acid soak. This is shown in Figure 3-22. This indicates that the residue formation is probably related to the reactive ion etching.

Following the nitric acid cleaning, the chip is again rinsed in deionized water for 5 minutes.

3.4.8 Metal Electroplating of the Lower Mirror

The next part of the process is the application of a high reflectivity metal to the silicon layer underneath the cantilevers. This layer underneath serves as the lower mirror to the Fabry-Perot structure. The silicon alone provides for only 30% reflectivity (refractive index = 3.875 at a wavelength of 632.8 nm) and would result in a low finesse Fabry-Perot. In general, simple evaporative methods deposit extremely smooth metal films which are of optical quality. This is the desired method. However, evaporative methods cannot be used to deposit metal on the silicon surface under the cantilevers. This is due to the close proximity and consequent shadowing effect of the cantilevers to the silicon surface (on the order of micrometers). The obvious alternative for the metallization is electroplating. The advantage of metal electroplating over evaporation is the ability of the plating solution to plate surfaces in extremely

confined spaces such as the silicon underneath the cantilever. Another advantage of electroplating is its plating selectivity to conductors. The silicon can be electroplated while the oxide is not, thereby preserving the electrical isolation between the cantilever mirror and the silicon based mirror below. Gold is the desired metal for both the top and bottom mirrors, since it provides a high reflectivity in the infrared (97%) and does not oxidize (like silver). Smooth and adherent gold films can be easily plated to other metals. However, these high quality gold films cannot be directly electroplated onto silicon. Smooth, adherent,

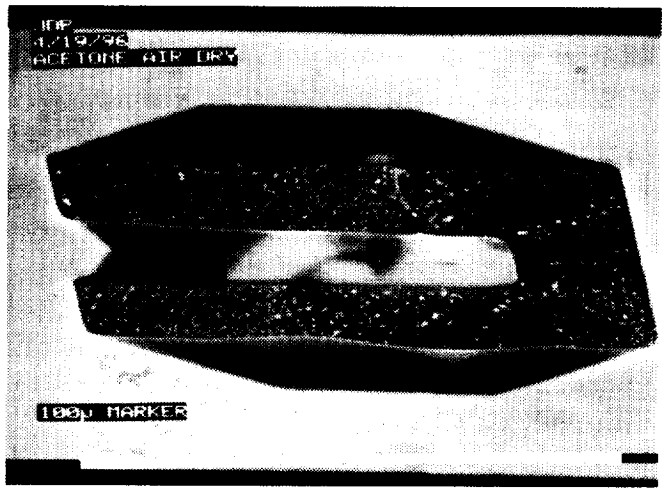

Figure 3-21A. A SEM photo of a cantilever Fabry-Perot structure showing the KOH etch residue on the silicon (white specks). This device was rinsed with water followed by acetone.

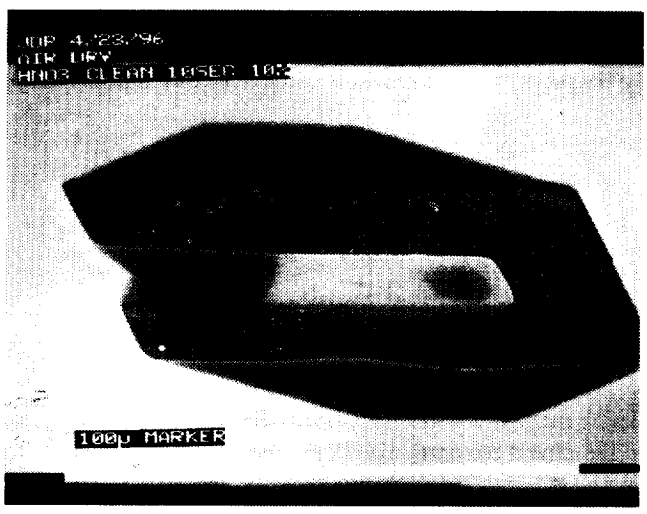

Figure 3-21B. A SEM photo of a cantilever Fabry-Perot structure showing the absence of the residue when the device is cleaned with nitric acid.

nickel films, on the other hand can be, as evidenced by the large number of micro-machines employing plated nickel. Nickel provides a much lower reflectivity (67%) than gold (97%). However, with the base nickel plated to the silicon, it can be replaced substitutionally by electroplated gold [12]. Here we present the electroplating method, results, and problems for nickel. Substitutional replacement of the nickel with gold is left for future work.

There are basically two electroplating methods. The first is the standard technique in which a voltage is applied between a metal ion containing solution and the conductive item being plated. The voltage

produces a metal ion current which transports metal to the plated surface. The disadvantage of this technique is poor plating uniformity on uneven surfaces. The plating current density generally follows the density of electric field lines between the solution electrode and the plated material. The density of the field lines is extremely uniform between two smooth parallel plates. This would be true for a flat solution electrode and a smooth flat piece of silicon. However, the Fabry-Perot chip is not smooth and contains complex topography so the field lines are nonuniform. This explains the high roughness, Ra = 1000 Å which was observed during an electroplating experiment where we attempted to plate gold to the Si surface

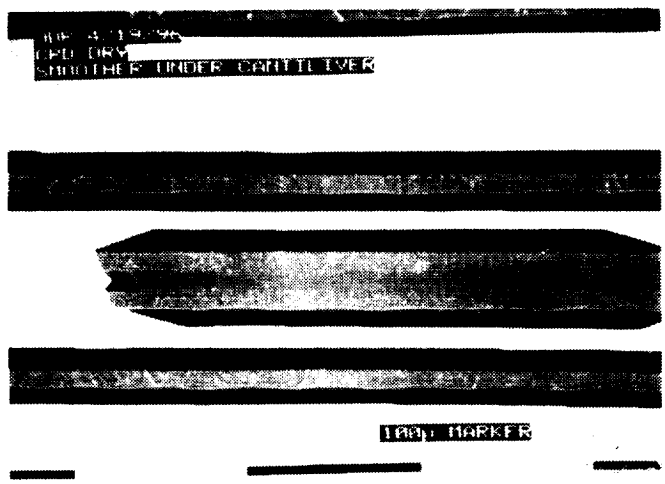

Figure 3-22. A SEM photo of the cantilever Fabry-Perot structure showing the absence of the residue under the cantilever. This device was not cleaned with nitric acid.

of a Fabry-Perot chip. R_a is a industry standard for roughness measurements and is defined as the mean deviation from the average height of the surface and is mathematically represented by

$$R_a = \frac{1}{L}\int_L |y(x) - \bar{y}|dx$$

$$R_a \rightarrow \textit{average roughness}$$

$$y \rightarrow \textit{vertical height}$$

$$\bar{y} \rightarrow \textit{average height}$$

$$L \rightarrow \textit{lateral range of roughness measurement} \qquad (3\text{-}5)$$

The second electroplating method is called electroless plating. This method requires no external voltage between the solution and the plated material. However the difference in chemical potential between the solution and material being plated must be of correct polarity and additionally competing processes besides plating must be minimal. That is, the plating efficiency depends greatly on the chemistry between the plating solution and the material being plated. On the other hand, the advantage of electroless plating is metal plating uniformity independent of surface topography.

ENPAT (Electroless Nickel Plating Ammonia Type) is a popular and successful nickel electroless plating solution [13] (ENPAT is a trademark of Transene Inc. of Rowley MA). This solution plates adherent and uniform films of nickel to both n or p type silicon. An electroless gold plating solution is available called Bright Electroless Gold which is also sold by Transene Inc. [14]. It cannot not be electrolessly plated directly to Si. However, its chemistry allows plating to nickel by substitutional replacement [12]. That is, plating occurs through ion exchange, gold atoms replacing Ni atoms which go into solution. According to chemists at Transene the replacement can go almost to completion with only a few atomic layers of nickel remaining. So the plating can be done in a two step process, first plating with

nickel, then replacement with gold using ion exchange.

Ni plating of the Fabry-Perot structures was carried out with the following procedure which was optimized for smooth and adherent layers. Chips were transported in a deionized water solution to the plating hood with care to avoid any potential air drying. The next step was a quick 10% BOE dip (Buffered Oxide Etch) for 10 seconds. This step was necessary to remove any native oxide present on the Si which would prevent nickel plating. Following the BOE dip, the chip was carefully placed into a beaker containing the ENPAT solution. The chip was suspended in the solution with a pair of plastic hemostats. The chip was continuously agitated by hand. Additionally, the solution was stirred vigorously with a magnetic stir bar to prevent gaseous bubbles from building up in the cantilever wells. These bubbles are a byproduct of the plating reaction and their presence results in nonuniform plating.

The temperature of the plating solution was maintained at 95°C with a hot plate and a surrounding water bath. The temperature of the solution must be greater than 90°C to provide plating. The temperature must be greater than 90°C in order to crack and ionize the Ni containing molecule in the plating solution.

The pH of the solution must be accurately controlled in order to obtain reproducible plating rates. This was done by the addition of ammonium hydroxide to maintain a pH of 10. The pH of the solution was continuously decreasing due to the evaporation of ammonium hydroxide which is extremely rapid at the 95°C boiling temperature. The rapid evaporation caused large deviations of the nickel plating rates and consequently resulted in poor control over the film thickness.

The chips were generally plated for 3 minutes resulting in a 500 Å thick nickel layer. Figure 3-23 shows a cross-sectional diagram of the Fabry Perot structure following Ni plating. Note that the nickel has selectively plated the silicon without plating the silicon dioxide. The plating selectivity preserves the electrical isolation between the top and bottom mirrors.

Figure 3-24 is an optical micrograph showing a top view of the Ni electroplating on a 3.2 μm deep Fabry-Perot. Note the blackish fuzz around the perimeter of the isolation trench and the (110) sides of the Si well. Under higher magnification the fuzz is revealed to be long thin strands or fingers of nickel. The fingers concentrate in regions of pronounced silicon roughness or sharp corners. Ni roughnesses as good as $R_a = 37$ Å was observed in these wells.

Ni plating was not successful, however, for the short cavity Fabry-Perots (<0.6μm). The tiny space between the cantilever and the Si surface was not sufficient to provide for uniform plating solution and gas byproduct flow. That is, both liquid and gas bubbles were stagnant underneath the cantilever. The result was extremely rough Ni plating under the cantilever. The roughness also was accompanied by long nickel finger growth that resulted in total loss of electrical isolation between the top and bottom mirrors. A microphotograph of a nickel plated 0.6 μm gap Fabry-Perot is shown in Figure 3-25. Note the dark rough nickel plated regions under the oxide, cantilever and eaves. A 0.2 μm increase in the well depth (due to a Si terrace) occurs at the right end of the cantilever. The increase in depth results in smoother plating.

3.4.9 Drying of the Cantilever Structures Following Wet Processing

3.4.9.1 Drying Through Room Air Evaporation and the Pinning/Sticking Problem. From initial immersion in the KOH solution to this point, the chips have not been allowed to air dry. As was mentioned previously, if the chip is dried, the cantilever structures will become permanently pinned down to the Si surface [11]. The pinning process is the result of two types of forces. First the cantilever is pulled down to the Si surface as a result of attractive capillary forces and liquid evaporation. After the cantilever makes contact with the silicon surface, strong attractive intersolid forces (Van der Waals forces) hold the cantilever fast to the Si surface. The pinning problem is well known within the MEMS research

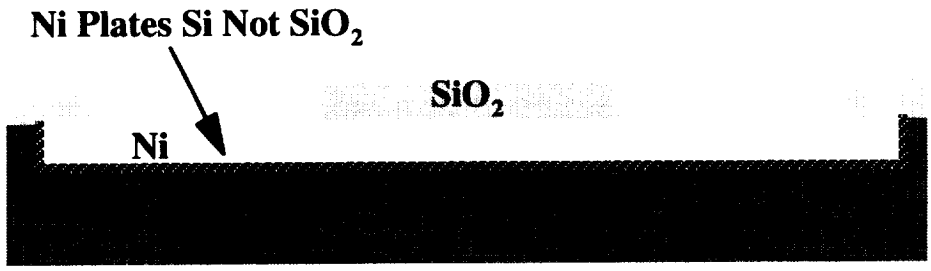

Figure 3-23. A cross-sectional diagram of the Fabry-Perot structure following Ni plating. The Ni has plated only the Si and not the SiO_2 preserving the electrical isolation between the top and bottom mirrors.

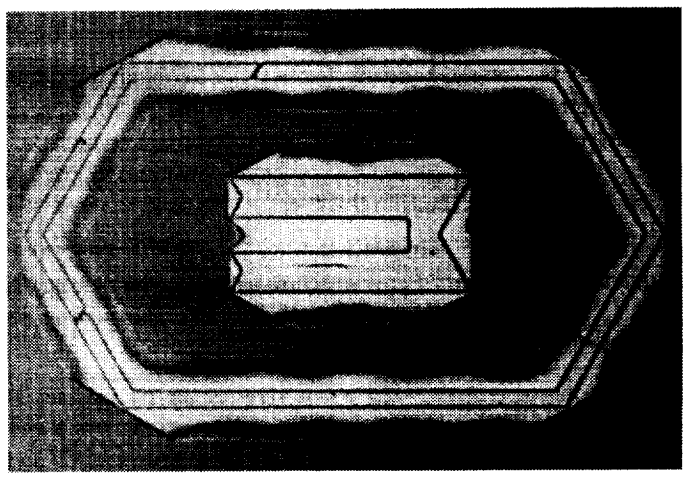

Figure 3-24. An optical micrograph of a Ni plated 3.2 μm cavity Fabry-Perot.

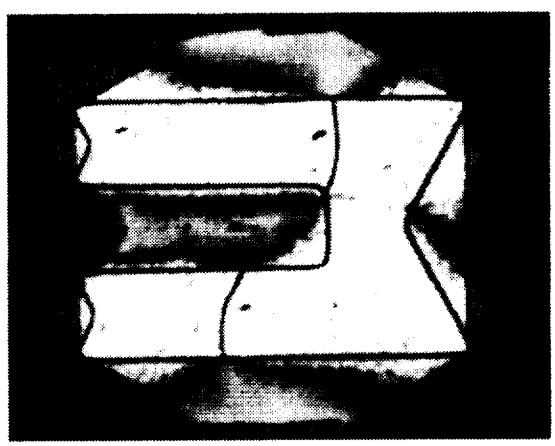

Figure 3-25. An optical micrograph of a Ni plated 0.6 μm air gap Fabry-Perot. Note the rough Ni plating under the cantilever and oxide eaves. The roughness is a consequence of poor plating solution and gas transport in the narrow gap.

community. Most researchers fabricating air gap micro-mechanical Fabry-Perots avoid the pinning problem by using dry etching methods to remove the sacrificial layer [15]. However, dry etching methods are generally isotropic, and consequently are not compatible with our crystal orientation dependent technique.

The pinning process is depicted in Figure 3-26. In Figure 3-26A the water underneath the cantilever is just beginning to evaporate at the edges. There exists an attractive force between the water and the SiO_2 cantilever (water wets oxide). There also exists an attractive force between the silicon substrate and the water due to the presence of a thin native oxide on the silicon or the nickel. As shown in Figure 3-26B, the end of the cantilever is pulled down as the water droplet evaporates. In Figure 3-26C the cantilever tip has been completely pulled down to intimate contact with the Si where it is held fast by Van der Waals forces.

All cantilever Fabry-Perots that were air dried during this study exhibited the pinning behavior except a small percentage of the Ni plated samples. Many air drying solutions were tried to no avail, water, methanol, ethanol, isopropanol, and acetone, with both slow room-temperature drying and accelerated oven drying. Pretreatment with BOE to remove the native oxide was also attempted. However, the native oxide grew back rapidly, since pinning still occurred. Figure 3-27, shows a typical air dried cantilever pinned to the Si surface.

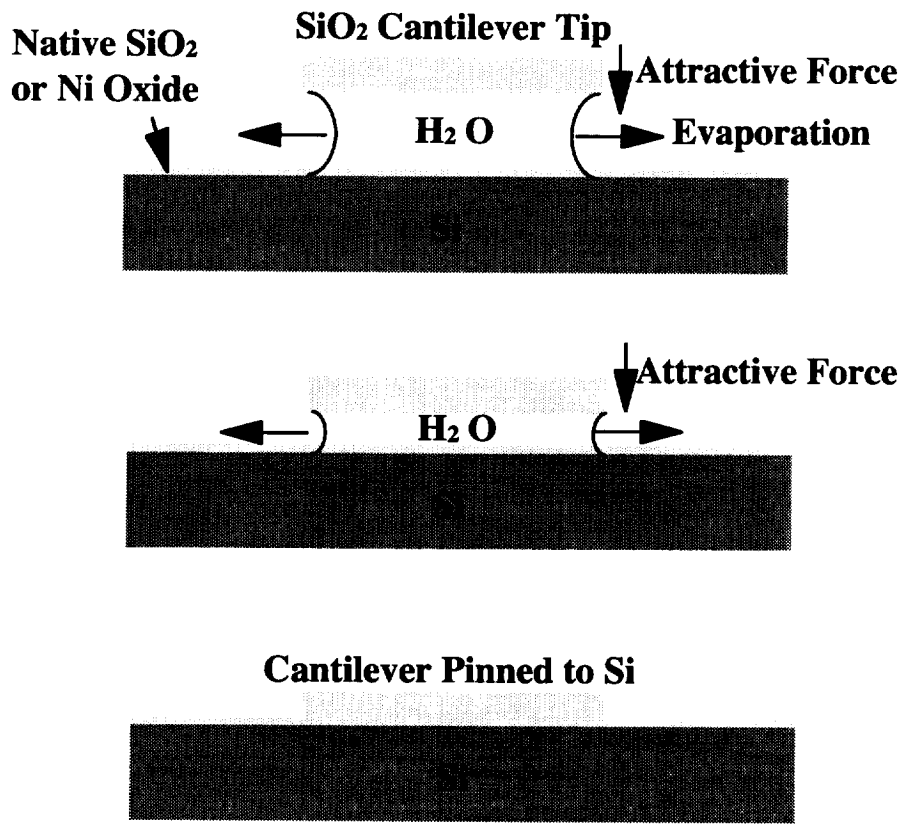

Figure 3-26A–C. The pinning process of a cantilever that is dried through room air evaporation.

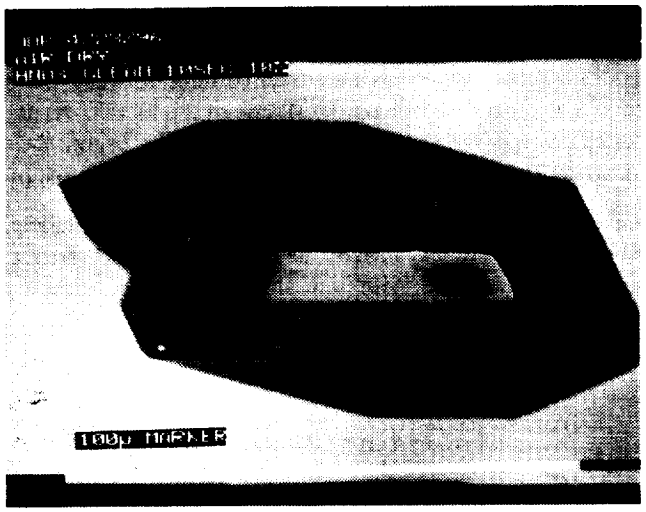

Figure 3-27. A SEM photo of an room air dried cantilever that is pinned down to the Si surface due to capillary and Van der Waals forces.

Figure 3-28 shows a SEM photo of an air dried cantilever Fabry-Perot which includes the electrical isolation trench.

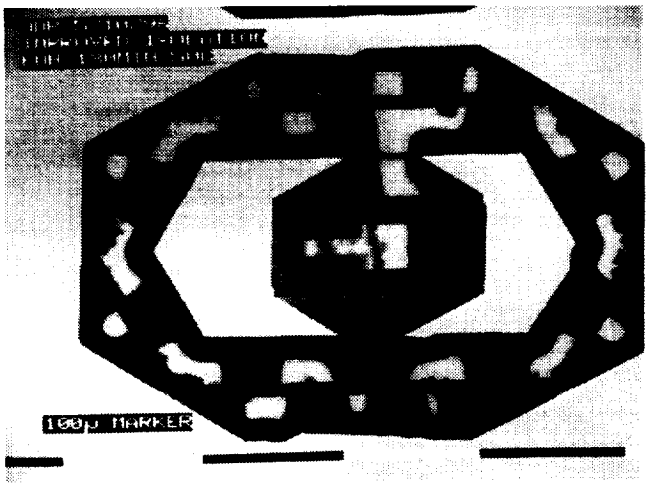

Figure 3-28. A SEM photo of an air dried Fabry-Perot including the surrounding hexagonal isolation trench. Note that the oxide eaves around the trench have been pulled down into contact with the Si. These contact points will result in the loss of electrical isolation between the top and bottom mirror metallization.

Note that the oxide eaves used for the electrical isolation have been pulled down into contact with the Si at many points. These electrical shorts are visibly shown as the bright white regions surrounded by dark areas around the perimeter of the hexagonal isolation trench. The contact points will provide electrical shorting paths between the metal on top of the cantilever and the Si/Ni layer below.

3.4.9.2 Critical Point Drying. A method by which the Fabry-Perots can be dried without pinning is Critical Point Drying (CPD) [16, 17]. CPD has been used for many years by biologists interested in looking at fragile and normally wet biological samples with a high vacuum Scanning Electron Microscope (SEM). Succinctly put, CPD drying permits surface tension force free drying, because a

liquid/air interface is never allowed to develop.

The critical point of a liquid/gas system is the critical temperature and pressure on the phase diagram. Below the critical temperature the system is entirely in a liquid state. Above the critical temperature the system is always gaseous and cannot be converted by pressure changes. The transition from liquid to gas at the critical point takes place without an interface because the densities of the liquid and gas are the same at this point. If the sample is totally immersed in liquid and taken above its critical point then it will be instantaneously dried without surface tension forces.

A Balzers Union Model CPD 020 critical point dryer was used to dry the Fabry-Perot chips. The unit consisted of a stainless steel pressure vessel complete with temperature controller. The liquid used for the CPD was bone dry (no water) liquid CO_2 which has a critical temperature and pressure of 31°C and 1073 psi (73 atm) respectively. Chips were transferred from the deionized water rinse to a liquid miscible with CO_2 either ethanol or acetone and then placed into the CPD pressure vessel which contained enough ethanol to cover the chip. The chamber was then reduced from room temperature to 5°C to ensure that incoming CO_2 liquid wouldn't rapidly and violently convert to gas potentially damaging the cantilevers. The chamber was then flushed with CO_2 until no odor of ethanol remained at the exhaust port, i.e., complete replacement of the ethanol with CO_2.

Following complete replacement with CO_2 liquid, all chamber valves were closed and the temperature raised through and past the critical point. Observation through a glass viewing port during the critical point transition showed the expected interface free transition of the CO_2 from a liquid to a gas. The final temperature of the chamber was raised to 45°C to ensure that recondensation of the CO_2 gas did not occur during the exhaust phase. The final part of the drying was the opening of the exhaust port allowing the gas to escape from the chamber. This was done slowly over a period of 30 minutes to avoid gas flow damage to the cantilevers. Figures 3-29 and 3-30 shows SEM photos of cantilever Fabry-Perots that have been dried with the CPD method. The cantilevers are erect and the oxide eaves haven't been pulled down into intimate contact with the Si.

3.4.10 Top Mirror Metal Evaporation.

The final step of the fabrication of the micro-mechanical Fabry-Perot filters is the evaporation of gold metal onto the top side of the SiO_2 cantilever. This metal will provide a high reflectivity which is necessary for a high finesse Fabry-Perot. The gold also provides a means of moving charge onto the cantilever which results in the electrostatic bending force.

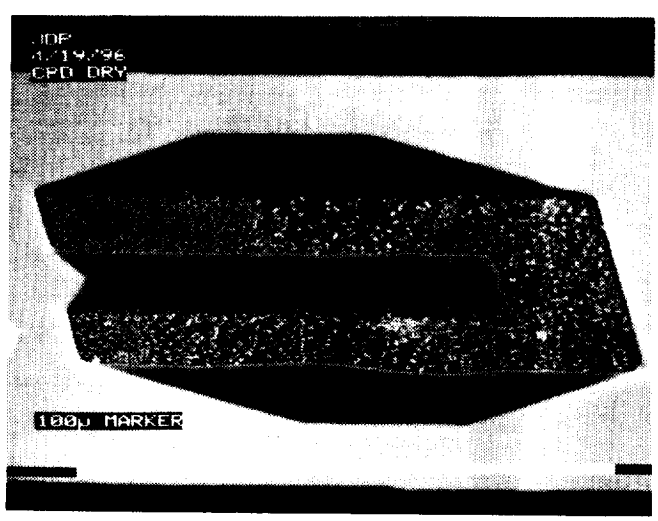

Figure 3-29. A SEM photo of a CPD dried cantilever which is erect in contrast to the air dried structures.

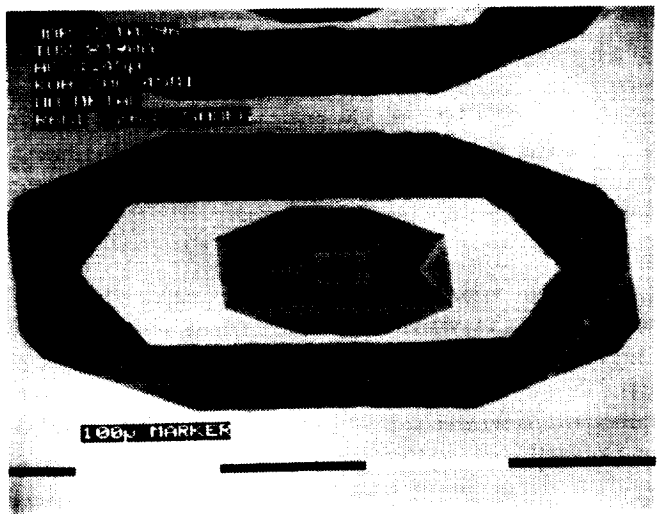

Figure 3-30. A SEM photo of a CPD dried cantilever Fabry-Perot which is erect. Note also that the oxide eaves used for the electrical isolation are not in contact with silicon layer below in contrast to the air dried devices.

An evaporation system was used to deposit gold onto the top mirror. Use of the evaporation system for this purpose provided several advantages. The evaporation system can deposit extremely clean and smooth films due to the low pressures obtainable with the diffusion pump (0.1 μTorr). Additionally, the metal flux is very anisotropic in comparison to a sputtering system due to the low pressure in the chamber and the point source nature of the metal flux. The anisotropy of the flux is extremely important to the fabrication of the Fabry-Perots, since we rely on electrical discontinuity between the top and bottom mirrors through the shadowing effects of the undercut oxide eaves. Figure 3-31 shows a cross-sectional diagram following the gold evaporation. Note the discontinuity between the top metal and bottom metal at the underside of the SiO_2 eaves.

A microphotograph of a completely processed cantilever based Fabry-Perot is shown in Figure 3-32 below.

The silicon under the cantilever is plated with 500 Å of nickel, while the top side of the cantilever and regions not shadowed have been coated with 300 Å of gold. The air gap under the cantilever is 3.2 μm as measured with a profilometer.

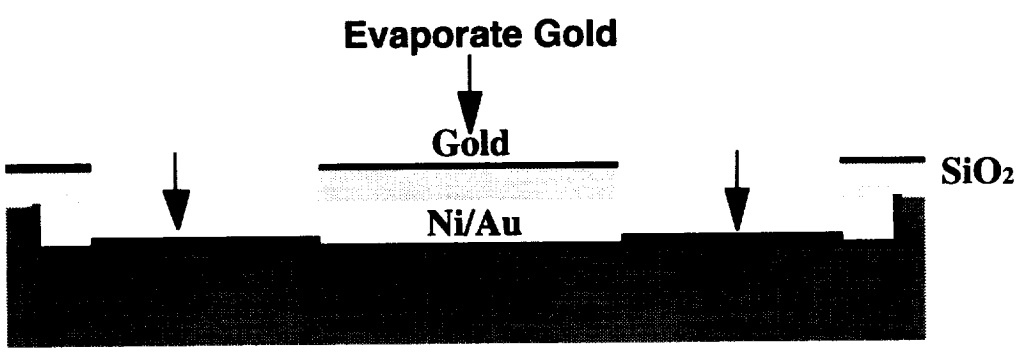

Figure 3-31. A cross-sectional diagram of the cantilever Fabry-Perot following the top mirror gold evaporation. Note the electrical discontinuity provided by the underside of the oxide eaves.

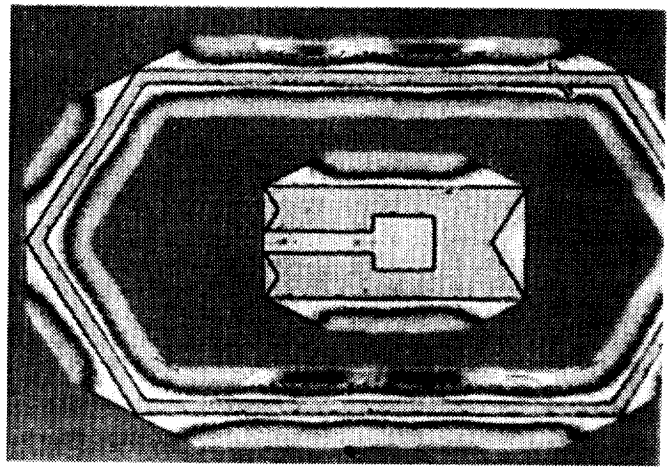

Figure 3-32. A microphotograph of a completely processed micro-mechanical tunable optical filter based on a movable cantilever mirror. The top side of the cantilever is coated with gold. The silicon underneath the cantilever is plated with nickel.

3.4.11 Stress Induced Cantilever Mirror Curvature

The high growth temperature of the thermal oxide (1000°C) and the large difference in the coefficients of thermal expansion between Si (2.33×10^{-6}/°C) and SiO_2 (0.55×10^{-6}/°C) can result in stress problems. Since silicon dioxide has a much lower thermal coefficient of expansion than silicon it is compressively stressed following removal from the furnace and cooling. The stress problems are usually manifested as unwanted curvature and in severe cases breakage. In the case of the Fabry-Perot structures, the thermal stress results in unwanted upward curvature of the cantilever. The curvature results in a lower finesse Fabry-Perot due to the loss of mirror parallelism. Figure 3-33 illustrates the curvature problem. The Figures are SEM photos of the cantilevers taken at a 50 degree tilt angle to emphasize the curvature. The cantilevers have been coated with 165 Å of gold but were not nickel plated. The width of the cantilevers is 20 μm. The photos depict the same cantilever structure but with increasing oxide thickness. The 970 Å thick oxide cantilever exhibits the most severe curvature. It is noticeably curling both along its width and length due to the stress at the oxide/silicon interface. The curvature of the cantilever is reduced by increasing the oxide thickness. The thickest oxide provides a higher film stiffness to bending. The least amount of curvature is exhibited by the 8300 Å thick cantilever (the thickest cantilever).

Another detrimental affect of the stress is the noticeable oxide eave ripple around the perimeter of the cantilever well. The amplitude of the ripples can be high enough to allow contact between the top mirror region and the nickel plated silicon below creating an electrical short.

All cantilevers fabricated in this study exhibited some degree of curvature. We believe the cause of the curvature is stress, but another question remains. Where does the stress concentrate itself in the cantilever and can it be avoided while using a thermally grown oxide? Some further observations reveal answers to this question. Note that in the Figure 3-33 that the cantilevers exhibit an increased slope in the upward bending as one moves toward their tips. This suggest that the stress inducing curvature is not entirely concentrated at the silicon connecting region. The stress is obviously distributed across the entire length of the freely suspended cantilever. Furthermore, to provide the upward bending, the bottom region of the cantilever must be in compression while the top region is in tension. One source of the stress profile could be due to defects or impurities present at the silicon/ silicon dioxide interface or any other mechanism which results in a nonuniform stoichiometry and density during the thermal growth of the oxide. Another source of the stress profile could also be plastic deformation of the interfacial oxide cantilever during the KOH undercutting and release process. This explanation has been presented by other researchers in the literature [10,18].

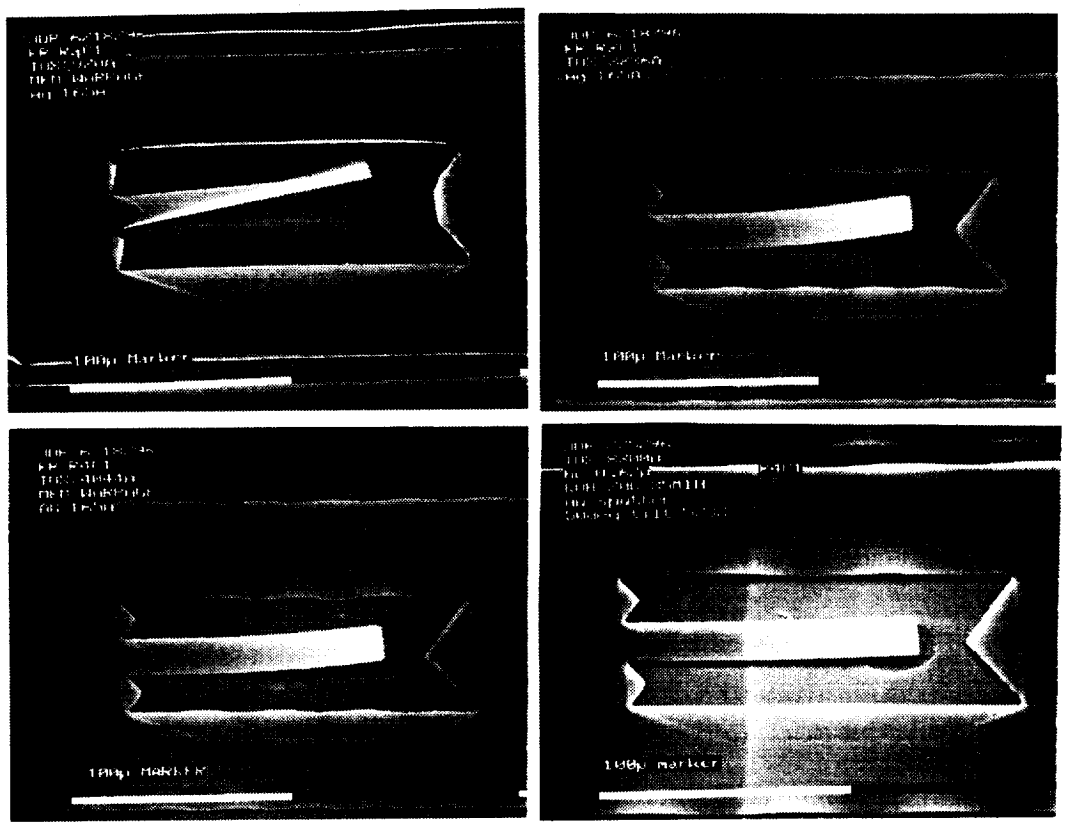

Figures 3-33. SEM photographs illustrating the stress induced upward cantilever curvature. Thicker oxide cantilevers curve less.

They suggest that the compressive stress on the interfacial oxide layer which is in intimate contact with the silicon can be high enough to plastically damage the layer during release. That is, the interfacial oxide under high compression has stored a large amount of spring energy. During undercutting, the spring energy is released allowing the interfacial oxide to expand beyond its plastic limit. These explanations which suggest an interfacial stress source for the bending are both consistent with the reduced bending of the thicker cantilevers. Wilmsen et al. have shown analytically that the stress limit for the plastic deformation is geometry dependent for square membranes held on all sides (oxide windows) [10]. He presents upper and lower bounds on the oxide thickness to window dimension ratio that do not result in plastic deformation following release. However, his theory is not directly applicable to freely suspended cantilevers. Further analytical work is needed to determine whether such bounds exist for cantilevers grown with thermal oxidation and whether the geometry constraints are practical for micro-mechanical Fabry-Perot fabrication.

An mentioned in section 3.1.4, one simple solution to the cantilever bending problem is to use low temperature CVD silicon nitride (low stress) as the cantilever material instead of thermal oxide. This solution totally avoids any potential geometry constraints on the shape or thickness of the cantilever structure. Silicon nitride may be a better candidate for the cantilever material and should be considered for future studies.

3.5 References

1. Tran, A. T. T. D., et al., Surface Micromachined Fabry-Perot Tunable Filter, *Photonics Tech. Ltrs.*, **8**(3), pp. 393–395, 1996.

2. Wu, M. S., et al., *Widely tunable micromachined gallium arsenide fabry-perot filters* in *IEEE/LEOS*, Keystone, CO, 1994.

3. Petersen, K. E., *Silicon as a mechanical material,* Proceedings of the IEEE, **70**(5), pp. 420–457, 1982.

4. Schwartz, B., Chemical Etching of Silicon, *J. of the Electrochem. Soc.*, 1976. (12): pp. 1903–1909.

5. Seidal, H., et al., Anisotropic Etching of Crystalline Silicon in Alkaline Solutions, *J. of the Electrochem. Soc.,*. **137**(11), pp. 3626–3632, 1990.

6. Seidal, H., *Crystalline Semiconductor Micromachining* in Transducers '87 Rec. of the 4th Int. Conf. on Solid-State Sensors and Actuators, pp. 120–125, 1987.

7. Waggener, H. A., R. C. Kragness, and A. L. Taylor, KOH Etching of Si, *Elect.*,**40**, p. 274, 1967.

8. Choi, W. S. and J. G. Smits, A method to etch undoped silicon cantilever beams, *J. of Microelectro. Sys.,*. **2**(2), pp. 82–86, 1993.

9.Sze, S. M., *Oxidation and Film Deposition,* in *Semiconductor Devices: Physics and Technology*, Murray Hill, NJ, pp. 360–362, 1985.

10. Wilmsen, C. W., E. G. Thompson, and G. H. Meissner, Buckling of Thermally-Grown SiO2 Films, *IEEE Trans. Elect. Dev.*, (1), p. 122.,1972.

11. Mastrangelo, C. H. and C. H. Hsu, Mechanical Stability and Adhesion of Microstructures: Part I: Basic Theory, *J. of Micro-mech. Sys.*, **2**(1), pp. 33–43, 1993.

12. Queau, E., et al., Electroless Metal Deposition as a Useful Tool For Microelectronics and Microstructures, *J. of Electrochem. Soc.*, (1), pp. 65–69, 1994.

13. Transene Inc. Literature, *Advanced Materials For Electronics*, Transene Inc., Rowley, Mass., pp. 126–127, 1981.

14. Transene Inc. Literature, *Advanced Materials For Electronics*, Transene Inc., Rowley, Mass., p. 138–139, 1981.

15. Harris Jr., J. S., M. C. Larson, and A. R. Massengale, *Coupled -cavity laser diode with micromachined external mirrors* in *IEEE/LEOS 1996 Summer Topical Meetings: Optical MEMS and Their Applications.* Keystone, CO, pp. 31–32, 1996.

16. Burstyn, H. P., Critical point drying: Application of the physics of the PVT surface to electron microscopy, *Am. J. of Phys.*, **43**(5), pp. 414-419, 1975.

17. Ho, S. T., et al., High index contrast mirrors for optical microcavities, *App. Phys. Ltrs.*, **57**(14), pp 1387–1389, 1990.

18. Jolly, R. D. and R. S. Muller, Miniature Cantilever Beams Fabricated by Anisotropic Etching of Silicon, *J. of Electrochem. Soc.*, Solid State Science and Technology, **127**(12), pp. 2750–2754, 1980.

IV. Electro-Mechanical and Electro-Optical Characterization

4.1 Introduction

In this chapter, the electro-mechanical and optical characteristics of the micro-mechanical modulators are presented. The characterization includes a voltage-contrast SEM study of the motion of a cantilever under bias. The SEM study also provided a qualitative indication of the effectiveness of the designed electrical isolation. Following, the wavelength resolved characteristics of the modulators are presented. Spectral measurements were taken with both a tunable laser and a broadband LED. Time resolved measurements are presented in section 4.4. Here the frequency response characteristics of the optical modulator are discussed. Comparisons between theoretical predictions and experimental results are included.

4.2 SEM Characterization of the Electro-Mechanical Behavior

The electro-mechanical behavior of a micro-mechanical tunable Fabry-Perot filter was studied in a SEM. A 1 cm by 1 cm sized chip containing approximately 600 devices was mounted on an SEM stage equipped with electrical probes. One probe was used to make contact to the top mirror region of the filter. Electrical connection to the silicon substrate was provided by backside contact with the probe stage. Electrical connection to the stage was made via an electrical feedthrough into the SEM chamber. A DC voltage supply connected in series with a floating ground AC function generator (DC to 1 MHz) was used to drive the modulator.

A SEM photo and a cross-sectional diagram of the cantilever modulator studied in the SEM are shown in Figures 4-1 and 4-2. The cantilever consists of a 20 nm gold coated, 470 nm thick SiO_2 membrane. The tip of the cantilever is separated from the Si surface by a 7.5 μm air gap when no bias is applied.

The surface geometry of the cantilever is a 55 μm square mirror pad supported by two 28 μm long legs. Originally the pad was supported on the other side by two more legs. This is obvious from the remnants of the oxide legs at the end of the cantilever. Inadvertently, but fortunately, the processing resulted in the breakage of these two legs forming the more flexible cantilever structure. The yield for complete structures is around 95%.

Electrical isolation between the top mirrors of individual Fabry-Perot devices and between the top mirrors and the underlying Si was observed using voltage contrast SEM. Figure 4-3 shows 16 of the Fabry-Perot structures with the top mirror of one cantilever structure electrically contacted with a probe

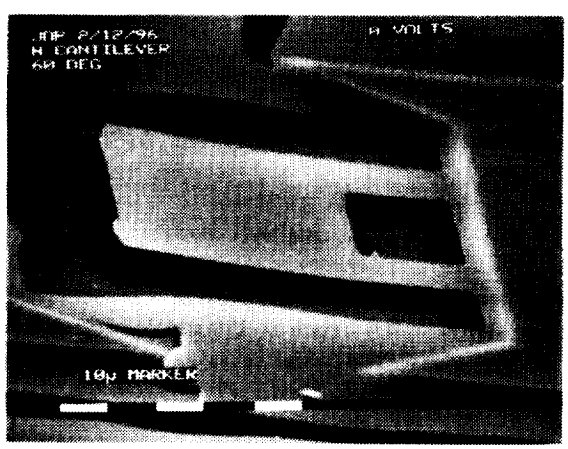

Figure 4-1. A photo of the cantilever modulator studied under bias in the SEM.

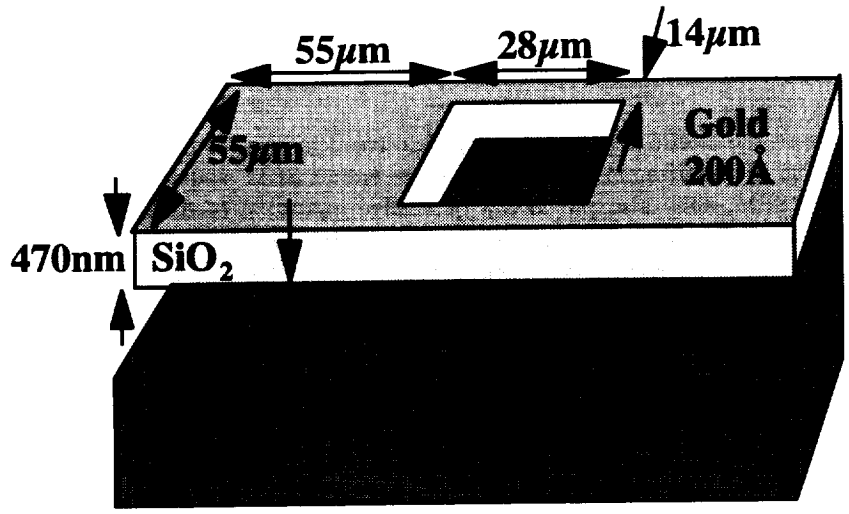

Figure 4-2. A cross-sectional schematic of the cantilever modulator studied in the SEM.

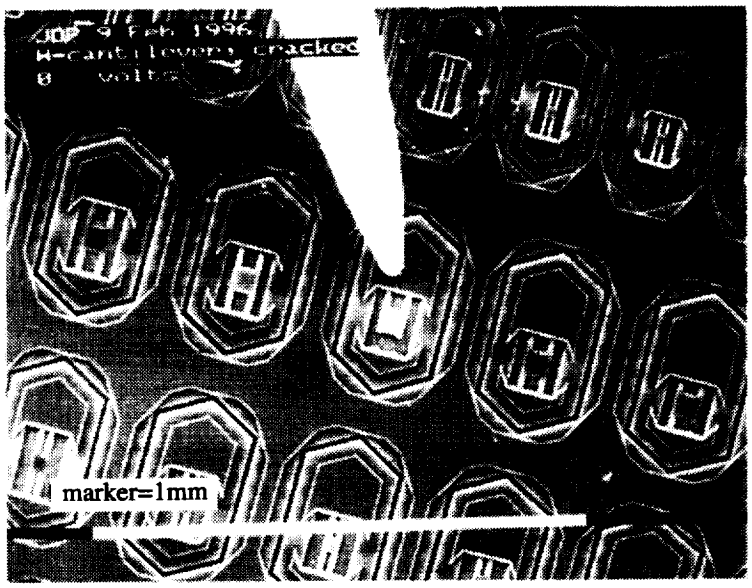

Figure 4-3. A SEM photo of the cantilever modulator without an applied bias.

without applied bias. Note the hexagonal electrical isolation trench delineating the structure. The extent of the probed cantilever including the isolation trench is 250 μm by 400 μm. Figure 4-4 shows the same cantilever but with 45 V of DC bias. The white or brighter regions indicate the area with a higher potential. Note that the hexagonal trench clearly electrically isolates the top mirror of the device from the top mirrors of adjacent Fabry-Perots. Also the bright top mirror or cantilever is shown to be electrically isolated from the darker Si well below. This indicates the required electrical isolation between the top and bottom mirrors.

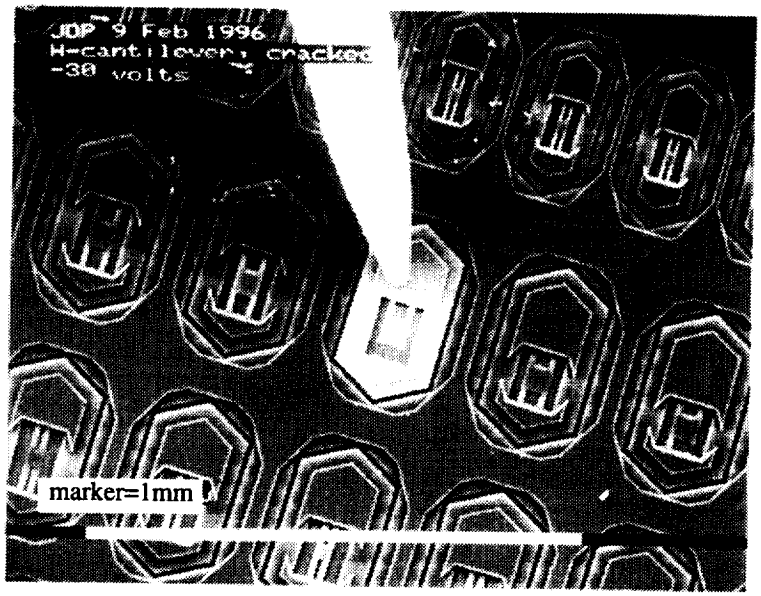

Figure 4-4. A SEM voltage contrast photo showing electrical isolation between the top and bottom mirrors of the contacted Fabry-Perot. The top mirror of the contacted device is also shown to be electrically isolated from the top mirrors of adjacent structures.

The movement of the cantilever as a function of applied DC bias was studied. The drive voltage was swept from 0 to 45 volts and then back to 0 volts. Figures 4-5 and 4-6 show SEM photos of the structure with 0 and 45 volts applied respectively.

Little movement of the cantilever was observed until the voltage reached 40 volts. At 40 volts the air gap at the tip of the cantilever was approximately 5 μm. The low sensitivity to voltage is expected since the cantilever force is proportional to the square of the ratio of the voltage to the air gap. At 45 volts the cantilever snapped down into contact with the Si indicating the threshold voltage effect predicted by the theory (at the threshold voltage a runaway condition exists in which the cantilever stiffness can no longer balance the electrostatic force).

Hysteresis was observed in the motion of the cantilever during the reverse voltage sweep. A reduction of the voltage to 12 volts was required to release the structure from the silicon. The hysteresis was predicted in the theoretical chapter and is consequence of the large electrostatic force present when the cantilever is in close proximity to the Si surface. However, as will be discussed in section 4.3 the hysteresis is experimentally shown to be avoidable, if the drive voltage is not allowed to exceed the threshold voltage V_{th}. The capability to operate the device without hysteresis was also predicted in the theoretical chapter.

Stiction was also observed when the cantilever was allowed to rest on the Si surface for more than a few seconds. That is, the cantilever was stuck and was not released at 12 Volts. Instead, the voltage had to be reduced further to release the structure. Stiction, as the name suggests, is the pinning of two structures together following contact. The pinning force is provided by short range intersolid forces between the two structures (Van der Waal forces). These are the same force which causes the pinning problem during the air drying which was discussed in the fabrication chapter. Stiction is a common problem with micro-mechanical structures which rely on contacted surfaces during operation. In the normal operation of the micro-mechanical Fabry-Perot the voltages would be maintained below the threshold voltage disallowing contact and preventing the stiction problem.

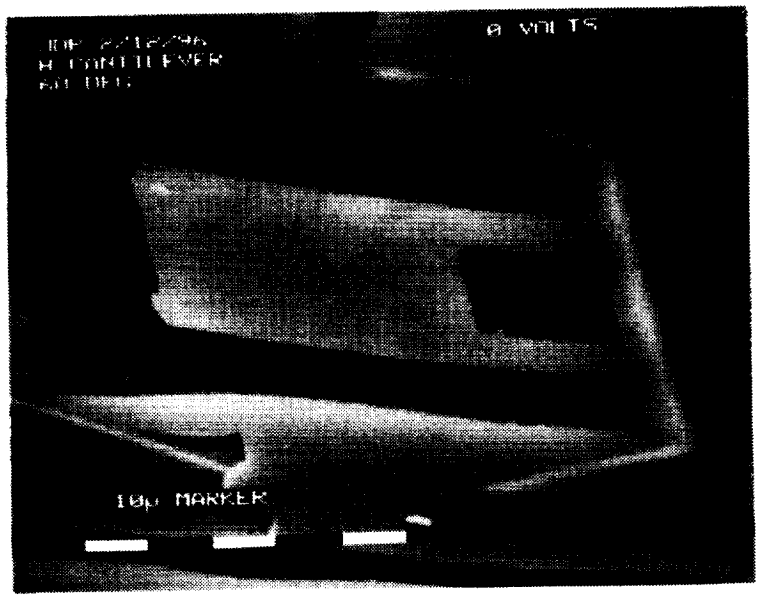

Figure 4-5. A SEM photo of the cantilever with 0 volts applied bias.

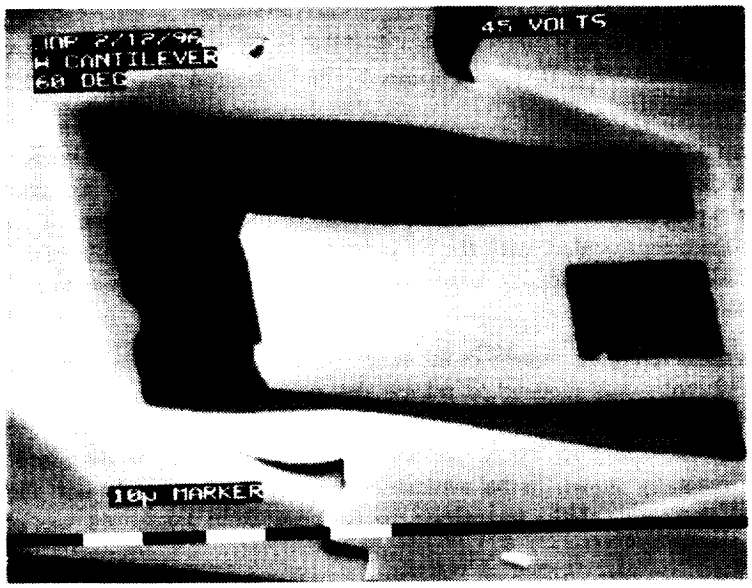

Figure 4-6. A SEM photo of the cantilever with 45 volts applied bias. The cantilever has been moved into contact with the silicon surface

Figure 4-7 shows the predicted displacement-voltage characteristic of the cantilever using the theoretical numerical model presented in Chapter II. As shown, the theoretical model is consistent with the experimental results. The model predicts the hysteresis and equivalent threshold and release voltages.

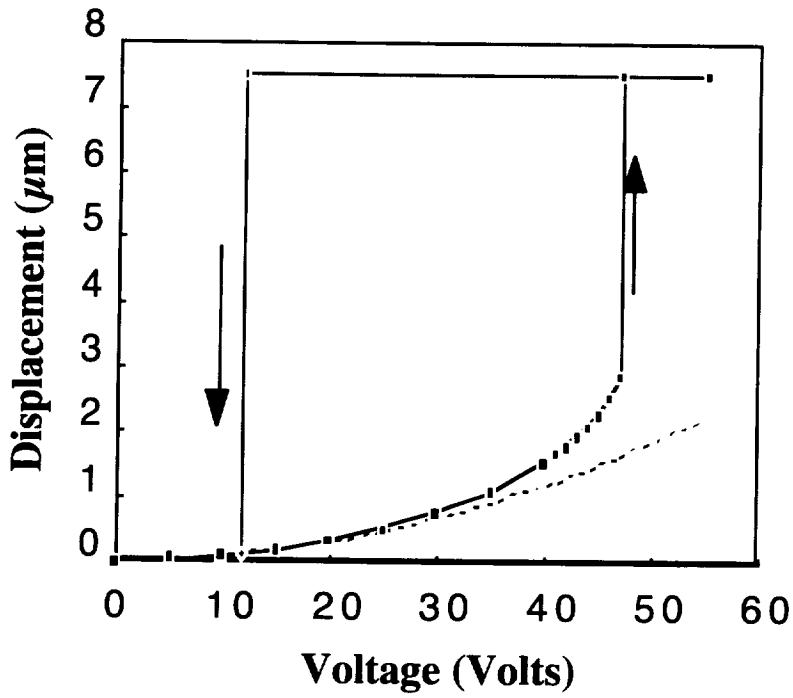

Figure 4-7. The predicted Displacement-Voltage characteristic for the cantilever structure studied in the SEM.

The resonant frequency of the cantilever structure was also observed using the SEM. The cantilever was driven with a 35 volt DC bias summed with a 10 volt peak-to-peak sinusoidal voltage. The resonant frequency of the cantilever was determined by observing the cantilever tip oscillation amplitude during the frequency sweep. Observation of the high frequency oscillations with the SEM video screen was made possible by scan triggering using the AC cantilever drive signal. The fundamental resonance frequency of the structure was observed to be approximately 40 KHz which is comparable with the theoretically predicted value of 42 KHz. Higher order resonances were also observed at 80 KHz and 120 KHz.

4.3 Electro-Optical Characterization: Wavelength Resolved

4.3.0 Introduction

In this section, the experimentally measured behavior of the micro-mechanical Fabry-Perots as tunable optical filters is presented. The behavior of the modulator filtering characteristics as a function of DC voltage is presented for two cases. In the first case, a cantilever modulator is spectrally analyzed using a tunable Ti-Sapphire laser source. The cantilever structure analyzed with the laser did not include a nickel layer on the bottom mirror. In the next case, a broadband LED is used as a source to spectrally characterize a cantilever Fabry-Perot filter including the nickel layer. The wavelength range for the spectral characterizations was 720–920 nm. This range is consistent with the high sensitivity region of a silicon photodetector which could potentially be integrated with the Fabry-Perot filter. Reflectance spectra were measured since the silicon substrate absorbs highly in this wavelength range preventing transmission spectra measurements.

The experimental arrangement used for all spectral characterizations is shown in Figure 4-8.

The light from the laser or LED is first collimated by a f = 25.4 mm lens and then focused onto the chip with an 8 mm focal length lens. A beam splitter is positioned between the lenses to direct the beam reflected by the Fabry-Perot chip to the spectrometer or to the CCD camera. All lenses were corrected for spherical aberration, coma, and astigmatism (Melles Griot multielement lenses 06 GLC 00# series). The

lenses were also antireflection coated for wavelengths ranging from 0.6 to 1 μm.

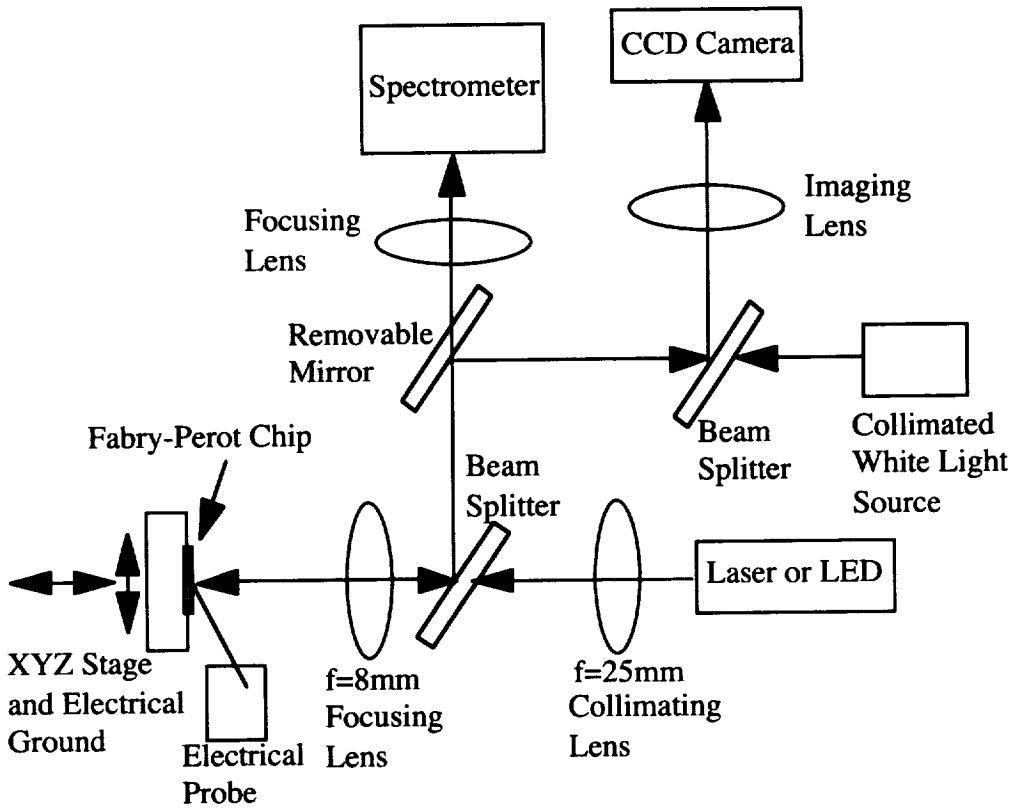

Figure 4-8. The experimental arrangement used to spectrally characterize the Fabry-Perot filters.

The drive voltage for the cantilever structures was applied by an electrical probe mounted onto a translation stage. The Fabry-Perot chip was mounted onto one-sided copper printed circuit board (PCB) that served as the electrical ground. The chip PCB combination was attached to a XYZ stage for focus optimization and cantilever selection. The glass-epoxy side of the PCB provided electrical isolation between the chip ground and the XYZ stage preventing ground loop problems.

Upon reflection from the Fabry-Perot cantilever structures, the reflected light is sampled with the beam splitter. From this point the light is either directed toward the CCD camera system for imaging or to the spectrometer. When the mirror is in place, an image of the chip is provided to the CCD camera. The camera system was used to view the sample during cantilever selection and beam focusing. Chip illumination was provided by a beam splitter coupled collimated white light source as shown.

Removal of the mirror permits the light to enter the spectrometer. The spectrometer used was an ORIEL Instaspec system with a 0.5 nm resolution. A 125 mm lens is used to focus the modulated light from the Fabry-Perot into the focal plane of the spectrometer.

4.3.1 Spectral Analysis of a Modulator Without Ni: Early Spectral Results

The first wavelength resolved reflectance characteristics were obtained on a Fabry-Perot which used the silicon-air interface as the bottom mirror rather than a metal mirror. The cantilever Fabry-Perot is shown in Figure 4-9. The length of the cantilever is a short 30 μm resulting in a very stiff structure. Longer and more voltage sensitive cantilevers were not analyzed on this chip since they were all pinned to the silicon (this chip was fabricated before CPD drying was used).

The reflection mode spectral characteristics of this structure were measured with a tunable Ti: Sapphire laser source. Figure 4-10 shows the reflected power plotted against wavelength for mirror voltages of 0, 30, and 40 volts.

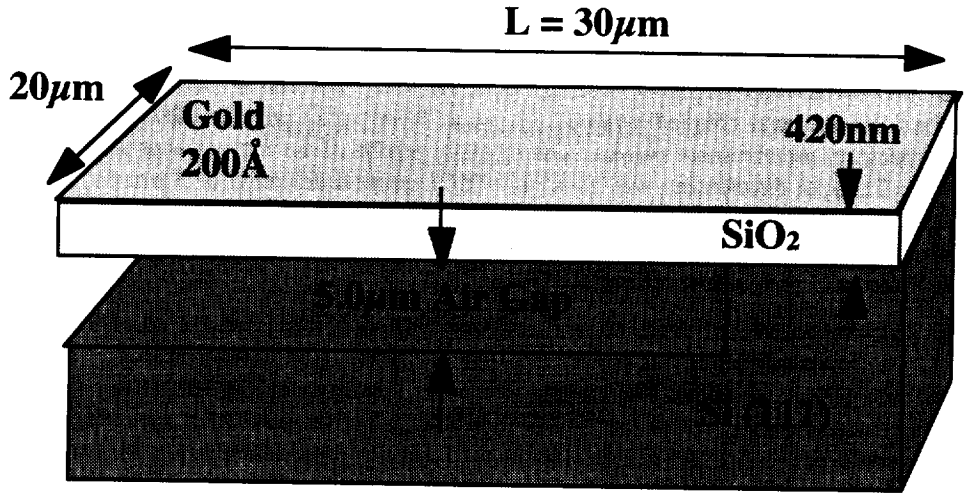

Figure 4-9. The cantilever structure which was spectrally analyzed with Ti:Sapphire laser. The length of the cantilever is a stiff 30 μm. The bottom mirror is not coated with nickel and provides only the 35% reflectivity of the bare silicon.

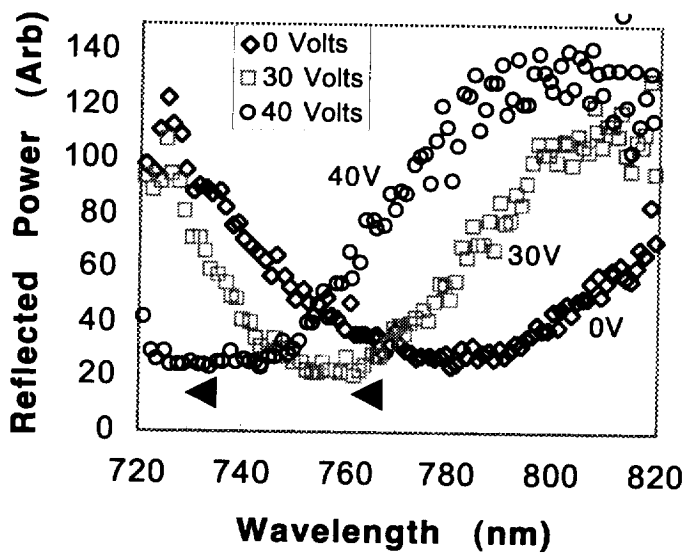

Figure 4-10. Fabry-Perot spectra taken at 0, 30, and 40 volts.

The reflected power is shown in arbitrary units and is normalized to the spectral distribution of the laser. The reflectance minima as predicted by the theory shift toward shorter wavelengths with increased voltage. An increase in voltage results in a shorter cavity and a smaller resonant wavelength. The filter provides 40 nm of wavelength tuning with a maximum of 40 volts applied bias. The small tuning range is mainly a consequence of the cantilever's short length. The linewidth of the reflection minimum is approximately 60 nm yielding a low finesse of 1.1. The low finesse is mainly due to the low 35% reflectivity of the silicon-

air interface.

4.3.2 Spectral Analysis of a Modulator Including the Ni Layer.

The spectral characteristics of a cantilever modulator including the higher reflectance nickel layer (67%) on the bottom mirror was measured. The light source used for the spectral characterization was a graded bandgap AlGaAs surface emitting LED. The LED spectral width was 100 nm FWHM and was centered at 850 nm. The LED light was coupled into a 62.5 μm core fiber pigtail providing 260 μW of power at the input of the spectrum measurement system. The intensity profile of the focused spot was measured with a beam scanner. The spot distribution was gaussian with a standard deviation of 5 μm (σ). Consequently, the spot diameter is 10 μm at a radius of one sigma. The spot is easily accommodated by the smallest 20 μm dimension of the cantilevers. The spectral measurements were normalized by the unamplified spectral distribution of the LED and are true reflectance spectra.

A cross-sectional diagram of the cantilever modulator spectrally characterized with the LED is shown in Figure 4-11. The oxide cantilever was coated with 200 Å of gold. The bottom mirror or silicon well was electroplated with 500 Å of nickel. The air gap under the cantilever at the supporting silicon wall was measured to be 3.2 μm with a Dektak profilometer. The length of the cantilever was 101 μm. The longer length of the cantilever provides for a more flexible top mirror in comparison to the 30 μm long cantilever analyzed with the Ti:Sapphire laser.

Spectra at voltages ranging from 0–53 V were measured for this structure. At 54 volts the cantilever structure reached its threshold voltage and snapped down into contact with the nickel surface. Hysteresis was observed during the reverse voltage sweep following contact. However, it was experimentally shown that if the applied voltage is constrained below the threshold voltage, then the hysteresis is avoided. That is, there is a one-to-one correspondence between voltage and spectra. The nonhysteretic behavior region was also predicted by the theory.

Spectra taken in the 40–50 volt range provided the highest spectral shift sensitivity to voltage, best finesse, best on/off ratio, and smallest linewidths. Figure 4-12 shows the reflectance spectra for this structure at 40, 44, and 48 volts. As shown the spectral width of the reflection minima is approximately 25 nm. This is a 35 nm improvement over the cantilever with a bare silicon bottom mirror which produced a 60 nm linewidth. The mode spacing for the nickel plated Fabry-Perot is approximately 60 nm yielding an improved finesse of 2.4. The finesse improvement is due to the increase in mirror reflectivity provided by the nickel layer. The on/off ratio is 1.5. The spectra, as predicted by the theory, blue shifts as the voltage is increased and the cavity length is reduced (this is indicated by the arrows in the Figure).

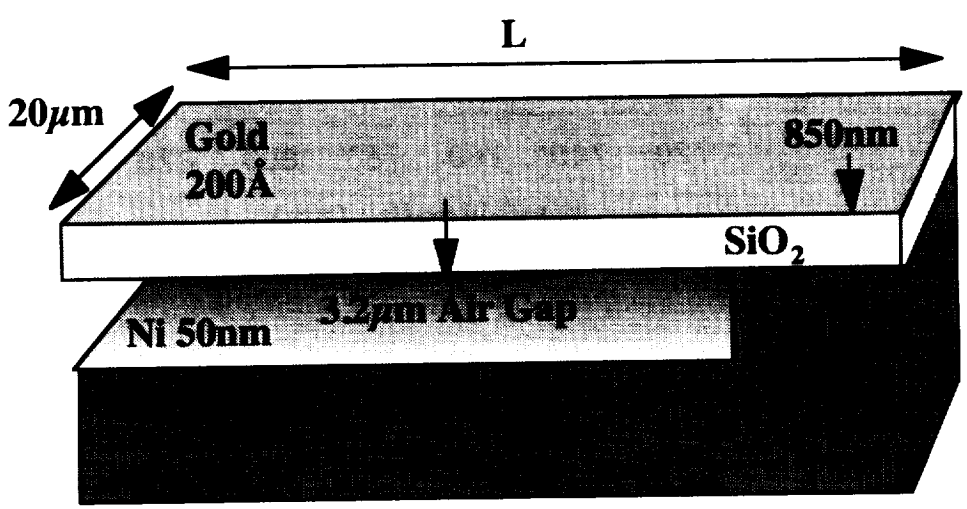

Figure 4-11. A cross-sectional diagram of a cantilever modulator with a nickel plated bottom mirror.

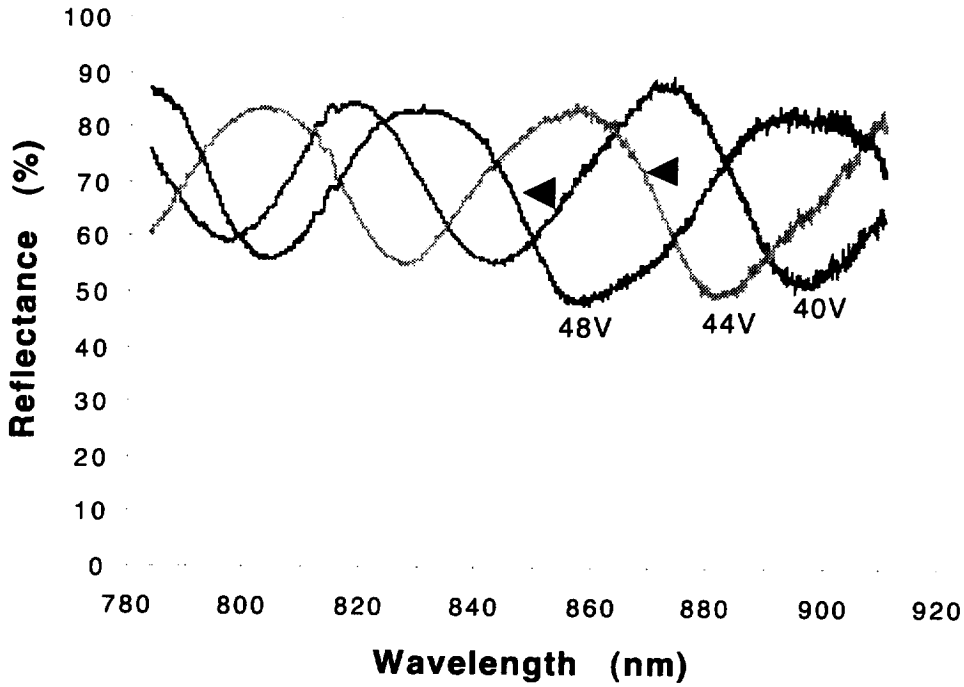

Figure 4-12. The Fabry-Perot spectra measured at 40, 44, and 48 volts applied bias.

Comparison between theoretical and experimentally measured spectra and threshold voltage has suggested that the air gap at the end of the cantilever is 6.27 μm instead of 3.2 μm. The wavelength position of the reflectance minima and the 53 volt threshold voltage are consistent with an air gap of 6.27 μm. The 3.2 μm depth as shown in Figure 4-11 was measured with the Dektak profilometer at the supporting silicon wall and not at the tip of the cantilever where the light beam is focused. Measurement of the cantilever tip height with the Dektak is impossible since the weight of the stylus would collapse the cantilever. The Dektak measurement is valid at the tip when the cantilever is straight. However, as mentioned in the fabrication chapter, the cantilevers curve upward resulting in an increased air gap at the tip (see Figure 3-33). The curvature was due to the high thermal stress between the silicon substrate and the silicon dioxide cantilever before undercutting.

Figure 4-13 shows a comparison between the measured and theoretical spectrum for the cantilever with a 40 volt applied bias. The calculated spectrum assumes ideal, flat and parallel, top and bottom mirrors and an air gap of 6.27 μm.

The measured reflectance wavelength minima are closely predicted by the theory. The maximum reflectance measured experimentally is 86% which is slightly lower but comparable to the calculated value of 92%. The lower experimental values are probably due to light scattering losses at the mirrors. On the other hand, the finesse, linewidth, and on/off ratio are much poorer than that predicted by the ideal Fabry-Perot theory. The theory predicts a finesse of 13, a linewidth of 4 nm, and an on/off ratio of 9. Reduced performance is most probably due to the stress induced curvature of the top mirror and the staircase profile of the bottom mirror. The staircase profile was discussed in the fabrication chapter and is a consequence of a misalignment of the wafer surface with respect to the (111) plane. The depth of the staircase has been shown to result in air gap variations ranging from 388–1700 Å underneath the cantilever as measured using the Dektak profilometer.

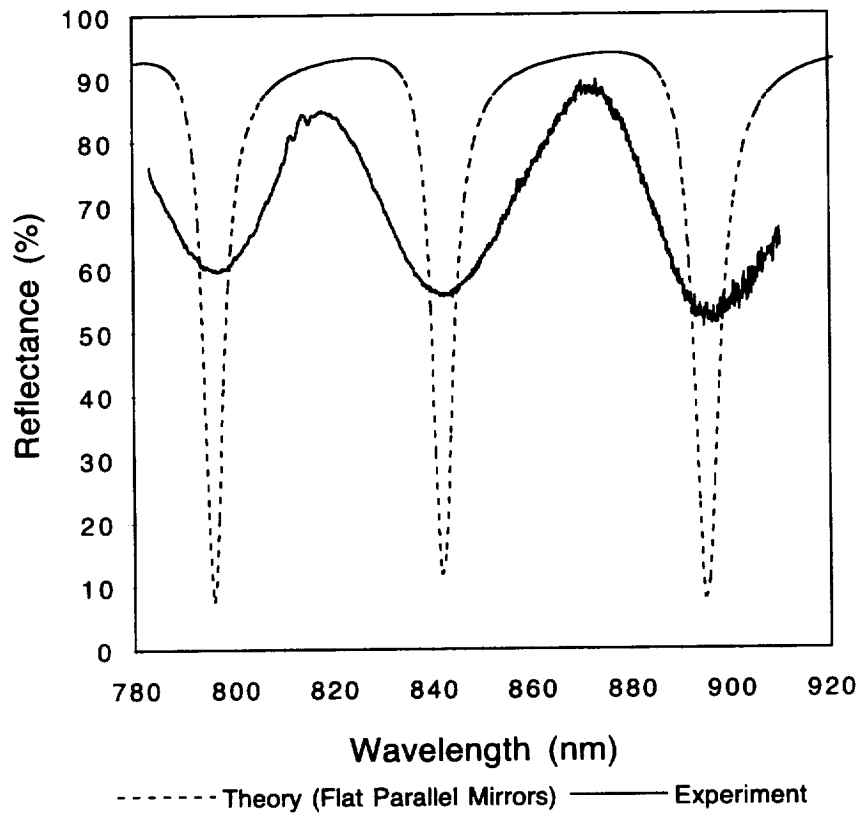

Figure 4-13. A comparison between the measured and calculated spectra for the Fabry-Perot at 40 volts applied bias. The calculated spectrum assumes ideal, flat and parallel, top and bottom mirrors.

The ideal Fabry-Perot optical theory predicts much better performance characteristics for our structure in comparison to those experimentally measured. A modification of the optical theory to include the effects of the nonideal curved top mirror and angled bottom mirror is required. The modified theory requires an estimate of the shape of the top and bottom mirror. We already have Dektak profiles of the bottom mirror indicating a flat sloped mirror with tilt angles ranging from 0.13° to 0.5°. In regard to the top mirror, we know that the cantilever curvature is much more pronounced along its length than its width. To simplify the analysis the curvature along the cantilever width is ignored. It is known based on the Dektak measurement that the air gap at the supported end of the cantilever is 3.2 μm. As mentioned previously, both the ideal optical and electromechanical theory suggests that the tip of the cantilever where the light beam is focused is 6.27 μm. above the bottom mirror. Furthermore the optical theory suggests that the air gap at the position of the light beam is 6.27 μm. During the measurements the center of the beam was positioned at 94 μm or 6 μm from the end of the cantilever. We now have two points to pass a profile curve through. It is assumed that the profile curve has the same fourth order polynomial dependence as in Equation 9 of Chapter 2. The shape is actually a superposition of a quadratic profile that results from the thermal stress [1] and a 4th order profile that results from the applied voltage. Figure 4-14 below shows the fitted fourth order polynomial profile of the cantilever. Qualitatively, the profile agrees with those shown in the SEM photos of Figures 3-33. In Figure 4-13 and the analysis, the angular misalignment of the bottom mirror is included. Later it will be shown that the performance degradation due to the relatively small angular misalignment of the bottom mirror is negligible in comparison to that of the top mirror. The top mirror has a calculated pitch angle of 2.5° at the tip while the staircase profile of the bottom mirror ranges from 0.1° to 0.5°. Here it is assumed that the bottom mirror has the worst case 0.5° misalignment which is the tolerance specified for the silicon wafers.

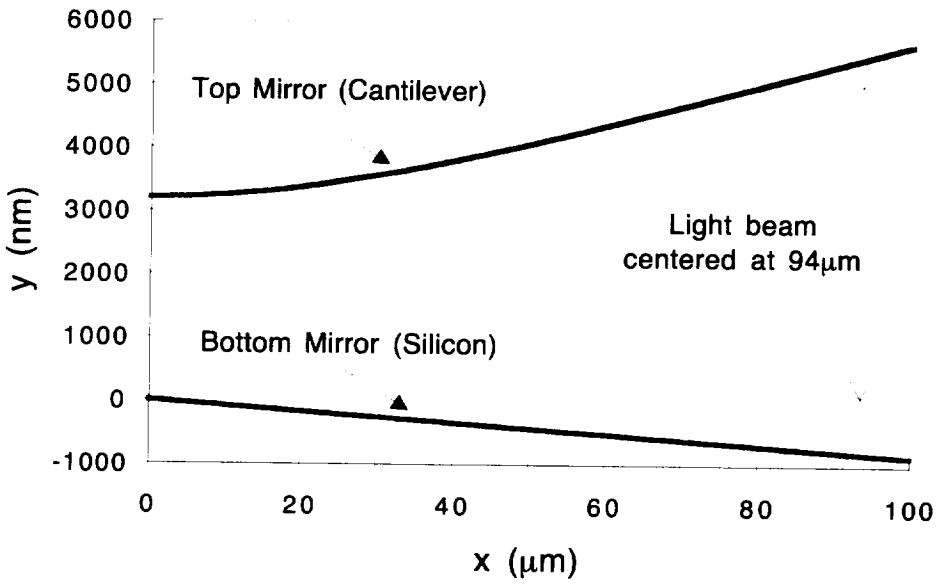

Figure 4-14. Mirror profiles for the Fabry-Perot. The 101 μm long cantilever is curving upwards due to stress damage. The bottom mirror is angled at -0.5° to represent the worst case staircase effect. The bias between the two mirrors is 40 volts.

A theoretical approximation of the spectra produced by the non ideal Fabry-Perot is to represent the two curved mirrors as a collection of ideal parallel mirror cavities with variable cavity length y(x). Here y(x) is the cavity length at position x. The spectrum produced by the collection of ideal cavities is the sum of each spectrum generated at position x weighted by the intensity profile of the illuminating light beam and an aperture function. The mathematical expression representing the theoretical calculation is given by:

$$R_{Curved\ Mirrors}(\lambda) = \frac{\sum_{Beam\ Extent} W(x_i) R_{Ideal}[\lambda, y(x_i)]}{\sum_{Beam\ Extent} W(x_i)} \tag{4-1}$$

Here $R_{Ideal}(\lambda, y(x_j))$ is the spectrum produced by a an ideal Fabry-Perot at position x_i. Each Fabry-Perot cavity is separated by the adjacent cavity by Δx which determines the spacing of the x_i and accuracy of the summation. The weighting function $W(x_i)$ is a product of the focused light beams intensity distribution and an aperture function.

$$W(x_i) = I(x_i) A(x_i) \tag{4-2}$$

The intensity distribution, $I(x_i)$ as mentioned previously, was measured with a beam scanner. The intensity profile is shown in Figure 4-15. The profile was fitted using a gaussian function with a σ of 5 μm.

The aperture function, $A(x_i)$ is an additional weighting factor on the gaussian. It either carries the value of zero or one. The physical source of the aperture function is the entrance slit of the Oriel spectrometer which is the first image plane for the gaussian. The entrance slit was 100 μm wide during the spectral measurements. Projecting an image of the entrance slit into the plane of the cantilever results in a demagnification of the slit to 5.0 μm. Consequently the aperture function for the gaussian in Figure 4-15 is 1 for $-2.5\ \mu m < x < 2.5\ \mu m$ and zero outside this range. The summation over the weighting factors in Equation 4-1 above provides the normalization.

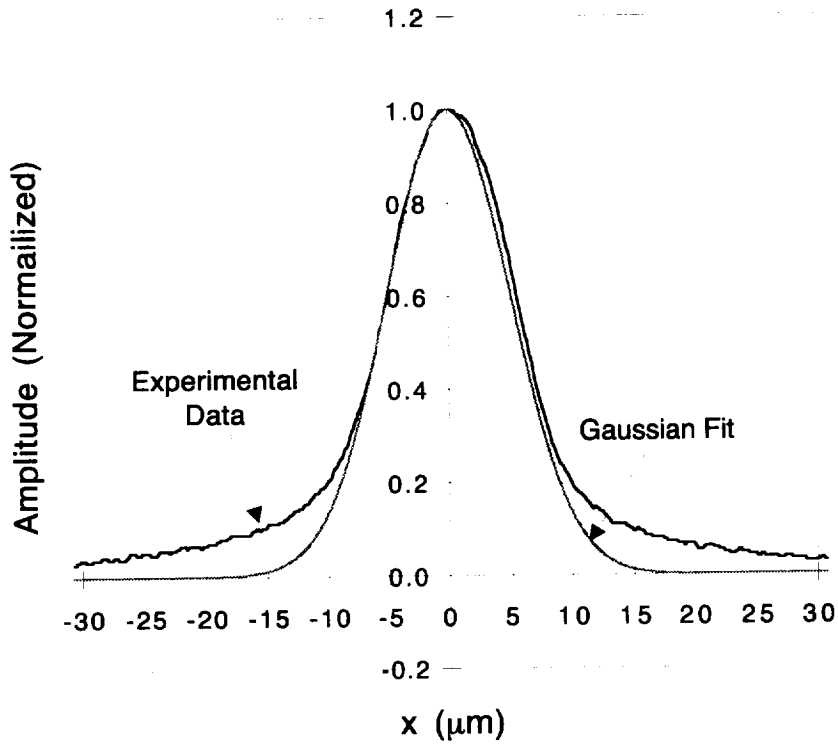

Figure 4-15. The measured intensity profile of the focused LED light beam on the top mirror. The profile is fitted with a $\sigma = 5\ \mu m$ gaussian function. The gaussian function is used to weight the spectra in the summation.

A few statements regarding the expected validity of the modified theory is due. The weighted sum approximation is more valid for low finesse. Our measured finesse is only 2.4 indicating that on average the light in the cavity exits or no longer contributes interferometrically after 2.4 round trips. The low number of round trips and small mirror angles ensure that beam walkout effects are not significant. Another concern is the validity of the plane wave approximation of the wavefronts. Consider the confocal beam parameter which gives the range over which the beam expands by factor of the square root of two from its minimum waiste position [2].

$$z_o = \frac{\pi \omega_o^2 n}{\lambda}$$

$$\omega_o \rightarrow \textit{minimum waist diameter}$$

$$n \rightarrow \textit{refractive index inside cavity}$$

$$\lambda \rightarrow \textit{wavelength} \tag{4-3}$$

The confocal length corresponding to a sigma of 5 μm is 185 μm at 850 nm wavelength whereas the path corresponding to the photon lifetime is a much small 15 μm (2.4 round trips in the cavity). Consequently beam divergence should be a relatively small correction to our modified theory .

Figure 4-16 shows the spectra calculated for the 101μm long cantilever using the spectral summation approximation for the case of gaussian beam illumination. The mirror profiles shown in Figure 4-14 were used. The summation was taken over Fabry-Perots spaced every 0.5 μm in the x direction. The gaussian was apertured with a 5 μm diameter iris. The theory shows that as the light beam spot size increases, the finesse and on/off ratio decrease while the linewidth increases. These trends are consistent with our experimental results. A larger spot size samples a larger range of cavity lengths resulting in poorer filter

performance.

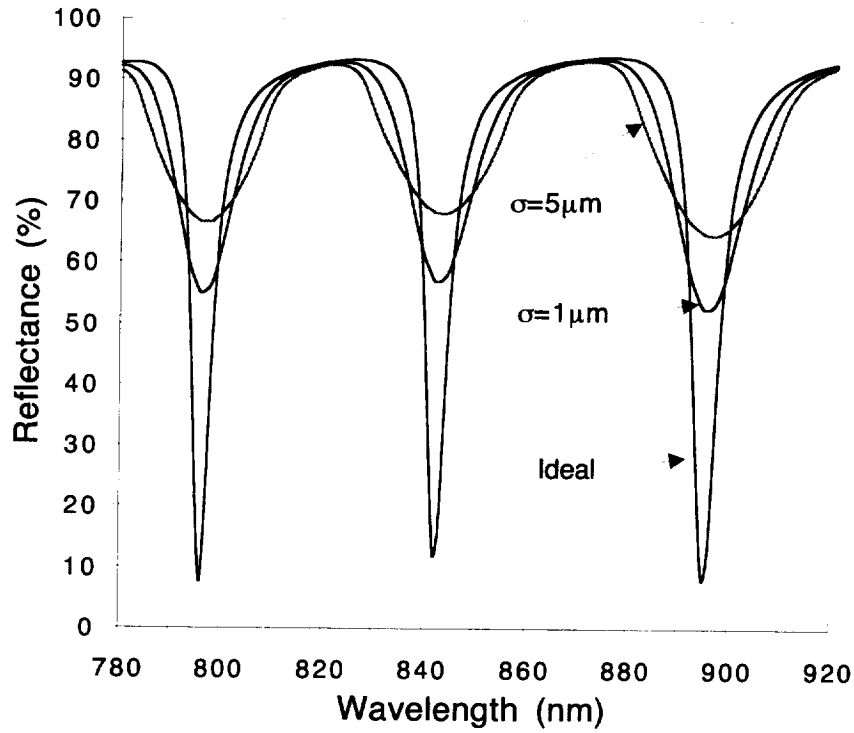

Figure 4-16. Reflectance as a function of wavelength for various spot sizes. Here the spectral summation approximation was used to calculate the total reflectance. The mirror profiles are those from Figure 4-14.

Figure 4-17 shows a comparison between the experimental and the theoretically calculated spectra for our nonideal Fabry-Perot shown in Figure 4-14. σ was the measured 5 μm. The spectral summation closely matches the experimental spectrum. Note that the finesse, linewidth, and on/off ratio predicted by the theoretical summation closely predicts the experimental values. The theory predicts a finesse of 2.7 and a linewidth of 22 nm which is close to the experimental values of 2.4 and 25 nm respectively. The maximum reflectance from the theoretical calculation is around 92% while the experimental value is a slightly lower 86%. As previously mentioned light scattering losses at the mirrors could be the culprit for the loss. The on/off ratio predicted by the theoretical summation is 1.4 whereas the experimental value is a comparable 1.5. In general the shape of the calculated spectrum is comparable to the experimentally measured spectrum except for the sharper or narrower peaks of the experimental data.

We have just established through theoretical corroboration that the curved top mirror and angled bottom mirror are the performance loss culprits of the micro-mechanical Fabry-Perot filter. One further question to be answered to facilitate efforts of future work is which of the two mirrors dominates the performance loss. Figure 4-18 below shows the calculated spectra for the Fabry-Perot when both the curvature of the top mirror and angled bottom mirror are included, and for the case in which the top mirror curvature alone is considered. There is only a slight difference between the two spectra. This indicates that the performance degradation due to the staircase profile of the bottom mirror is negligible in comparison to that caused by the stress induced curvature of the top mirror.

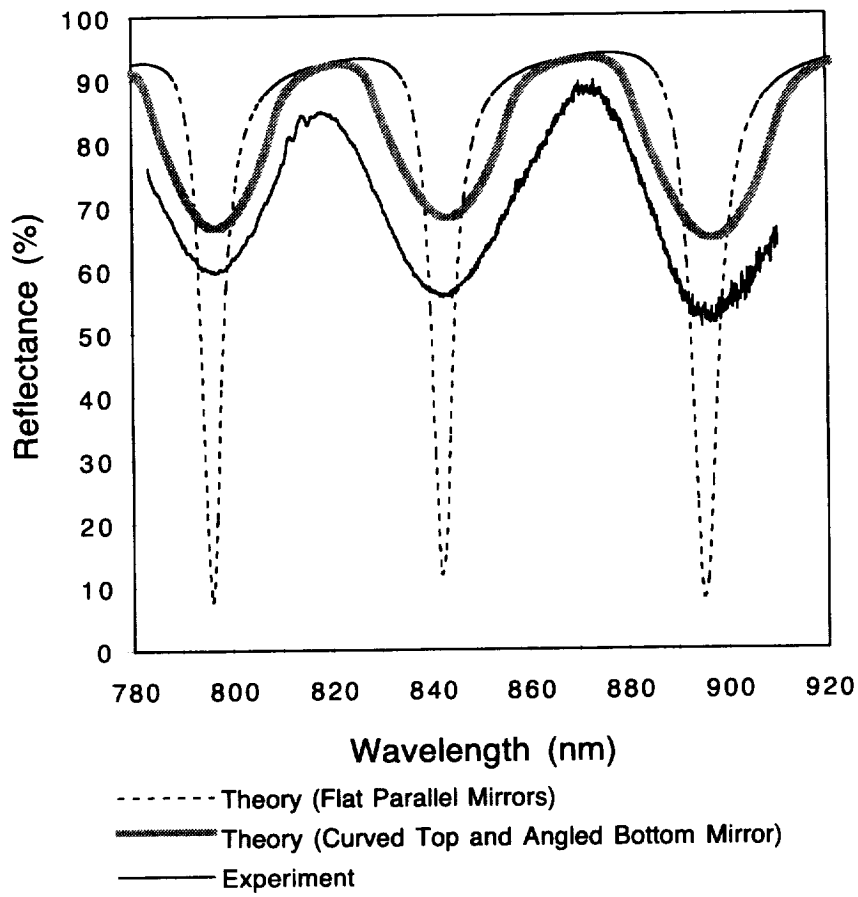

Figure 4-17. Experimental and theoretical spectra for the 101 μm long cantilever. The non ideal Fabry Perot theoretical spectrum was calculated using the summation approximation.

Figure 4-19 shows the wavelength tuning behavior of one cavity mode (8 wavelengths or m = 16) as a function of applied voltage. The diamond data points are the measured data points. The dashed lines represents the quadratic approximation of the resonant wavelength using :

$$\lambda(V) = \frac{2}{m}\left\{ n_{SiO_2} h_{ox} + h_{co} - \frac{3}{4}\frac{\varepsilon_o}{E h_{ox}^3}\frac{V^2}{\left[h_{co} + \frac{h_{ox}}{\varepsilon_{rox}}\right]^2} L^4 \right\} \tag{4-4}$$

The solid line represents the numerical solution.

Regarding the experimental data, the reflectance minima or transmission peak varies quadratically with voltage. Beyond 53 volts the cantilever snaps down into contact with the nickel due to the threshold voltage effect. The wavelength tuning range of this structure is 120 nm with 0-53 volts. As predicted by the theory, the wavelength tuning sensitivity of the more flexible 101 μm long cantilever is higher than the 30 μm long cantilever analyzed with the Ti:Sapphire laser (40 nm: 40 V). Analytic solutions are plotted for oxide elasticity moduli of 7.3×10^{10} Nm^2 and 5.0×10^{10} Nm^2. As shown by the theoretical curves the reported value of 7.3×10^{10} Nm^2 for fused silica results in an underestimate in the wavelength shift. A reduction of the elasticity modulus to 5.0×10^{10} Nm^2 results in closer agreement with the measured data.

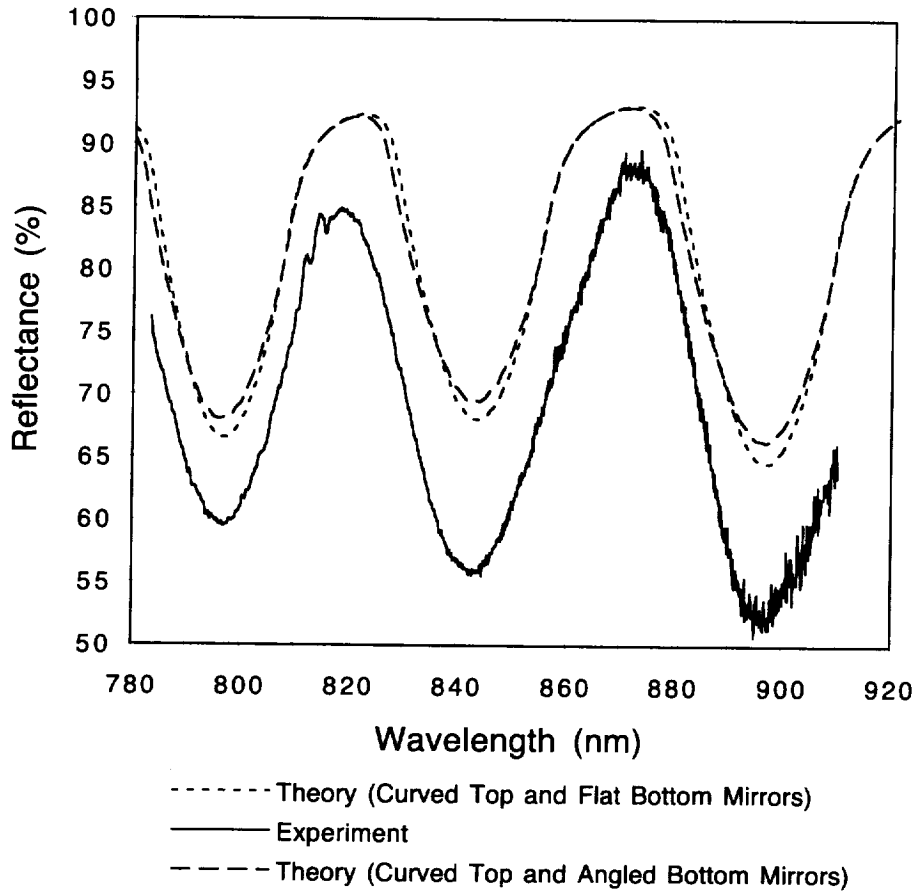

Figure 4-18. Experimental and theoretical spectra for the 101 μm long cantilever. The theoretical spectra were calculated using the weighted spectral summation. The dashed curves represent the theoretical spectra. The finesse degradation due to the top mirror curvature is dominant.

The experimental results presented in the next section for the time resolved response characteristics also suggest an elasticity modulus of 5.0×10^{10} Nm^2. It is reasonable to expect a smaller elasticity for our grown wet oxides in comparison to fused silica or dry oxide. Wet oxides exhibit lower densities than dry oxide or fused silica. A lower density results in a smaller number of springs per unit volume and a smaller electronic binding force between atoms (decreased stiffness) . K. E. Petersen has shown in earlier work with cantilever structures a measured elasticity modulus for a wet oxide of 5.7×10^{10} Nm^2 and 6.9×10^{10} Nm^2 for a dry oxide [3]. He reports an accuracy of +/- 20%. Our measured value of 5.0×10^{10} Nm^2 is within the bounds of his accuracy and consistent with his results. Figure 4-20 shows the behavior of the on/off ratio as a function of applied voltage. The ratio increases from a value of 1.26 at 0 volts to a value of 1.5 at 40 volts where it saturates. This behavior is most probably due to the lack of mirror parallelism at 0 volts. At zero volts the cantilever tip is bending upward due to stress induced curvature. An increase in voltage would bring the tip of the cantilever down into better parallelism with the Ni layer below providing for a more stable optical resonator (the light beam is focused on the tip of the cantilever). Consequently, the on/off ratio is improved.

The repeatability of the filter tuning characteristic was studied. One concern was the potential changes in the shape and elasticity of the cantilevers following the application of a voltage higher than the threshold voltage. Beyond the threshold voltage the cantilever snaps down into full contact with the nickel/silicon surface. The large attractive force provided by the high voltage could result in the plastic deformation of the cantilever and possibly stiction. Stiction, as mentioned earlier, is a common problem with micro-machined

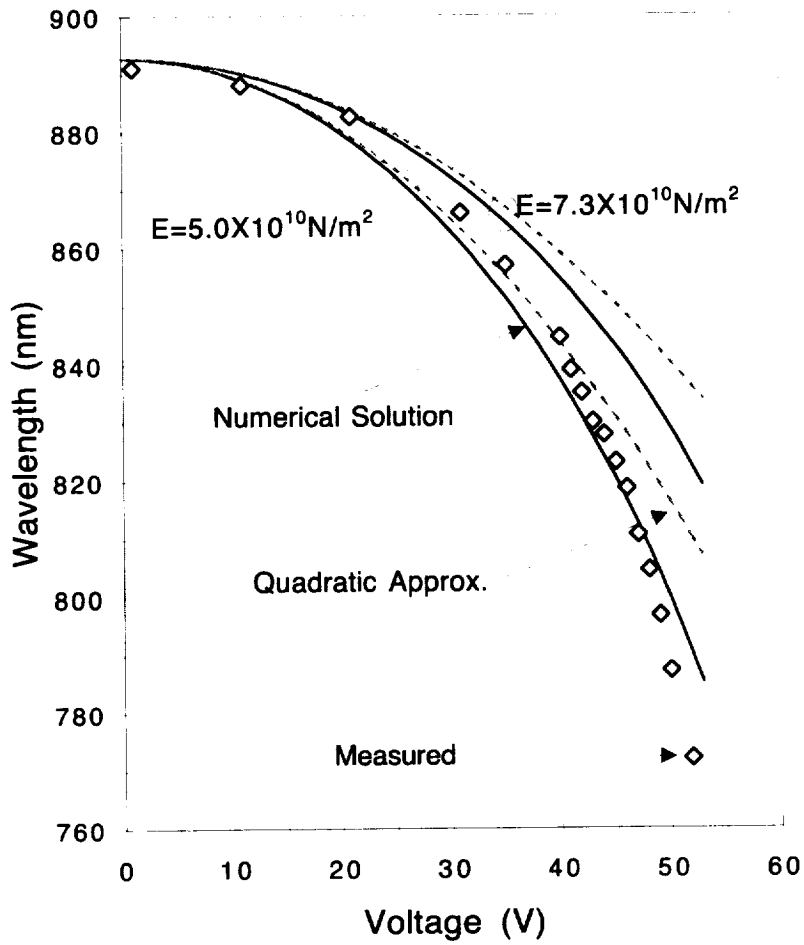

Figure 4-19. Minimum reflectance wavelength for one cavity mode as a function of applied DC voltage. The theoretical predictions using 5.0 X 10^{10} N/m^2 for the oxide elasticity modulus closely match the experimentally measured values.

structures. Stiction refers to the sticking of the cantilever to the substrate due to intersolid forces. The sticking force is higher with increased contact area. Large contact area between two structures is provided when their surfaces are maximally smooth as in the case of two smooth Fabry-Perot mirrors.

Figure 4-21 illustrates the repeatability of the cantilever spectrum. A spectrum was measured at 40 volts bias before the cantilever was pushed beyond the threshold voltage. A second spectrum also measured at 40 V bias is shown. This spectrum was taken following 10 voltage cycles. During each cycle the cantilever was snapped down into contact with the nickel at the threshold voltage and then released during the reverse sweep (0 to 54 to 0 volt cycle).

As shown the spectrum is repeatable and shows no measurable wavelength shift. This suggest that the stress forces are not sufficient to plastically deform the cantilever. Some stiction was observed on this device but not permanent sticking. The threshold voltage remained constant at 54 V over the 10 cycles.. However, the release voltage decreased from 13 V to 5 V over the 10 cycles. The reduction in release voltage for the structure is believed to be due to the increased conformality of the cantilever oxide surface to the nickel surface during the contact cycling. The increased contact surface area would result in greater stiction forces and consequently a lower release voltage.

The effects of the continuous oscillation of the cantilever on spectral repeatability was also studied. A 41 V DC bias in series with a 5 V peak-to-peak AC signal at 10 KHz was applied to the 101 μm long

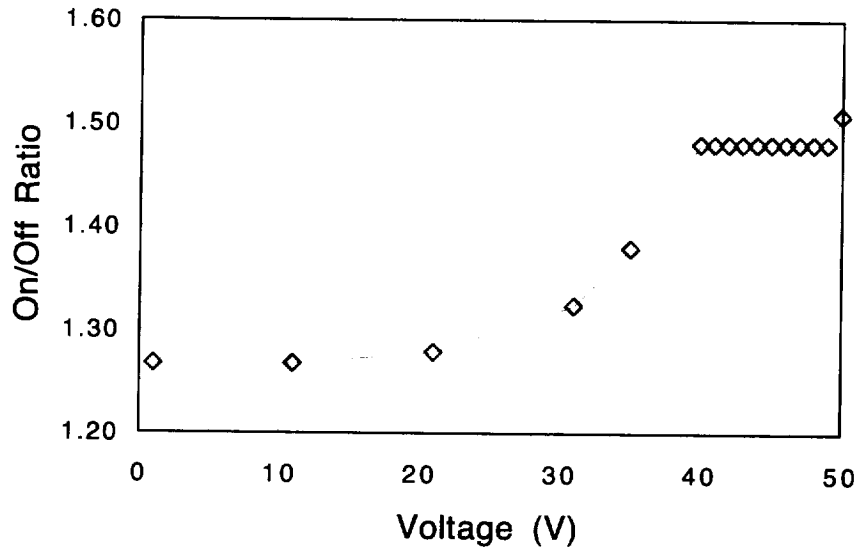

Figure 4-20. On/Off ratio versus voltage for the cantilever Fabry-Perot.

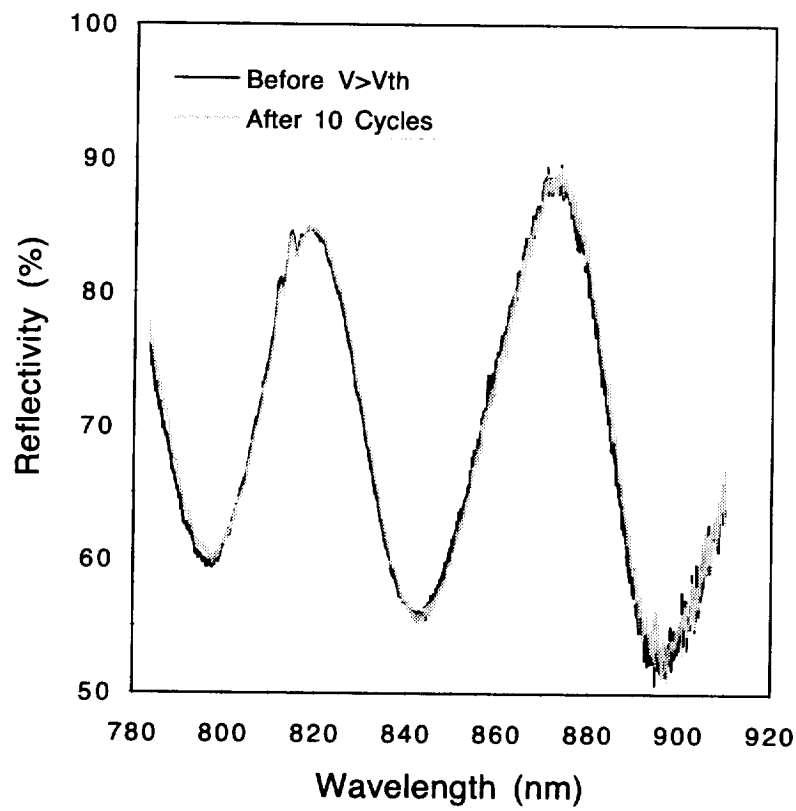

Figure 4-21. Repeatability of the cantilever Fabry-Perot spectra before and after cycling the cantilever from 0 to 54 volts and back ten times. Both spectra were measured at 40 V applied bias. Significant changes in the spectrum were not observed.

cantilever Fabry-Perot. The signal was applied for 8 hours. Spectra were taken at 41 V before and after the 8 hour period. Figure 4-22 shows the spectra.

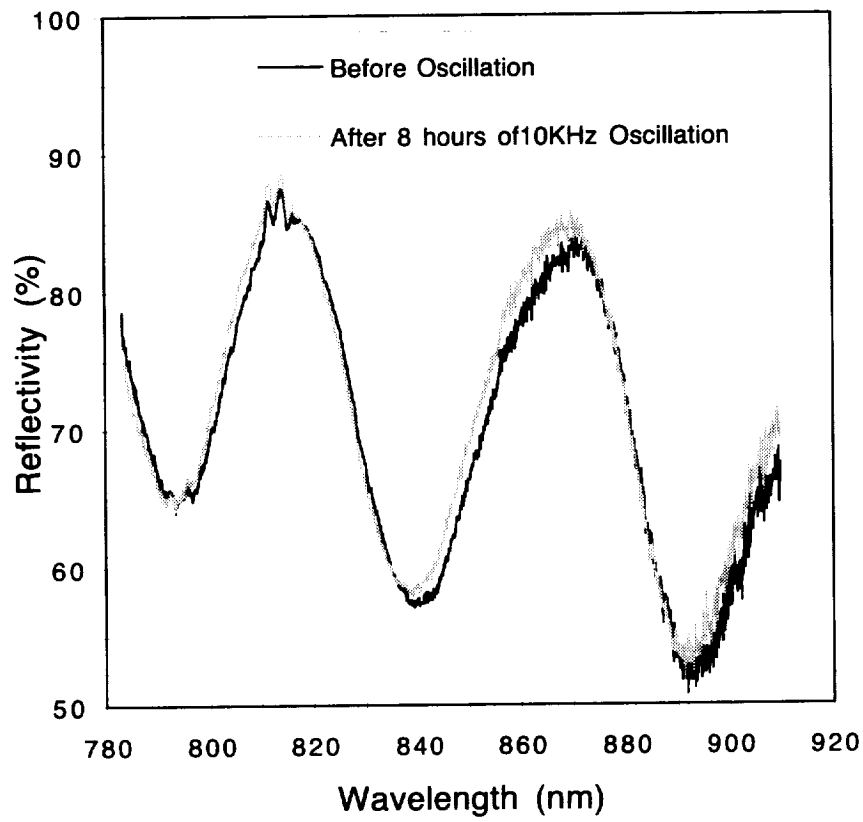

Figure 4-22. Spectrum repeatability before and after 8 hours of oscillation at a 10 KHz drive frequency. The applied voltage consisted of a 41 V DC bias in series with a 5 V peak-to-peak sinusoidal signal.

The spectra do not exhibit a significant change in reflectance and indicate good repeatability. The average magnitude change in the reflectance was 1.6 % with a maximum change in reflectance of 5.5%.

4.4 Electro-Optical Characterization: Time Resolved

The characteristics of the cantilever Fabry-Perots as intensity modulators were studied. The intensity modulation was characterized as function of drive frequency. Cantilever modulators as shown in Figure 4-11 above were studied with lengths ranging from 60 to 101 μm. The measurement arrangement shown in Figure 4-8 was used for the characterization. A fiber pigtailed 830 nm single mode laser was used as the optical source. An optical isolator was added in line with the laser to prevent optical feedback problems. The laser spot was focused on the cantilever tips to provide maximum intensity modulation. Detection of the modulated optical power was provided with a silicon PIN photodetector with a 125 MHz bandwidth. In Figure 4-8, the photodetector was placed in the position of the spectrometer.

The voltage applied to the cantilevers consisted of a small sinusoidal voltage (AC peak-to-peak voltage < 5 V) in series with a DC bias. An illustration of the biasing scheme is shown in Figure 4-23. The DC bias was necessary to blue shift the reflectance curve to a linear monotonic region relative to the laser wavelength.

Here the reflectance curve is DC biased to shift the reflectance spectrum from a peak at 830 nm to the midpoint in the reflection minima. At the midpoint the slope and modulation sensitivity is highest. Additionally, the midpoint ensures maximum cantilever deflection without nonlinearities. The small AC voltage then modulates the reflectance curve about the DC bias point yielding linear modulation of the laser light intensity. The DC biases were kept below the cantilever's threshold voltage. Additionally, the sums of

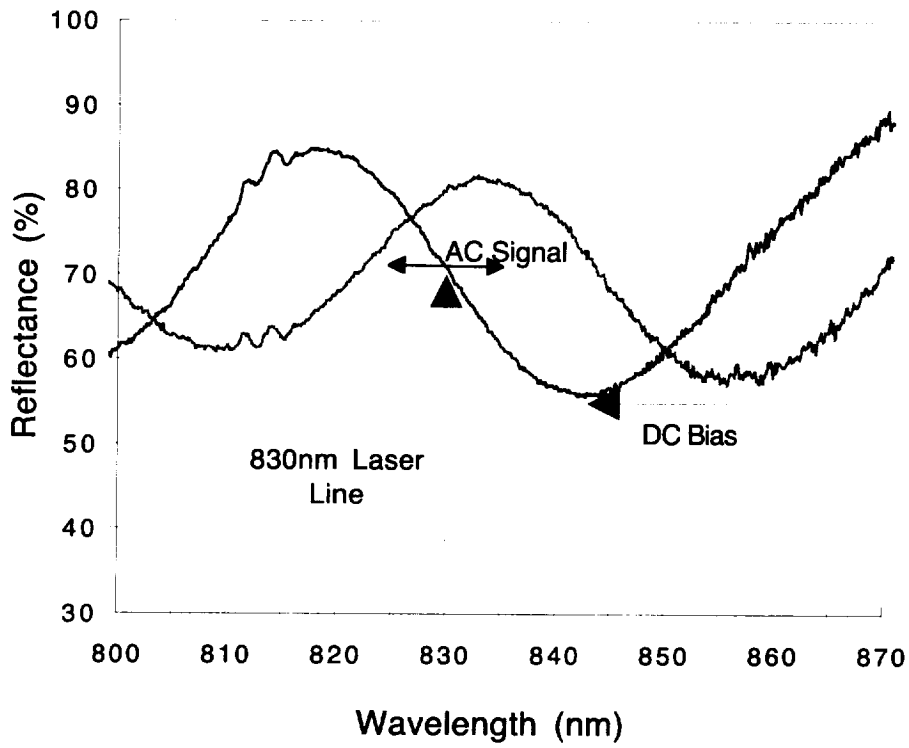

Figure 4-23. An illustration of the biasing scheme used in the time resolved measurements.

the DC and AC voltage were chosen so that the reflectance minima did not move relative to the laser line into and beyond its maxima and minimas during the AC cycle. This ensured an intensity modulation frequency equal to the AC signal frequency and linear modulation.

Figure 4-24 shows the photodetector output voltage versus time for the L = 101 μm cantilever Fabry-Perot modulated at 10 KHz.

The photodetector output frequency matches the cantilever AC drive frequency. The on/off ratio of the filter is approximately 2 and is defined as Vmax/Vmin.

Figure 4-25 shows the optical power as a function of time for the same L = 101 μm cantilever driven near at its fundamental resonant frequency of 57 KHz. The photodetector signal frequency no longer matches the cantilever drive signal frequency. Instead nonlinear modulation has occurred. For all other measurements presented, the AC voltage was reduced to avoid the nonlinearities. During this measurement the sum of the AC and DC voltages were high enough to result in nonlinearities at resonance. The existence of the higher frequency components and distortion is due to the large variation of the air gap at resonance. The large deflections result in modulation in the nonlinear regions of the reflectance curve. Another possibility is multiple reflectance minima and maxima passing through the 830 nm laser line per AC cycle. Note that the optical power envelope frequency still matches the drive voltage frequency.

Figures 4-26 and 4-27 show the frequency response of the optical power modulation for cantilevers of length 101 μm and 45 μm respectively. The response is defined as the peak-to-peak amplitude of the photodetector voltage ($v_{max}-v_{min}$ as shown in Figure 4-24 above) and is normalized to the DC response. The frequency response is relatively flat from DC to the fundamental resonant frequency for all three cantilevers. At the fundamental resonance the response peaks and then quickly rolls off toward zero. Contributions to the response characteristic from higher order resonances were not evident from the measurements as they were in the SEM study. The reduced effect of the higher order resonances during these measurements is due to viscous air damping which is not present in the vacuum of the SEM chamber. The longest and most flexible cantilever (L = 101 μm), as predicted by the theory, provided the smallest

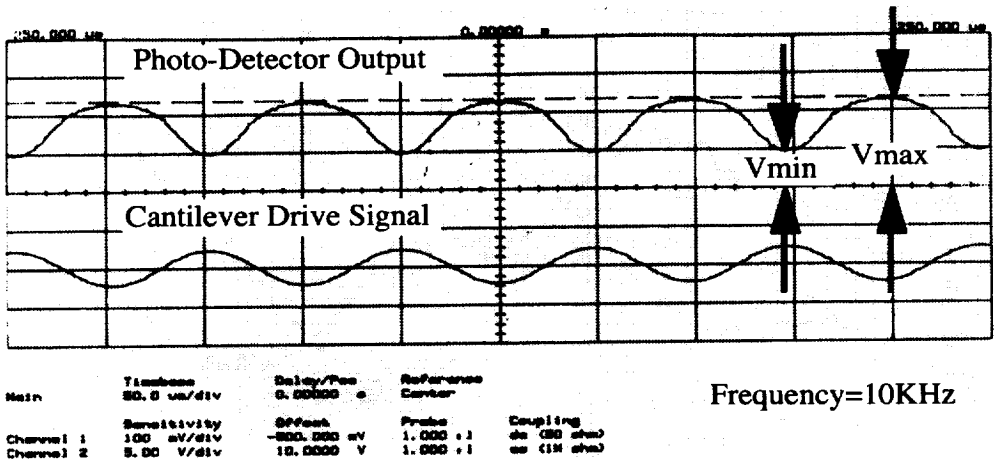

Figure 4-24. Modulation of 830 nm laser light by a cantilever modulator driven at 10 KHz. The DC bias was 21 V.

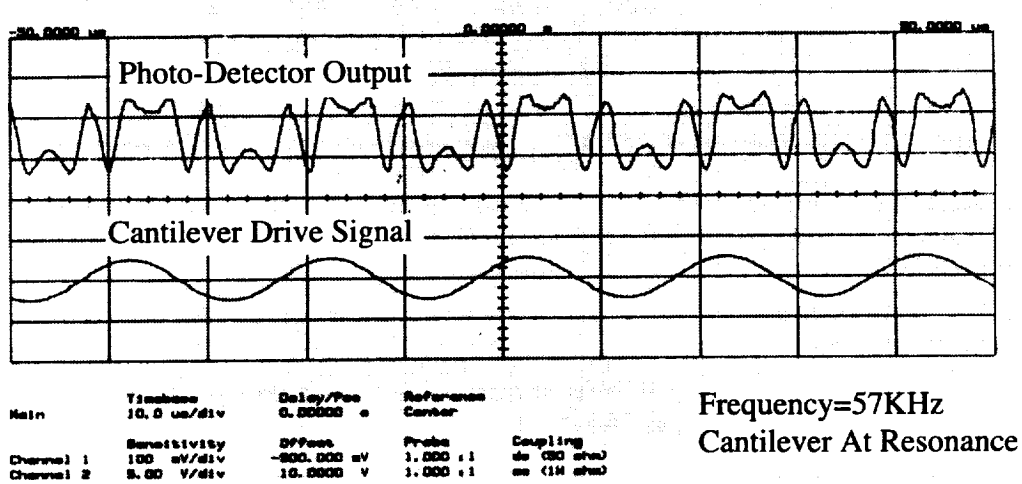

Figure 4-25. Modulation of 830 nm laser light by a cantilever modulator driven at its fundamental resonant frequency of 57 KHz. Note the higher order frequency components in the photodetector signal due to the large cantilever deflection.

bandwidth of 91 KHz (resonant frequency = 57 KHz) while the shorter and stiffer cantilever (L= 45 μm) exhibited a much higher 360 KHz bandwidth (resonant frequency = 262 KHz). The solid line in the graphs represents the theoretical prediction to the response characteristics. The theory presented in section 2.2 was used. An oxide elasticity modulus of 5.0 X 10^{10} N/m^2 was assumed since this value agrees with the measured resonant frequencies.

Damping factors of 1.35 × 10^{-7} kg/sec and 1.95 × 10^{-7} kg/sec were used to fit the amplitude at resonance for the 101 μm and 45 μm long cantilevers respectively. The larger damping factor for the shorter cantilever could be due to its smaller air gap: a longer cantilever bends further upwards due to stress. The smaller air gap of the short cantilever results in increased air compression resistance during the downward motion of the cantilever. Using the assumed values of elasticity and damping factor, the theoretical curves agree closely with the experimental values.

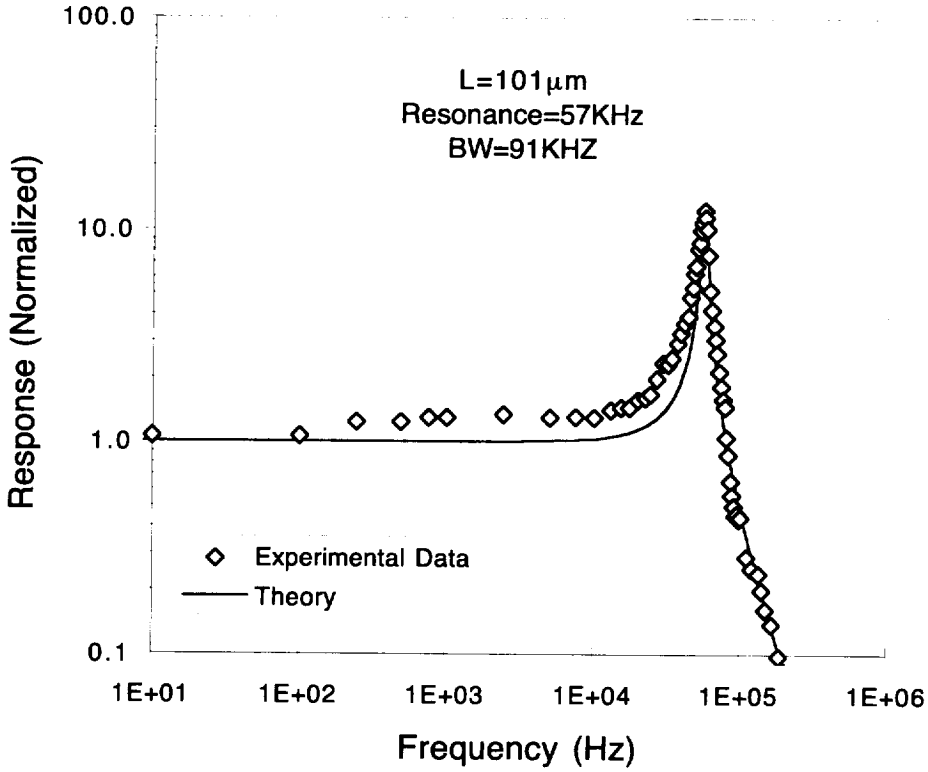

Figure 4-26. Frequency response of a cantilever modulator with a length of 101 μm.

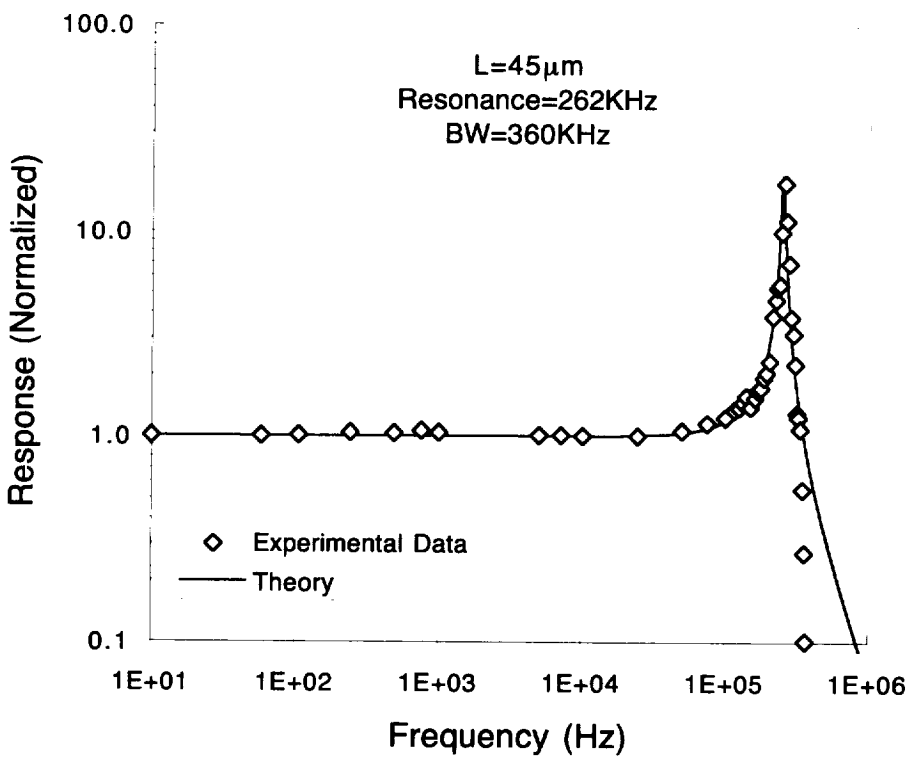

Figure 4-27. Frequency response of a cantilever modulator with a length of 45 μm.

A graphical comparison between the experimentally measured and theoretically calculated bandwidth and resonant frequency as function of cantilever length is shown in Figure 4-28. In the theoretical calculations a value of 5.0×10^{10} N/m^2 was used for the elasticity modulus. The experimental values for the resonant frequency ranged from 57 KHz for the longest cantilever (L = 101 μm) and 920 KHz for the shortest cantilever (L = 22 μm). The experimental values for the resonant frequency exhibit a $1/L^2$ dependence and show excellent agreement with the theoretical curve. For cantilevers with lengths ranging from 45 μm to 101 μm the relative error between predicted and experimental values was within 6%. The measured -3 dB bandwidths ranged from 91 KHz for the 101μm long cantilever and to more than 920 KHz for the 22 μm long cantilever. The -3 dB frequency for the latter structure could not measured due to the limiting 1 MHz bandwidth of the AC signal function generator. Agreement between the measured and theoretically predicted bandwidth is good (within 10%) for cantilevers of lengths ranging from 60 μm to 101 μm. For the 45 μm long cantilever the percent error was a relatively was 33%. The larger error may be due to limitations of the theoretical model when applied to the shorter structures.

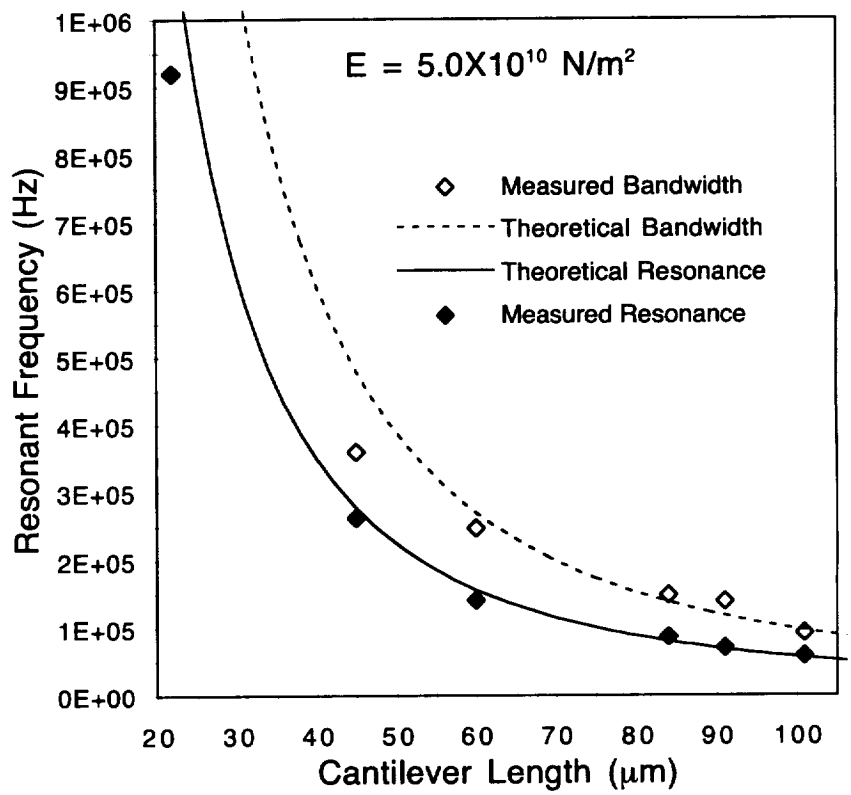

Figure 4-28. Bandwidth and resonant frequency versus cantilever length. The calculated values are shown by the lines and the experimental values by the diamonds. The elasticity modulus used in the theoretical curves was 5.0×10^{10} N/m^2.

The graph of Figure 4-28 is also shown in Figure 4-29. Here the same experimental data for the resonance frequency and bandwidth appears. However, the theoretical curves are now plotted using the reported value of the elasticity modulus for fused silica (7.3×10^{10} N/m^2). The theoretical curves predict significantly higher bandwidths and resonant frequencies in comparison with the experimental values. Relative errors ranging from 16 to 54% occur between the measured and predicted values for the resonant frequency. The large discrepancies between theory and experiment using the elasticity modulus of fused silica suggest the elasticity value of 5.0×10^{10} N/m^2 is a more accurate value for the wet oxide. Both the wavelength tuning characteristic presented in section 4.3.2 and the response characteristic suggest the lower value.

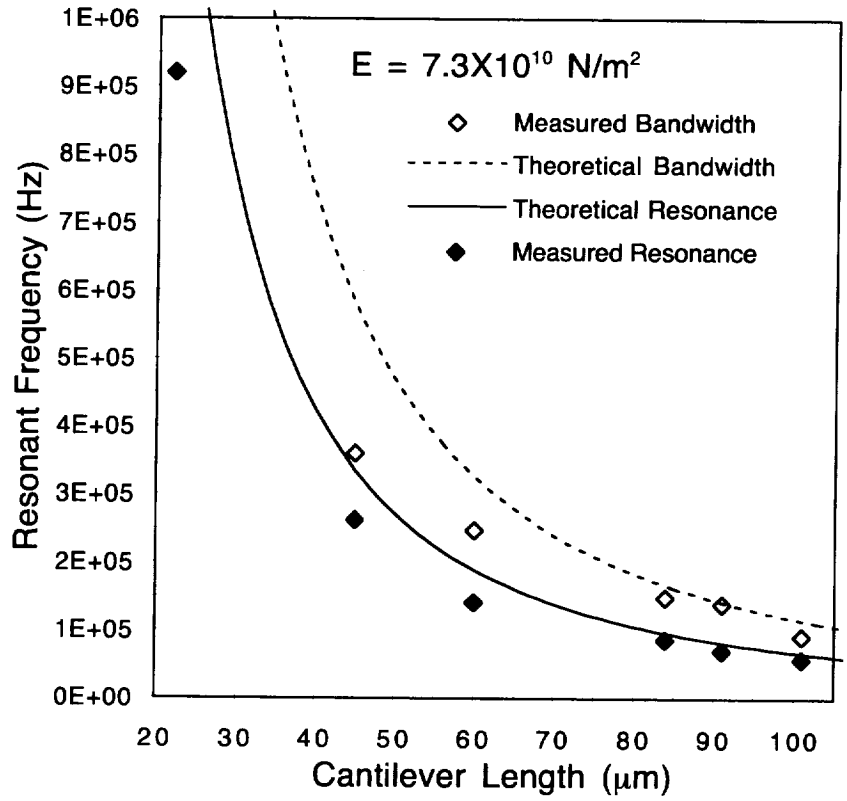

Figure 4-29. Bandwidth and resonant frequency versus cantilever length. The calculated values are shown by the lines and the experimental values by the diamonds. The elasticity modulus used in the theoretical curves was 7.3 X 10^{10} N/m^2.

4.5 References

1. Gere, J. M. and S. P. Timoshenko, *Deflections of Beams,* in *Mechanics of Materials,* R. Kingman, Editor., Wadsworth Inc., Belmont, CA, pp. 405–407, 1984.

2. Yariv, A., *The Propagation of Rays and Beams,* in *Optical Electronics,* M.E.V. Valkenburg, Editor., Saunders College Publishing, a division of Holt, Rinehart and Winston Inc., Philadelphia, PA, pp. 35–71, 1991

3. Petersen, K. E., Dynamic Micromechanics on Silicon: Techniques and Devices, *IEEE Trans. Electron Dev.*,. **ED-25**, p. 1241, 1978.

V. Conclusion

5.1 Summary of the Study: Major Issues

In this work, we have demonstrated a novel single mask level self-aligned process for fabricating micro-mechanical Fabry-Perot filters in (111) Si. We have used this process to fabricate arrays of Fabry-Perot optical filters with a movable cantilever top mirror and a silicon based bottom mirror. Our fabrication process requires only one grown or deposited layer to form the movable mirror, while the substrate material provides for both the sacrificial layer and the bottom mirror. The structure utilizes metallic coatings to provide for the high reflectivity mirrors. The silicon based Fabry-Perot filter can be integrated with low cost silicon-based photodetectors and electronic circuits.

In chapter two we presented a theoretical analysis describing the movement of the cantilever as a function of applied bias and the corresponding optical spectra. The wavelength-voltage tuning characteristic was shown to be parabolic for low voltages. It was shown that small air gap, long length cantilever Fabry-Perots provide the highest wavelength tuning range and highest sensitivity to voltage. Hysteresis in the tuning characteristic was also predicted when the applied voltage was driven past the threshold voltage, V_{th}. Hysteresis is not present for voltages below V_{th}. The theory also predicted tradeoffs: modulator bandwidth for wavelength tuning sensitivity and transmittance for finesse. Numerical calculations showed that 175 nm of wavelength tuning range is provided with a CMOS compatible 4.75 V of applied bias, using a 1 μm air gap, 100 μm long Fabry-Perot with both mirrors gold coated. The finesse of the structure with 40 nm of gold thickness was calculated to be 30 with 181 nm of free spectral range.

The details and results of our modulator fabrication process were presented in chapter 3. The process uses only one grown or deposited layer (silicon dioxide or silicon nitride) to provide the cantilever material. A single mask was used to define the cantilever structure and the electrical isolation. The sacrificial layer and lower mirror material are provided by a (111) silicon substrate. The formation of the air gap under the cantilever relies on a combination of reactive ion etching and KOH anisotropic etching on the (111) silicon substrate. Electrical isolation between mirrors was provided by KOH undercut eaves around the perimeter of the cantilever well and around a hexagonal isolation trench. Gold was the choice of metal for the mirrors due to its high reflectivity and inertness to oxidation. Gold metallization of the cantilever was carried out using thermal evaporation. Metallization of the silicon based bottom mirror was carried out using selective nickel electroplating. The Ni electroplating was successful for structures with air gaps larger than 1 μm. Nickel electroplating can be followed by substitutional gold electroplating to provide higher finesse structures.

Several sources of Fabry-Perot performance degradation were observed during the fabrication. The smoothness and planarity of the silicon based bottom mirror was shown to be highly sensitive to the alignment of the wafer surface normal with the (111) direction (the staircase effect). Bottom mirror surface height deviations ranging from 388 Å to 1700 Å were observed across the 20 μm width of the cantilevers. The smoothness and planarity was also shown to be affected by surface defects in the wafer (the source of the defects is probably the wafer sawing and polishing). The formation of pits in the silicon during the KOH etching was commonly observed especially in the case of short cavity Fabry-Perots. These degradations can be reduced with tighter wafer tolerances.

Silicon dioxide and silicon nitride were presented as good candidates for the cantilever and KOH masking material. In this study we used thermally grown silicon dioxide. A problem in using thermal oxide is the large thermal stress between the oxide and the silicon due to the high growth temperatures and large difference in thermal coefficients of expansion. The stress results in an upward curvature of the cantilever. This curvature results in loss of parallelism between the top and bottom mirrors and consequently a lower finesse structure. Replacement of the thermal oxide layer with a silicon nitride layer in future devices should remedy this problem entirely since silicon nitride's thermal expansion coefficient closely matches that of silicon.

Another problem is the rough electroplating of the silicon in the case of short cavity (on the order of 1

μm) Fabry-Perots. Small air gap Fabry-Perots are attractive since they provide high wavelength sensitivity to voltage. The rough plating is believed to be due to slow plating solution and byproduct transport in the tight and restrictive space under the cantilever. The roughness could be potentially improved by more rigorous solution agitation (higher rpm stirbar, ultrasonic agitation, etc.) and by improving the surface wetting property of the plating solution .

The measured electro-mechanical and electro-optical behavior of the cantilever modulators was presented in chapter 4. The motion and electrical isolation of a cantilever modulator under bias was studied in an SEM. Qualitative results from the SEM study showed agreement with the theory. Electrical isolation between the mirrors was confirmed using voltage contrast SEM. The predicted hysteretic behavior in the motion of the cantilever was also observed. However, the hysteresis was experimentally shown to be avoidable if the voltage is maintained below the threshold voltage.

The spectral tuning characteristics of the cantilevers Fabry-Perots were measured in the 700 to 900 nm wavelength range for a 101 μm long cantilever. Agreement between the theoretically predicted and measured spectra required the modification of the optical theory to account for the stress induced curvature of the cantilever beam and the angular misalignment of the bottom mirror. The wavelength tuning characteristics indicated a blue shift of the wavelength with increasing voltage. The wavelength tuning characteristic was shown to be quadratically dependent on voltage. The theoretically calculated and measured tuning characteristic were in agreement provided that a wet oxide elasticity modulus of 5.0×10^{10} N/m^2 is used. This is in agreement with Petersen's measurements which indicated a lower elasticity modulus for wet oxides ($E = 5.7 \times 10^{10}$ N/m^2 +/- 20%) in comparison to that of dry oxides ($E = 6.9 \times 10^{10}$ N/m^2 +/- 20%) or fused silica ($E = 7.3 \times 10^{10}$ N/m^2).

The frequency response was measured for structures with cantilevers lengths ranging from 22 μm to 101 μm. The theoretically calculated and measured frequency response were in agreement provided that again a wet oxide elasticity modulus of 5.0×10^{10} N/m^2 is used. The modulation bandwidths of the structures ranged from 91 KHz for the 101 μm long cantilever and greater than 920 KHz for the stiffest 22 μm long cantilever. The bandwidth and resonant frequency of the structures exhibited the $1/L^2$ dependence in agreement with the theory. A tradeoff between modulation bandwidth and on/off ratio was observed experimentally and is consistent with theoretical calculations.

5.2 Micro-Mechanical Fabry-Perot Performance Comparison

Table 5-1 provides a comparison between the performance of our 101 μm long cantilever Fabry-Perot and Cornell's DBR Fabry-Perot which is also formed on a silicon substrate[1]. The table also includes theoretically predicted performance characteristics for our structure that are based on expected improvements in mirror quality on future devices.

Column 1 in Table 5-1 lists the tuning sensitivities of the devices. Tuning sensitivity is defined as the required voltage to obtain a transmission wavelength shift. Our measured device exhibits a tuning sensitivity of almost twice that of Cornell's reported structure: 120 nm: 53 V versus their 60 nm: 65 V. Our larger tuning sensitivity occurs even though their device has a much smaller air gap than our structure, 3.0 μm versus our 6.27 μm. For a given voltage the electrostatic force present in their structure is 4 times that of ours (the electrostatic force per unit area is proportional to 1/Air Gap^2). The low sensitivity of their device is probably due to the many stiff DBR layers in the movable mirror structure and the movement of their top mirror through more difficult stretching instead of bending like our cantilever structure. In comparing the spectral filtering quality of the micro-mechanical Fabry-Perots finesse is used as the figure of merit. Cornell's DBR structure exhibits a superior finesse of 35 in comparison to our structures 2.4. In light of the great importance of finesse as a figure of merit for the Fabry-Perot, Cornell's structure is currently better performance wise.

Table 5-1. Micro-Mechanical Fabry-Perot Performance Comparison

	Tuning Sensitivity	Finesse	FSR	Air Gap	Band-width	Number of Layers Required
CUB Measured Au-Ni	120nm: 53V	2.4	60nm	6.27μm	91 KHz	3
CUB Theory Au-Ni	120nm: 53V	13	60nm	6.27μm	94KHz	4
CUB Theory Au-Au	175nm: 5V	30	181nm	1μm	94KHz	4
Cornell's DBR-DBR	60nm: 65V	35	375nm (Calculated)	3μm	?	19

However our device deserves consideration for future research and development. A major advantage of our structure is its simple fabrication process. The fabrication process for our structure requires only 4 total deposited layers including the metallization whereas Cornell's structure requires 19 layers. Consequently our structure is easier to fabricate and may be more integratable with other devices. Furthermore, the theoretical predictions suggest that the finesse of our structure can be competitive with Cornell's provided that the mirror flatness and parallelism of our Fabry-Perot are improved. As previously mentioned, the low finesse of our structure is attributable to the curvature of the cantilever top mirror and the misalignment of the bottom mirror. The replacement of the thermal oxide with either a low temperature oxide or silicon nitride should result in lower stress and a much straighter cantilever. Tighter tolerances on the wafer alignment will reduce the misalignment of the bottom mirror. With these improvements in place, the theory predicts a more competitive finesse of 13 for our structure with a gold top mirror and nickel bottom mirror. The finesse of 13 of course is for an ideal structure and represents an upper bound for the achievable finesse. However we can go one step further and substitutionally replace the nickel on the lower mirror with the higher reflectivity gold. This improvement increases the finesse of our structure to 30 which is comparable and competitive to Cornell's 35. Furthermore, by reducing the air gap of our structure to 1 μm a CMOS compatible 5 V can provide 175 nm of tuning range.

5.3 References

1. Tran, A. T. T. D., et al., Surface Micromachined Fabry-Perot Tunable Filter, *Photonics Tech. Ltrs.*, 8(3), pp. 393–395, 1996.

Comprehensive List of References

Archer, R. R., et al., *An Introduction to the Mechanics of Solids*, 2nd ed. T.J. Lardner, ed., McGraw-Hill, New York, pp. 511–555, 1982.

Bassous, E., H. H. Taub, and L. Kuhn, Ink jet printing nozzle arrays etched in silicon, *App. Phys. Ltrs.*, **31**, p. 135, 1977.

Born, M. and E. Wolf, *Wave Propagation In A Stratified Medium. Theory of Dielectric Films*, in *Principles of Optics*, Pergamon Press, New York, pp. 51–70, 1980.

Brackett, C. A., *Dense wavelength division multiplexing networks: Principles and applications*, IEEE Journal of Selected Areas in Communications, **8**(6), pp. 948–964, 1990.

Burstyn, H. P., Critical point drying: Application of the physics of the PVT surface to electron microscopy, *Am. J. of Phys.*, **43**(5), pp. 414–419, 1975.

Chang-Hasnain, C. J., E. C. Vail, and M. S. Wu, *Widely -tunable micro-mechanical vertical cavity lasers and detectors* in IEEE/LEOS 1996 Summer Topical Meetings: Optical MEMS and Their Applications, Keystone, CO, pp. 43–44, 1996.

Choa, F. S., et al., InGaAs/InGaAsP integrated tunable detector grown by chemical beam epitaxy, *App. Phys. Ltrs.*, **63**(13), pp. 1836–1838, 1993.

Choi, W. S.. and J. G. Smits, A method to etch undoped silicon cantilever beams, *J.of Microelectromech. Sys.*, **2**(2), pp. 82–86, 1993.

Finite Element Structural Modeling Software, Version 67, *MSC/NASTRAN*, MacNeil Schwendler Corporation, Los Angeles, CA, 1993.

Fowles, G. R., *Reflection and Refraction at the Boundary of an Absorbing Medium*, in *Introduction to Modern Optics*, Holt, Rinehart, and Winston Inc., New York, pp. 165–168, 1968.

Fowles, G. R., *Theory of Multilayer Films*, in *Introduction to Modern Optics*, Holt, Rinehart, and Winston Inc., New York, pp. 95–100, 1968.

Fricke, J. and E. Obermeier, *Surface Micromachined Accelerometer Based On A Torsional Moving Structure* in The 8th International Conference on Solid-State Sensors and Actuators, Stockholm, Sweden, pp. 542–545, 1995.

Gere, J. M. and S. P. Timoshenko, *Deflections of Beams*, in *Mechanics of Materials*, R. Kingman, Editor, Wadsworth Inc., Belmont, CA, pp. 405–407, 1984.

Goldman, K. and M. Mehregany, *A Novel Micromechanical Temperature Memory Sensor*, in The 8th International Conference on Solid-State Sensors and Actuators, Stockholm, Sweden, pp. 132–135, 1995.

Harris Jr., J. S., M. C. Larson, and A. R. Massengale, *Coupled -cavity laser diode with micromachined external mirrors*, in IEEE/LEOS 1996 Summer Topical Meetings: Optical MEMS and Their Applications, Keystone, CO, pp. 31–32, 1996.

Ho, S. -T., et al., High index contrast mirrors for optical microcavities. *App. Phys. Ltrs.*, **57**(14), pp. 1387–1389, 1990.

Hornbeck, L. J., *Digital Light Processing and MEMS: An Overview* in IEEE/LEOS 1996 Summer Topical Meetings: Optical MEMS And Their Applications, Keystone, CO, pp. 7–8, 1996.

Jenkins, F. A. and H. E. White, *Dispersion*, in *Fundamentals of Optics*, McGraw-Hill, New York, pp. 464–487, 1957.

Jolly, R. D. and R. S. Muller, Miniature Cantilever Beams Fabricated by Anisotropic Etching of Silicon, *J. of the Electrochem. Soc.*, Solid State Science and Technology, **127**(12), pp. 2750–2754, 1980.

Larson, M. C. and J. S.Harris Jr. *Broadly-tunable, narrow linewidth resonant cavity light emitter* in 53rd Annual Device Research Conference, Charlottesville, VA, pp. 130–131, 1995.

Lo, Y.H., et al., *Integrated micro-optical interferometer arrays*, in IEEE/LEOS 1996 Summer Topical Meetings: Optical MEMS and Their Applications.. Keystone, CO, pp. 25–26, 1996.

Martinet, E., et al., Electrical tunability of infrared detectors using compositionally assymetric GaAs/AlGaAs multiquantum wells, *App. Phys. Ltrs.*,. **60**(7), pp. 895–897, 1992.

Mastrangelo, C. H. and C. H. Hsu, Mechanical Stability and Adhesion of Microstructures: Part I: Basic Theory, *J. of Micro-mech. Sys.*, **2**(1), pp. 33–43, 1993.

Middelhoek, S., J. B. Angell, and D. J. W. Noorlag, Microprocessors get integrated sensors, *IEEE Spect.*, **17**(2), p. 42, 1980.

Nathanson, H. C. and R. A. Wickstrom, A Resonant-Gate Silicon Surface Transistor With High-Q Bandpass Properties, *App. Phys. Ltrs.*, **7**, p. 84, 1965.

Nathanson, H. C., et al., The Resonant Gate Transistor, *IEEE Trans. Elect. Dev.*,. **ED-14**, p. 117, 1967.

Neikirk, Y. K. A. D. P., *Monolithically integrated optically interrogated pressure microsensor*. Acoustic Society of America, p. 2353, 1992.

Petersen, K. E., Dynamic Micromechanics on Silicon: Techniques and Devices, *IEEE Trans. Elect. Dev.*, **ED-25**, p. 1241, 1978.

Petersen, K. E., Micromechanical light modulator array fabricated on silicon, *App. Phys. Ltrs.*, **31**(8), pp. 521–523, 1977.

Petersen, K. E., *Silicon as a mechanical material*, Proceedings of the IEEE, **70**(5), pp. 420–457, 1982.

Queau, E., et al., Electroless Metal Deposition as a Useful Tool For Microelectronics and Microstructures, *J. of the Electrochem. Soc.*, (1), p. 65–69, 1994.

Schwartz, B., Chemical Etching of Silicon, *J. Electrochem. Soc.*,. (12), pp. 1903–1909, 1976.

Seidal, H., et al., Anisotropic Etching of Crystalline Silicon in Alkaline Solutions, *J. Electrochem. Soc.*, **137**(11), pp. 3626–3632, 1990.

Seidal, H., *Crystalline Semiconductor Micromachining*, in Transducers '87 Rec. of the 4th Int. Conf. on Solid-State Sensors and Actuators, pp. 120–125,1987.

Stokey, W. F., *Vibrations of Systems Having Distributed Mass and Elasticity*, in Shock and Vibration Handbook, C. M. Harris, Editor., McGraw-Hill, New York. pp. 7-1 to 7-15, 1988

Sze, S. M., *Oxidation and Film Deposition*, in Semiconductor Devices: Physics and Technology, Murray Hill, NJ, pp. 360–362, 1985.

Sze, S. M., *Physics of Semiconductor Devices*, John Wiley & Sons, New York, 1969.

Tran, A. T. T. D., et al., *Electro-mechanically tunable micro Fabry-Perot filter array*, in 53rd Annual Device Research Conference, Charlottesville, VA, pp. 128–129, 1995.

Tran, A. T. T. D., et al., Surface Micromachined Fabry-Perot Tunable Filter, *Photonics Tech. Ltrs.*, **8**(3), pp. 393–395, 1996.

Transene Inc., *Advanced Materials For Electronics*, Rowley, Mass. p. 126–127, 1981.

Transene Inc., *Advanced Materials For Electronics*, Rowley. Mass. p. 138–139, 1981.

Uenishi, Y., *Coupled -cavity laser diode with micromachined external mirrors*, in IEEE/LEOS 1996 Summer Topical Meetings: Optical MEMS and Their Applications, Keystone, CO, pp. 33–34, 1996.

Waggener, H. A., R .C. Kragness, and A. L. Taylor, KOH Etching of Si, *Elect.*,. **40**, p. 274, 1967.

Waynant, R. and M. Ediger, *Electro-Optics Handbook*, 1st ed., McGraw-Hill, New York, pp. 11.56–11.75, 1994.

Wilmsen, C. W., E. G. Thompson, and G. H. Meissner, Buckling of Thermally-Grown SiO2 Films. *IEEE Trans. Elect. Dev.*, (1), p. 122, 1972.

Wipiejewski, T., et al., Tunable extremely low threshold vertical cavity laser diodes, *IEEE Photonics Ltrs.*, **5**(8), pp. 889–892, 1993.

Wolber, W. G. and K. D. Wise, Sensor development in the microcomputer age, *IEEE Trans. Elect. Dev.*, **ED-26**, p. 1864, 1979.

Wu, M. S., et al., Widely and continuously tunable micromachined resonant cavity detector with wavelength tracking, *IEEE Photonics Tech. Ltrs.*, **8**(1), p. 98–100, 1996.

Wu, M.S., et al., *Widely tunable micromachined gallium arsenide fabry-perot filters* in IEEE/LEOS, Keystone, CO, (Post Deadline Paper), 1994.

Yariv, A., *The Propagation of Rays and Beams*, in *Optical Electronics*, M. E. V. Valkenburg, Editor., Saunders College Publishing, a division of Holt, Rinehart, and Winston Inc., Philadelphia, PA, pp. 35–71, 1991.

Zeghbroeck, B. J. Van., *Micro-Mechanics* in Principles Electronic Devices, University of Colorado, Boulder, pp. A1.1–A1.4, 1995.

REPORT DOCUMENTATION PAGE

Form Approved
OMB No. 0704-0188

Public reporting burden for this collection of information is estimated to average 1 hour per response, including the time for reviewing instructions, searching existing data sources, gathering and maintaining the data needed, and completing and reviewing the collection of information. Send comments regarding this burden estimate or any other aspect of this collection of information, including suggestions for reducing this burden, to Washington Headquarters Services, Directorate for Information Operations and Reports, 1215 Jefferson Davis Highway, Suite 1204, Arlington, VA 22202-4302, and to the Office of Management and Budget, Paperwork Reduction Project (0704-0188), Washington, DC 20503.

1. AGENCY USE ONLY (Leave blank)

2. REPORT DATE
September 1997

3. REPORT TYPE AND DATES COVERED
Technical Paper

4. TITLE AND SUBTITLE
Micro-Mechanical Voltage Tunable Fabry-Perot Filters Formed in (111) Silicon

5. FUNDING NUMBERS
WU 274-00-97-01

6. AUTHOR(S)
James D. Patterson

7. PERFORMING ORGANIZATION NAME(S) AND ADDRESS(ES)
NASA Langley Research Center
Hampton, VA 23681-2199

8. PERFORMING ORGANIZATION REPORT NUMBER
L-17646

9. SPONSORING/MONITORING AGENCY NAME(S) AND ADDRESS(ES)
National Aeronautics and Space Administration
Washington, DC 20546-0001

10. SPONSORING/MONITORING AGENCY REPORT NUMBER
NASA TP-3702

11. SUPPLEMENTARY NOTES
The information in this report was offered as a thesis in partial fulfillment of the requirements for the Degree of Doctor of Philosophy in Electrical Engineering, University of Colorado, Boulder, Colorado.

12a. DISTRIBUTION/AVAILABILITY STATEMENT
Unclassified-Unlimited
Subject Category 33
Availability: NASA CASI (301) 621-0390

12b. DISTRIBUTION CODE

13. ABSTRACT (Maximum 200 words)
The MEMS (Micro-Electro-Mechanical-Systems) technology is quickly evolving as a viable means to combine micro-mechanical and micro-optical elements on the same chip. One MEMS technology that has recently gained attention by the research community is the micro-mechanical Fabry-Perot optical filter. A MEMS based Fabry-Perot consists of a vertically integrated structure composed of two mirrors separated by an air gap. Wavelength tuning is achieved by applying a bias between the two mirrors resulting in an attractive electrostatic force which pulls the mirrors closer. In this work, we present a new micro-mechanical Fabry-Perot structure which is simple to fabricate and is integratable with low cost silicon photodetectors and transistors. The structure consists of a movable gold coated oxide cantilever for the top mirror and a stationary Au/Ni plated silicon bottom mirror. The fabrication process is single mask level, self aligned, and requires only one grown or deposited layer. Undercutting of the oxide cantilever is carried out by a combination of RIE and anisotropic KOH etching of the (111) silicon substrate. Metallization of the mirrors is provided by thermal evaporation and electroplating. The optical and electrical characteristics of the fabricated devices were studied and show promissing results . A wavelength shift of 120nm with 53V applied bias was demonstrated by one device.

14. SUBJECT TERMS
Micro-Electro-Mechanical Systems (MEMS) , Fabry-Perot Filters, Silicon Micro-Machining

15. NUMBER OF PAGES
107

16. PRICE CODE
A06

17. SECURITY CLASSIFICATION OF REPORT
Unclassified

18. SECURITY CLASSIFICATION OF THIS PAGE
Unclassified

19. SECURITY CLASSIFICATION OF ABSTRACT
Unclassified

20. LIMITATION OF ABSTRACT

NSN 7540-01-280-5500

Standard Form 298 (Rev. 2-89)
Prescribed by ANSI Std. Z-39-18
298-102